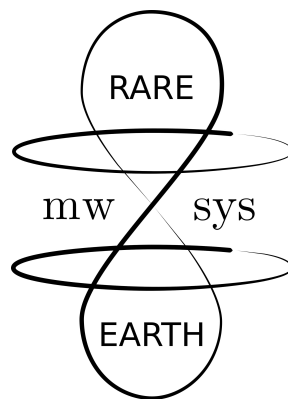




Walther
Meißner
Institut



Energy Exchange Between Spatially Separated Cryogenic Rare-Earth Electronic Spin Ensembles



THESIS

submitted in partial fulfillment of the
requirements for the degree of

MASTER OF SCIENCE
in
PHYSICS

Author :
Matrikel-Nr. :
Supervisor :

O.T. Huisman
03770892
Prof. Dr. Rudolf Gross
Dr. Nadezhda Kukharchyk

Garching-Forschungszentrum, Germany, March 2023

Energy Exchange Between Spatially Separated Cryogenic Rare-Earth Electronic Spin Ensembles

O.T. Huisman

Delft University of Technology
Delft, Netherlands

Walther-Meißner-Institut, Bayerische Akademie der Wissenschaften
Physik-Department, Technische Universität München
Garching, Germany

March 2023

Abstract

Superconducting coplanar waveguide chips were designed and microfabricated using optical lithography. The fabricated chips were used to perform millikelvin measurements on the rare earth ion $^{167}\text{Er}^{3+}$ doped in a Yttrium Orthosilicate crystal. The goal of the measurements is to obtain insight into the possibility of phonon-mediated energy transfer between spatially separated spin ensembles. In addition, numerical simulations were performed to study the thermodynamic behaviour of spin ensembles interacting with a phonon bath.

*Die Schönheit ist das Durchleuchten des ewigen Glanzes des Einen,
durch die materielle Erscheinung.*
Werner Heisenberg

Introduction

1.1 Motivation of Research Effort

1.1.1 Physical production of Quantum Memory

The main goal of quantum memory research is to develop a platform and operating protocol that allows for the storage of quantum information. These protocols will be operated side-by-side with quantum computing architecture, a so-called hybrid architecture. The memory should be able to store the state of the involved qubits over timescales longer than the coherence time of the computing hardware would normally permit. One of the most promising quantum computing platforms is coplanar superconducting circuits containing waveguides and combinations of harmonic and anharmonic resonators.[1] Due to the nature of the latter, these circuits are usually operated at radio or microwave frequencies. To directly couple superconducting qubits to a memory interface, with only on-chip components (e.g. no lasers), requires that the memory interface operates in this frequency regime as well.

Optical storage of quantum information in rare earth (RE) solid state spin ensembles has proven very successful. To be specific, in these optical memory protocols microwave states were stored using the combination of an atomic transition and a nuclear spin transition[2][3][4], using a combination of optical and electron spin resonance (ESR) techniques. The former matches optical frequencies, while the latter allows for long coherence times, sometimes on the order of days.[5][6] The same platform shows promise for the low microwave regime by solely applying ESR techniques on the RE electron spin.[7] Circuit quantum electrodynamics experiments have al-

ready been performed in this context. In these experiments, a RE-doped crystal is placed directly on top of a coplanar microwave resonator. Usually, continuous wave (CW) spectroscopy is performed by sweeping the strength of an external magnetic field, while applying very low power to the resonator. The latter implies that the resonator is in the quantum regime, hosting an energy on the order of single microwave photons. The characteristic hybridisation of the resonator level structure with that of the spin ensemble is observed. Some of these experiments made use of a superconducting resonator, which can be fabricated with the same methods commonly used for superconducting quantum circuits. More recently also pulsed ESR experiments were done with such a setup, showing that solid state RE dopants could provide a microwave quantum memory platform.[8][9]

1.1.2 Questions Concerning Coherence

One of the most promising multimode quantum memory protocols is that of the Atomic Frequency Comb (AFC), first introduced in 2008.[2] The main idea is to burn a frequency comb of narrow spectral holes into an inhomogeneously broadened absorption line.[10][11] A photon whose linewidth spans several of the spectral holes will be collectively absorbed. Analogous to Hahn echo [12], the absorbing spectral holes will coherently refocus and reemit the photon. Why this is in fact a multimode memory is explained below. What makes AFC more attractive than other RE quantum memory protocols is that for the latter their efficiency depends on the optical depth of the medium.[4] Other protocols such as Electromagnetically Induced Transparency (EIT) [13][14] or Controlled Reversible Inhomogeneous Broadening (CRIB)[15] for example, theoretically requires materials with quite large optical depths. Considering this fact, it is natural that there has come to be a research focus on implementing AFC memories in RE platforms and improving their fundamental ingredient: spectral hole burning in inhomogeneous lineprofiles.

Informally, if the frequency comb profile contains a number of peaks N , with peak frequency spacing Δ and peak width γ into a two-level system with a ground and excited state $|\uparrow\rangle$ resp. $|\downarrow\rangle$, the stored phonon state will take the form[16][17]:

$$|\psi(t)\rangle = \frac{1}{\sqrt{N}} \sum_{j=1}^N c_j e^{2\pi i \Delta j t} |\uparrow_1 \dots \downarrow_j \dots \uparrow_N\rangle$$

As long as this state stays coherent, each component of the superposition will be in-phase at integer multiples of $t = 1/\Delta$. At these points in time

the system will remit the photon state a spin echo. To turn this into an on-demand process a transition to a metastable state can be additionally driven. It must be however clear that the efficiency, i.e. the amount of signal that can be retrieved with this protocol is limited by the smallest coherence time T_2 in the system. The decoherence-limited efficiency then goes as:

$$\eta \sim e^{-\frac{1}{\Delta T_2}}$$

This technique can be extended to temporal multimode storage by ensuring that the original phonon is a pulse contained within a temporal width T that is smaller than $1/\Delta$. [18] The number of such photons that theoretically could be stored is then given by:

$$N_p = \frac{1}{\Delta T}$$

Microwave frequency multiplexing is principle not impossible, but this would require the AFC to be applied to several inhomogeneously broadened transitions. As mentioned above the protocol is implemented with resonators applying pulsed ESR techniques. Resonators of course only operate within a small band, and overtones of that band. Recent work has shown that CW ESR spectroscopy can be performed using a broadband coplanar waveguide (CPW) instead of a coplanar resonator. [19][20]. In the future, this might allow for broadband pulsed ESR implementation of AFC memory. This is one of the research focuses of the microwave RE systems group in which the work presented here was done.

As mentioned above, the effectiveness of AFC will depend on the coherence time of the spin ensemble. This is true for most quantum memory protocols. Within the study of quantum hardware platforms, it is well known that this limit can be greatly extended by cooling down the system to temperatures on the order of 10 millikelvin. This requires samples to be placed at the lowest temperature stage of a helium dilution refrigerator. There are several reasons for this. One of them is simply that the energy of the quantum level splitting $\sim \hbar\omega$ must be smaller than the average energy of thermal fluctuations $\sim k_B T$, for the system to be in a coherent quantum state at all. The second reason is that decoherence and relaxation in their most basic description are governed by processes that depend on the interaction of a spin with a thermal bath. Lowering the temperature of this bath means diminishing its occupation, which leads to longer coherence times.

This however relates to an open question that has existed since the golden days of ESR, and relates specifically to the spin relaxation due to lattice vibrations. It has become standard knowledge that spin-lattice interaction is

the mechanism behind the T_1 -relaxation of solid-state spin systems. [21]. In the theoretical formalism on which this knowledge is based, the solid state crystal lattice is treated as one of the environmental thermal baths. It will be explained in section 2.2, that this assumption touches upon some fundamental questions. Driving a millikelvin thermal bath within a small frequency band makes the use of a thermodynamic quantity 'temperature' problematic. Within a certain frequency regime the transfer of energy from the spins to the lattice phonons, will lift a spectral band of lattice out of thermal equilibrium. This is known as phonon bottleneck, because the resonant non-equilibrium phonons that come into being, will reduce the efficiency by which the spins can relax away their energy.[22] The many-body non-equilibrium dynamics that govern this process are very complex. An illustration is given in figure 1.1. If the issue of spectral non-equilibrium is ignored, one can still perform a very reasonable correction to the relaxation description.[23][24]. In essence, one assumes there to be two thermal baths. One indeed being the crystal lattice, the other being the thermostat that cools the millikelvin stage holding the samples. One is able to find an adjusted T_1 by assuming that both the lattice and the spin system must relax to the thermal equilibrium set by the mixing chamber. If the temperature and field dependence characteristic of this reduced T_1 have been observed, it is seen as an indicator of a phonon bottleneck presence. A recent study presented such kind of evidence that indicate a phonon bottleneck in a prominent candidate platform for quantum memory, namely Erbium doped Y_2SiO_5 . [25]

The approach of two thermal baths however does not address the problem of non-equilibrium within the lattice itself, caused by spins relaxing most strongly into phonons in resonance with the level splitting. The complex decoherence behaviour observed in photon echo experiments [26], indicate that still some finer details concerning the bottleneck could be interesting to investigate. While microscopic treatments of the phonon bottleneck have been attempted[27], the connection between microscopic interactions and the thermodynamic behaviour has not fully been described yet. The nonequilibrium of the phonon bath might have a different effect, depending on which part of the ESR spectrum is being observed, and therefore might influence the efficiency of quantum memory protocols in unforeseen ways.

Keeping in line with the general goal of a broadband cavity-free quantum memory platform, CW ESR measurements were performed on a spin ensemble using broadband superconducting coplanar waveguides, fabricated on-chip.

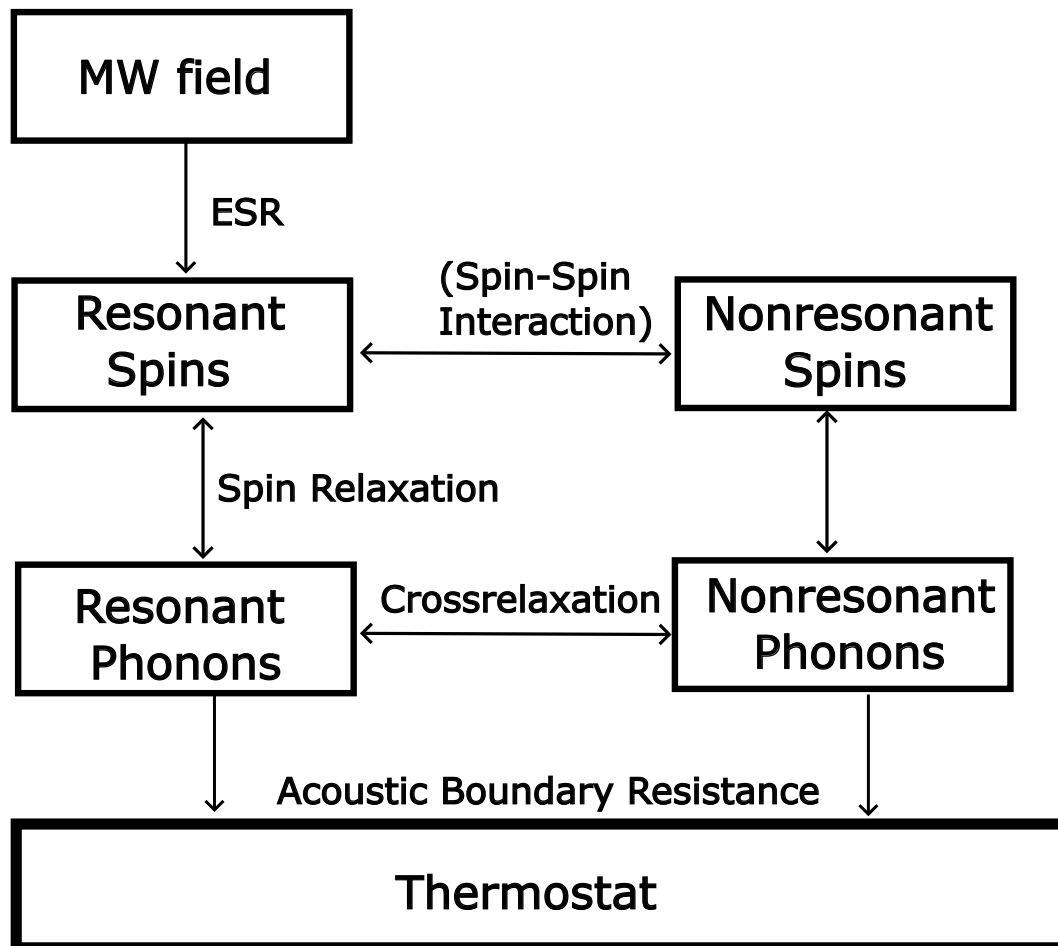


Figure 1.1: Diagram showing the different interactions that come into play in the phonon bottleneck. The external field excites spin, which relax their energy into phonons. The phonons then relax either by frequency downconversion or through contact with the thermostat. In the case of a bottleneck, the resonant phonon bath moves out of thermal equilibrium with the thermostat and starts reexciting spins. Things become more complicated if spin-spin interactions with non-resonant spins are taken into account[28], which in turn couple to non-resonant phonons.

The goal of the measurements was to clarify some aspects of the phonon bottleneck. The spin species in question were those of Erbium-167 in Y_2SiO_5 , for which experimental evidence suggests the existence of a phonon bottleneck. For this purpose, a unique on-chip coplanar set-up was used, namely a chip consisting of two patterned waveguides. The host RE-doped crystal covers both. The goal of this layout is that one waveguide is used to do CW spectroscopy, while the other is used to provide strong driving at a single frequency, which we refer to as pumping. The lines should be far enough apart that the field induced by one is not felt by the other. In that case, any effect from the pump on the measured spectrum must theoretically be transferred by means of non-equilibrium heat transfer. The design of the device and the performed measurements are discussed in chapter 3. In figure 1.2 pictures of the device and sample are displayed.

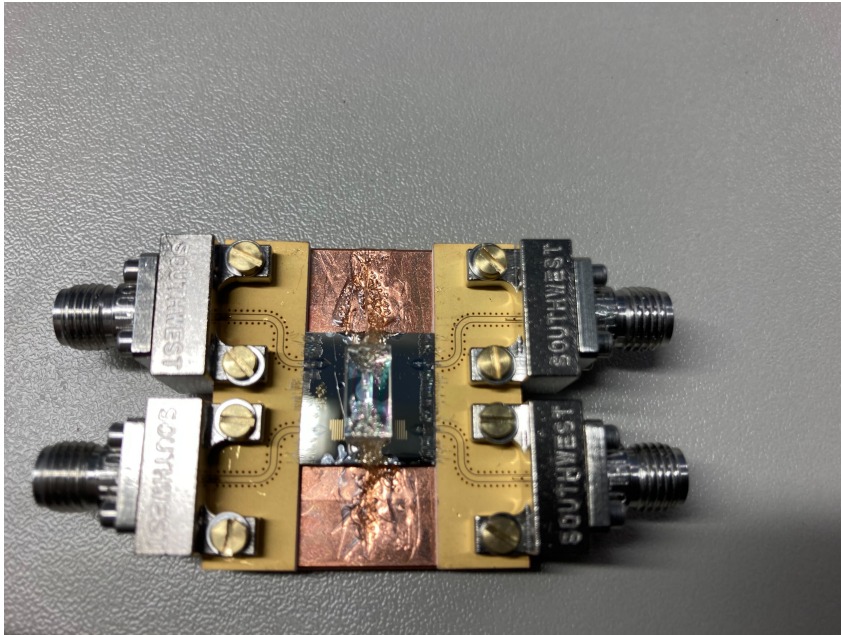
In parallel to the experimental investigation, a simple model was developed based on an older (somewhat obscure) formalism that allows for the application of the quantum mechanical equation of motions in a non-equilibrium thermodynamic context. This is presented in chapter 2. Computational results from this model gave a correct qualitative indication of what was to be expected in the pump-probe measurements. In the combination of modeling and measuring an effort was made towards a new method that could potentially characterize some of the thermodynamic aspects of the phonon bottleneck, based on the phonon-mediated energy transfer between spatially separated spin ensembles.

1.2 Electron spins of Er:YSO

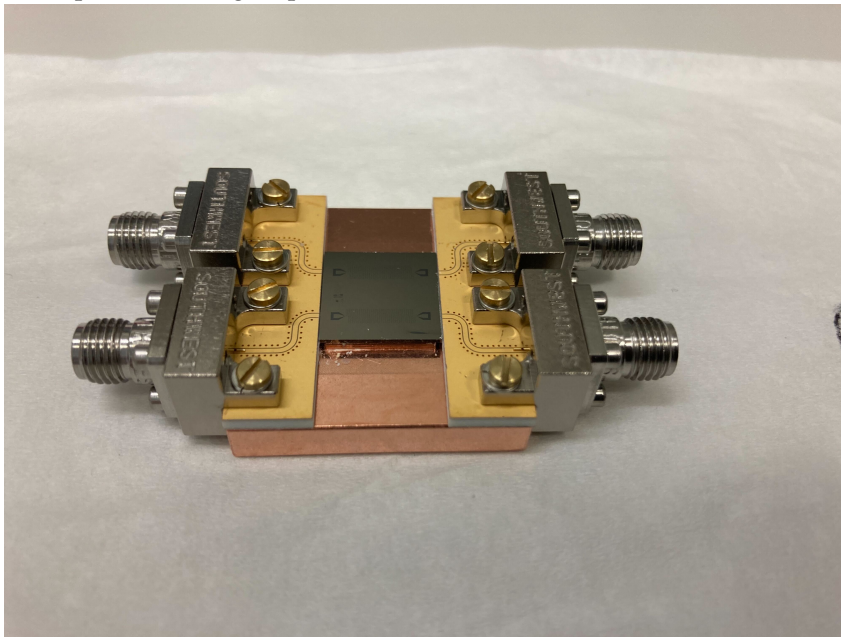
1.2.1 Crystal Structure of YSO

Yttrium Orthosilicate (Y_2SiO_5) is part of the large orthosilicate (X_2SiO_5) class of optical materials and has proven to be a suitable host for RE-based quantum information processing.[29] It combines a large optical depth with good coherence properties in both optical and microwave regimes.[30] The latter has to do with the magnetic environment in YSO, which allows for very narrow homogeneous linewidths, which are inversely proportional to the echo decay time. This is mostly because the abundant Silicon and Oxygen isotopes are nonmagnetic. Only the Yttrium nuclear spins contribute to this magnetic environment, in which the magnetic moment is only $0.137\mu_B$. Significant progress in quantum memory has been made using YSO as host.

YSO has the symmetry of the space group $C2/c$, and the doping sites of



(a) Sampleholder plate with PCBs and the Er:Y₂SiO₅ sample on top of the superconducting chip.



(b) Sampleholder plate with PCBs and superconducting chip before wirebonding. The two waveguides are distinguishable on the chip surface.

Figure 1.2: Colour pictures of the used device and sample.

the point group $C1$. [31] Both undoped and doped YSO can be grown using the Czochralski method and seems specifically well suited to host Erbium. RE ions can be implanted into undoped YSO with a focused ion beam (FIB) system. [32] The Er^{3+} dopants replace Y^{3+} in the lattice at two magnetically inequivalent lattice sites. Erbium and Yttrium ions have the same charge and similar ionic radii, which allows for doping without causing significant strain or a large number of lattice defects. Both Erbium-doped as-grown crystals and Erbium implanted crystals show good prospects for quantum computing.

1.2.2 Rare Earth Ions

When rare earth is mentioned as a platform for quantum information science, one usually is referring to doped dielectric crystals, with the dopants being ions from the upper row of the f -block in the periodic system. Starting at $Z = 57$, the orbital structure is filled from $[\text{Xe}]5d^16s^2$ up. By virtue of the *Aufbau* principle, the next orbital that is occupied from $Z > 56$ onward is $4f$. This results in all of the REs having either a $[\text{Xe}]4f^n6s^2$ or $[\text{Xe}]4f^n5d^16s^2$ configuration. [23] Due to the preference for empty, half-filled, or filled orbitals, the above structure leads to nearly all species having valence 3. This gives them almost identical chemical properties, which justifies naming the collective of RE elements after their first member [33]: ‘lanthanide series’ or simply ‘lanthanides’. The $4f$ orbitals have a smaller radius than the $6s$ and $5p$ orbitals, which somewhat shield the $4f$ electrons from the crystalline environment. [34] This can be observed in their improved coherence and in the fact that orbital angular momentum behaves more like that of a free atom. Compare this to the quenching of orbital angular momentum that occurs for d electrons, due to the orbital moments precessing in the static crystal field, and consequently their expectation values averaging out to zero. For rare earths L is barely quenched, implying that the spin-orbit coupling dominates over the crystal field potential in the Hamiltonian. [35] We will spend most attention on Erbium, which played a role in experiments.

Spectral Structure of ^{167}Er

The fact that the electronic orbital angular momentum is only weakly affected by the crystal field has significant effects on the spectroscopic properties of RE atoms.

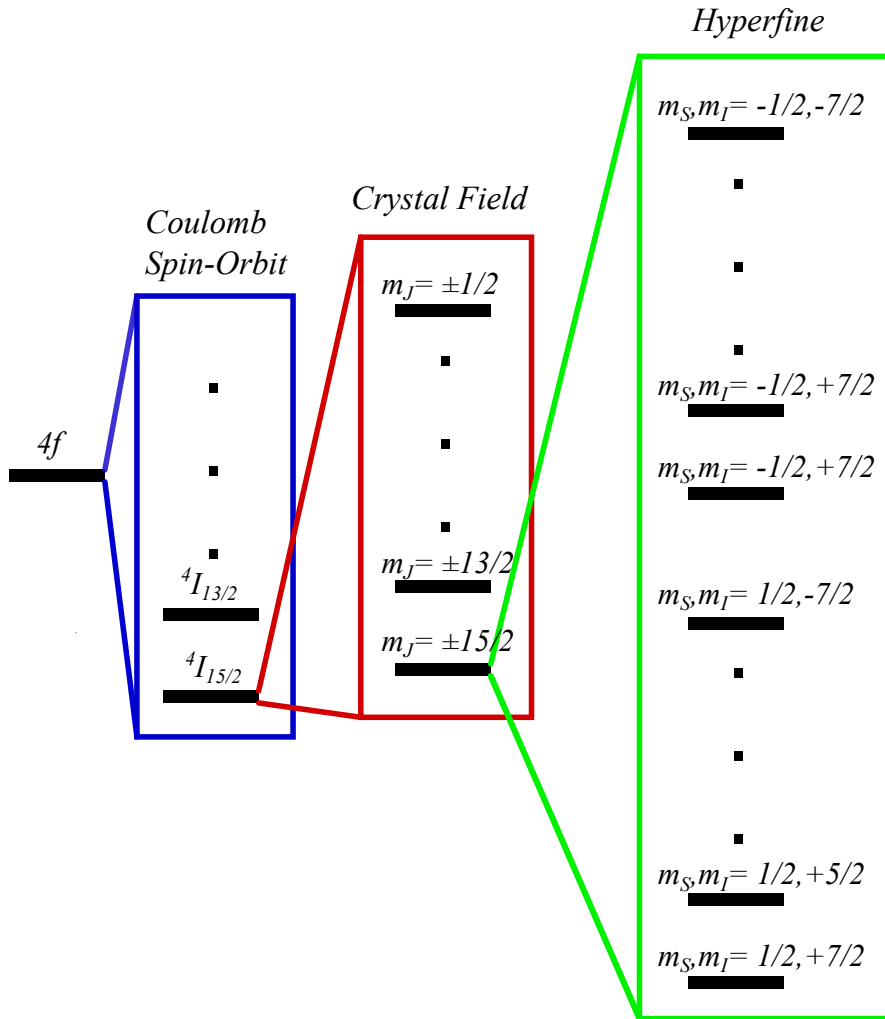


Figure 1.3: Diagram illustrating the splitting of the 4f spectrum in 167-Er:YSO.

The fact that 4f electrons retain their orbital angular momentum causes strong spin-orbit coupling, and consequent hybridisation into total angular momentum states:

$$J = L \oplus S = L + S, L + S - 1, \dots, |L - S|$$

In a host crystal, the local electrostatic field will further split the J states into different m_J states (Stark splitting). Additionally, the atomic level structure of the species with an odd number of electrons has Kramers degeneracy. The crystal field will not split the Kramer's doublets, since electrostatic fields do not break time-reversal symmetry, i.e. does not distinguish between up or down spin. The Kramers degeneracy is broken either by the Zeeman

effect or hyperfine coupling.[36] For 167-erbium it is the latter. All of these splittings are summarised in figure 1.3.

The general Hamiltonian of an electron bound to a dopant is given by [35]:

$$H = \frac{1}{2m} \left(\mathbf{p} - \frac{q}{c} \mathbf{A} \right)^2 + \lambda \mathbf{L} \cdot \mathbf{S} + 2\mu_B \mathbf{B} \cdot \mathbf{S} + V_{ec} + V_{nc} + V_{cf}$$

The first term is simply the long momentum of the electronic motion. Here $\lambda \mathbf{L} \cdot \mathbf{S}$ is the Russel-Saunders spin-orbit coupling, $2\mu_B \mathbf{B} \cdot \mathbf{S}$ is the electronic Zeeman interaction, V_{nc} is the nuclear Coulomb potential, V_{ec} the Coulomb potential generated by the other bound electrons, while V_{cf} is the crystal field potential. In the gauge $\mathbf{A} = \frac{1}{2} \mathbf{B} \times \mathbf{r}$, the long momentum can be rewritten to give:

$$H = \frac{p^2}{2m} + \lambda \mathbf{L} \cdot \mathbf{S} + \mu_B \mathbf{B} \cdot \mathbf{L} + 2\mu_B \mathbf{B} \cdot \mathbf{S} + V_{ec} + V_{nc} + V_{cf} + \text{weak diamagnetism} \quad (1.1)$$

The strongest interaction term is the electronic Coulomb potential V_{ec} , which splits the spectrum into separate L states. As mentioned above, the spin-orbit coupling dominates over the Zeeman and crystal field terms, it quantises the spectrum further into eigenstates of the total angular momentum $\mathbf{J} = \mathbf{L} + \mathbf{S}$. In general, the state J is λJ above the $J - 1$ state in energy. The combined effect of the Coulomb and spin-orbit interaction is that all of J, L, S must be considered when describing the eigenstates of RE atoms.

However, for ESR spectroscopy, an effective Hamiltonian in \mathbf{S} is more desired. Therefore we take a step back and treat the \mathbf{L} dependent terms of the Hamiltonian as a perturbation to spin states. Take the following generic state, given L, m_L and some spin state $|s\rangle$ which is not specified any further.

$$|\psi_s(\mathbf{r})\rangle = f(r) |L, m_L\rangle |s\rangle$$

Perturbation theory then predicts the correction to $|\psi(\mathbf{r})\rangle$ from the orbital Zeeman term to be:

$$|\psi_s(\mathbf{r})\rangle = f(r) \left(|L, m_L\rangle + \sum_i \sum_{\tilde{m}_L \neq m_L} \frac{\langle L, \tilde{m}_L | L_i | L, m_L \rangle}{E_{m_L} - E_{\tilde{m}_L}} \mu_B B_i |L, \tilde{m}_L\rangle \right) |s\rangle$$

The matrix elements of the spin-orbit interaction w.r.t. these perturbed states

are:

$$= 2\lambda\mu_B|f(r)|^2 \sum_{ij} \sum_{\tilde{m}_L \neq m_L} \frac{\langle \psi_{s'}(\mathbf{r}) | \lambda \mathbf{L} \cdot \mathbf{S} | \psi_s(\mathbf{r}) \rangle \langle L, \tilde{m}_L | L_i | L, m_L \rangle \langle L, m_L | L_j | L, \tilde{m}_L \rangle \langle s' | S_i | s \rangle B_j}{E_{m_L} - E_{\tilde{m}_L}}$$

The effective coupling between the external field and the electron spin can now be written in the bilinear form:

$$H_Z = \mu_B \mathbf{B} \cdot \mathbf{g} \cdot \mathbf{S}$$

where \mathbf{g} is the gyromagnetic tensor, that has the components:

$$g_{ij} = 2\delta_{ij} + 2\lambda|f(r)|^2 \sum_{\tilde{m}_L \neq m_L} \frac{\langle L, \tilde{m}_L | L_i | L, m_L \rangle \langle L, m_L | L_j | L, \tilde{m}_L \rangle}{E_{m_L} - E_{\tilde{m}_L}}$$

for a transition between spin states attached to an orbital state $f(r) |L, m_L\rangle$, which have broken degeneracy, as was explained above.

The crystal field potential can naturally be applied to these eigenstates due to a construction by Stevens.[37] The potential V_{cf} is decomposed into spherical harmonics.

$$V_{cf} = \sum_{\ell m} C_{\ell m} r^\ell Y_{\ell m}$$

The coefficients $C_{\ell m}$ depend on the possible electronic configuration of the ion and on the nature of the crystalline environment. Specifically, the point symmetry of the ion is encoded in these coefficients. Within a highly symmetric crystal field, most of them are zero. The spherical harmonics then act on the L states by rewriting the spherical harmonics in Cartesian coordinates, and replacing (x, y, z) by (L_x, L_y, L_z) , for example:

$$r^1 Y_1^1 \sim x + iy \longrightarrow L_x + iL_y$$

From this, it can be seen that the general effect of V_{cf} , when coupling between states with the same J , is to break the degeneracy in m_J . The given example crystal field potential can be effectively written as $J_x + iJ_y$.

Let us now consider Erbium in detail, which is in the configuration $[\text{Xe}]4f^{12}6s^2$. Ionic Erbium has charge +3, the two outer $6s$ and a single $4f$ have been removed. The ion has 65 electrons, so it has Kramers degeneracy. The ground state w.r.t. the nuclear and electronic Coulomb potential is $^{2s+1}L_J = ^4 I_{15/2}$, which will be split into 8 spin degenerate levels by the crystal field. The

crystal field splitting is on the order of THz, which causes sharp optical transitions.[29] The Zeeman splitting is on the order of GHz, and at cryogenic temperatures only the lowest Kramer doublet is occupied. [29]

As was mentioned above, the Erbium will dope the host at two inequivalent crystal sites. This means that we consider our paramagnetic system, not as one but two effective $S = \frac{1}{2}$ systems, with different transition frequencies. Both sites have the point symmetry of the group C_1 . This is the trivial group, meaning that there is no real symmetry to speak of.

In contrast to the other isotopes, the ^{167}Er isotope has a net nuclear spin of $I = \frac{7}{2}$. The hyperfine interaction between the electron and nuclear spin would be added to the total Hamiltonian of eq. 1.1 in the form of a magnetic dipole interaction.[38] This form is bilinear in \mathbf{S} and \mathbf{I} , and can be written in simple form using tensor \mathbf{A} :

$$H_{hf} = \mathbf{S} \cdot \mathbf{A} \cdot \mathbf{I}$$

The hyperfine coupling between the nucleus and electrons will split each Kramer doublet into 16 hyperfine levels.

Effective Spin Hamiltonian

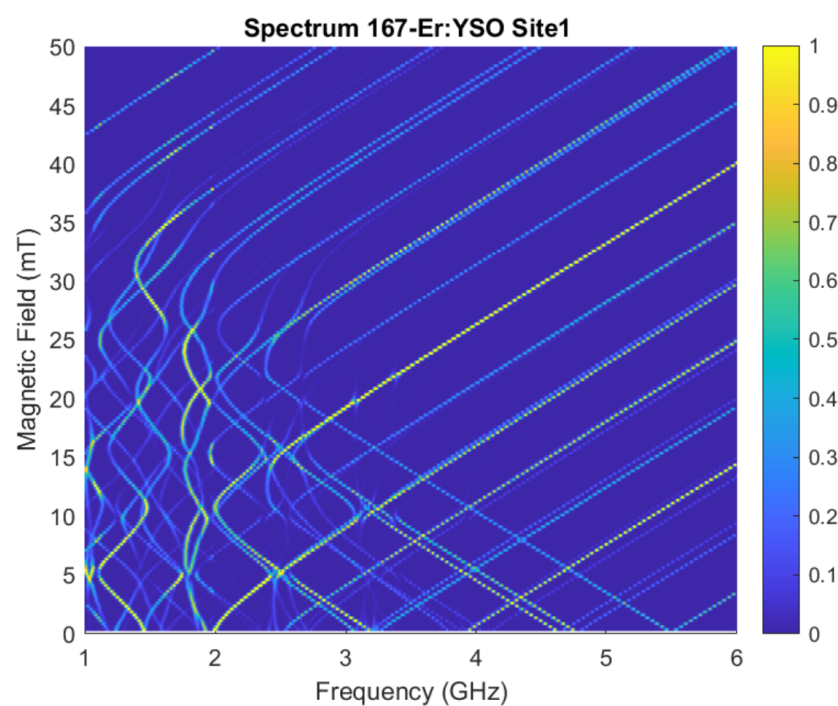
Before we construct the ESR Hamiltonian there is one more relevant interaction that needs to be discussed, namely the quadruple coupling between the Er^{167} nuclear spin and the crystal field.[39] Any nucleus with spin $I > \frac{1}{2}$ will have an ellipsoid charge distribution, which does not have spherical symmetry. The measure of how prolate or oblate the shape of the charge distribution is, which is referred to as the nuclear quadruple moment, which couples to external electrostatic fields. This means that there will be an energetically favourable orientation of the nucleus within the crystal field, which is not necessarily aligned with any of the crystal symmetry axes.

Taking all of the above into account, the general spin $S = \frac{1}{2}$ Hamiltonian is written as:

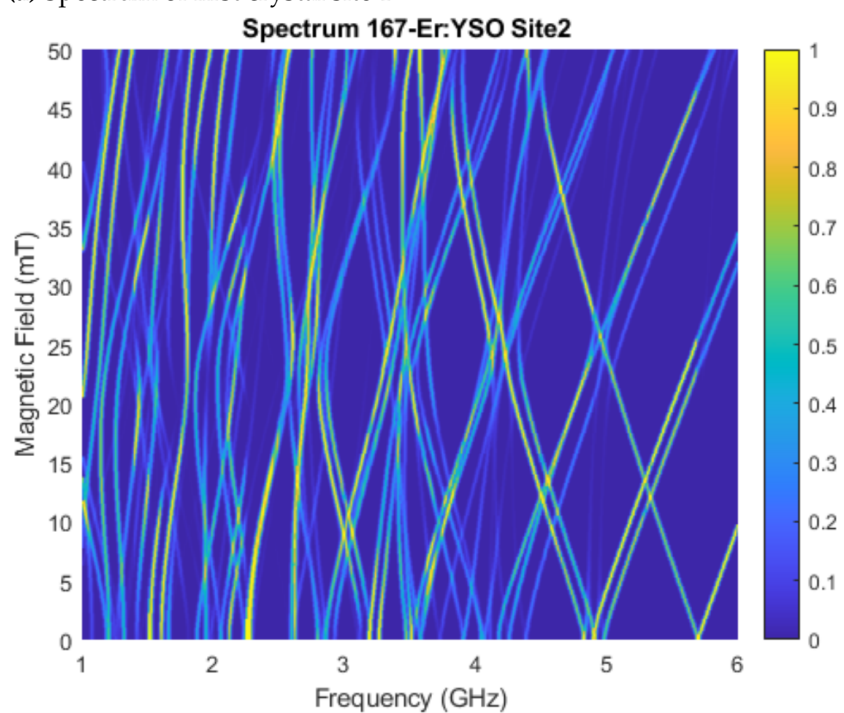
$$H = \mu_B^e \mathbf{B} \cdot \mathbf{g} \cdot \mathbf{S} + \mathbf{I} \cdot \mathbf{A} \cdot \mathbf{S} + \mathbf{I} \cdot \mathbf{Q} \cdot \mathbf{I} - \mu_B^n g_n \mathbf{B} \cdot \mathbf{I} \quad (1.2)$$

Here \mathbf{g} , \mathbf{A} , \mathbf{Q} are resp.the gyromagnetic, hyperfine, and quadruple tensor. These quantities have to be represented as rank(2) tensors since the coordinate frames of the magnet, electron spin, nuclear spin, and crystal will in general not be aligned. \mathbf{B} is the external magnetic field. μ_B^e, μ_B^n , are the electron resp. nuclear Bohr magneton, and g_n is the nuclear g-factor.

Precise ESR spectroscopy of Er:YSO was performed by Guillet-Noël et al. (2006).[40] Based on their results, the field-dependent ESR spectra have been simulated using Easyspin.[41] The orientation of the crystal was chosen to correspond with that of the experiments. More details on this are given in chapter 3.



(a) Spectrum of first crystal site 1



(b) Spectrum of second crystal site 2

Figure 1.4: Field swept spectra of 167-Er:YSO simulated with Easyspin.

Theory

2.1 Phenomenological Characterisation of Relaxation

2.1.1 Magnetisation Dynamics

When analysing data from a magnetic resonance experiment the underlying assumption is almost always that the Bloch equations model the behaviour of the spin that is affected by the complicated Hamiltonian given in eq. 1.2.[42] The idea behind this is that the measurement is done on a system containing many spins, with a large ratio of those being affected by the external magnetic field. Assuming ergodicity, the ensemble expectation value of the different spin components, which is the measured magnetisation, may be taken as a good indication of the expected behaviour of the individual quantum spin. If this were not true there would be no clear relation between the spin Hamiltonian and measured net magnetisation of the sample.

Bloch equations

The Bloch equations describe the coupling of the magnetic field to the magnetic moment of a paramagnetic body. We will describe their behaviour since it reflects the basic framework that is used to interpret magnetic resonance experiments. In its most simple form it is given by:

$$\dot{\mathbf{m}}(t) = \gamma \mathbf{m}(t) \times \mathbf{B}(t) \quad (2.1)$$

We assume that a strong constant field defines the z-axis of the spin system. This field is either an actual external field applied in the lab or the effective field of the hyperfine coupling. γ is the gyromagnetic ratio. We add to this model our phenomenological knowledge of how the magnetisation is affected by its environment; relaxation of the longitudinal (z) and longitudinal (x, y) components of the magnetisation characterised by T_1 and T_2 resp. Expanding the outer product:

$$\frac{dm_x}{dt} = \gamma(m_y B_z - m_z B_y) - \frac{m_x}{T_2} \quad (2.2)$$

$$\frac{dm_y}{dt} = \gamma(m_z B_x - m_x B_z) - \frac{m_y}{T_2} \quad (2.3)$$

$$\frac{dm_z}{dt} = \gamma(m_x B_y - m_y B_x) - \frac{m_z - m_0}{T_1} \quad (2.4)$$

The longitudinal component relaxes to an equilibrium, whose value depends on system properties and the strength of the constant field. The transverse components relax to zero. T_2 is also known as the dephasing or spin-spin relaxing time. Depending on the type of interaction being considered, spin-spin interaction can cause dephasing [30], spectral diffusion [43] [44] [45] or inhomogeneous broadening.[46] The latter case could be modelled into the Bloch equations by taking B_0 to be drawn from a probability distribution.[46] This is however not done here.

Now take the driving microwave field to be linearly polarised in the x direction. The total external field is:

$$\mathbf{B}(t) = B_0 \mathbf{e}_z + 2B_{mw} \cos \omega t \mathbf{e}_x$$

The main characteristics of solutions of the equation become more pronounced if we analyse the system in the frame rotating along with the microwave field. This means we apply a rotation around the z-axis over an angle ωt . In this rotating frame: $\mathbf{m}_i(t) \mapsto \tilde{\mathbf{m}}(t)$ and $\mathbf{B}(t) \mapsto \tilde{\mathbf{B}}$. We rewrite:

$$\dot{\tilde{\mathbf{m}}}(t) = \gamma \tilde{\mathbf{m}}(t) \times \tilde{\mathbf{B}} - \tilde{\mathbf{m}}(t) \times \boldsymbol{\omega} = \gamma \tilde{\mathbf{m}}(t) \times \tilde{\mathbf{B}}_{eff}$$

Here the term with $\boldsymbol{\omega} = (0, 0, \omega)^T$ comes from the time dependence that the basis vectors obtain in the rotating frame. The Bloch equations for $\tilde{\mathbf{m}}(t)$ have the same form as equations 2.1, but with an effective field given by:

$$\begin{aligned} \mathbf{B}(t) \mapsto \tilde{\mathbf{B}} &= \left(B_0 - \frac{\omega}{\gamma}\right) \mathbf{e}_z + 2B_{mw} \left(\cos^2 \omega t \mathbf{e}_x + \sin \omega t \cos \omega t \mathbf{e}_y\right) \\ &\approx \left(B_0 - \frac{\omega}{\gamma}\right) \mathbf{e}_z + B_{mw} \mathbf{e}_x \end{aligned}$$

Here the secular approximation is made, implying that fast oscillating terms are assumed to not contribute meaningfully to the dynamics being studied. Note that this requires $B_0 \gg B_{mw}$. Defining $\omega_0 = \gamma B_0$, one obtains:

$$\frac{d\tilde{m}_x}{dt} = -(\omega - \omega_0)\tilde{m}_y - \frac{\tilde{m}_x}{T_2} \quad (2.5)$$

$$\frac{d\tilde{m}_y}{dt} = \gamma B_{mw}\tilde{m}_z + (\omega - \omega_0)\tilde{m}_x - \frac{\tilde{m}_y}{T_2} \quad (2.6)$$

$$\frac{d\tilde{m}_z}{dt} = -\gamma B_{mw}\tilde{m}_y - \frac{\tilde{m}_z - m_0}{T_1} \quad (2.7)$$

Steady state solution

We obtain the steady state solutions by assuming that $\mathbf{m} \rightarrow 0$ as $t \rightarrow \infty$. These would describe the result of a CW spectroscopy experiment, in essence when the driving frequency is varied slowly enough such that the steady state is obtained at each measurement. In this case one can easily find an analytical solution by solving the linear system $A\tilde{\mathbf{m}} + \frac{m_0}{T_1}\mathbf{e}_3 = 0$ with:

$$A = \begin{pmatrix} -\frac{1}{T_2} & -(\omega - \omega_0) & 0 \\ (\omega - \omega_0) & -\frac{1}{T_2} & \gamma B_{mw} \\ 0 & -\gamma B_{mw} & -\frac{1}{T_1} \end{pmatrix}$$

One finds:

$$\tilde{m}_x(\text{ss}) = \frac{(\omega_0 - \omega)T_2^2\gamma B_{mw}m_0}{1 + T_2^2(\omega - \omega_0)^2 + T_1T_2(\gamma B_{mw})^2} \quad (2.8)$$

$$\tilde{m}_y(\text{ss}) = \frac{T_2\gamma B_{mw}m_0}{1 + T_2^2(\omega - \omega_0)^2 + T_1T_2(\gamma B_{mw})^2} \quad (2.9)$$

$$\tilde{m}_z(\text{ss}) = \frac{(1 + T_2^2(\omega - \omega_0)^2)m_0}{1 + T_2^2(\omega - \omega_0)^2 + T_1T_2(\gamma B_{mw})^2} \quad (2.10)$$

2.1.2 Measurement Techniques

Linear Response

In the previous subsection, the steady state and transient responses of a magnetic moment to AC driving were established. These results were derived in the frame of the microwave frequency. We can relate these results back to the lab frame by:

$$m_x(t) = \tilde{m}_x(t) \cos \omega t + \tilde{m}_y(t) \sin \omega t$$

From this expression, it becomes clear that $\tilde{m}_x(t)$ and \tilde{m}_y are the in-phase resp. quadrature component of the transverse magnetisation response to the driving. Consider now the case of weak driving, entering the regime of linear response theory. If we neglect terms of the order $\mathcal{O}(B_{mw}^2)$, and define $m_0 = \chi_0\omega_0/2\gamma$ in eq. 2.10 we obtain the linear susceptibility $\chi = \chi' - i\chi''$, with

$$\chi' = \frac{\chi_0}{2}\omega_0 T_2 \frac{(\omega_0 - \omega)T_2}{1 + (\omega - \omega_0)^2 T_2^2}$$

$$\chi'' = \frac{\chi_0}{2}\omega_0 T_2 \frac{1}{1 + (\omega - \omega_0)^2 T_2^2}$$

These are defined as:

$$m_x(t) = (\chi' \cos \omega t + \chi'' \sin \omega t) B_{mw} = \Re[\chi e^{i\omega t}] B_{mw}$$

By increasing the strength of B_{mw} one should observe the breakdown of linear response. The observed linewidth will become more shallow and broader, except if the homogeneous linewidth is much smaller than the inhomogeneous linewidth.[46]

In traditional ESR, magnetisation is detected by the inductor that is also used to generate the microwave field.[35] In our experiments the transmission line serves as this inductor. We introduce now the filling factor q , which is the ratio of alternating field integrated over the sample volume to the integration of the field over the total volume it extends.[47] If the inductance of the circuit without sample was L_0 , by adding the sample with susceptibility, this will change by:

$$L = L_0(1 + 4\pi q\chi(\omega))$$

The complex impedance of the inductive element obtains a real part:

$$Z = i\omega L = i\omega L_0(1 + 4\pi q\chi') + 4\pi\omega q L_0\chi''$$

The complex part of χ acts as a change in the dissipation of the inductor, which presents itself in spectroscopy as an absorption dip. From the impedance, the response of the measurement device to the presence of a paramagnetic sample can be calculated.

Signal Strength

We consider measurements done with a transmission line in the linear response regime. The Q-factor associated with transmission lines is generally

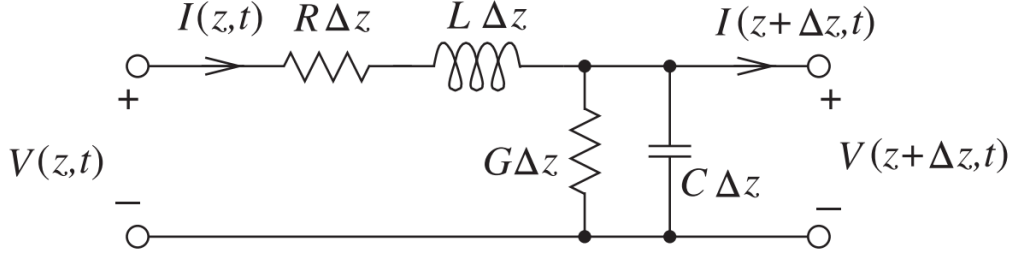


Figure 2.1: Distributed elements model of a transmission line. After Steer [49]

very low [48], and relatively strong powers are used to drive the lines, meaning that enough energy is present in the superconducting circuit to justify a classical treatment.

The distributed elements model of a general transmission line is given in figure 2.1. Using the complex impedance of each element and Kirchoff's laws, it can be shown that the voltage drop and corresponding current over each of the distributed circuits are given in the Fourier domain by [49]:

$$\begin{aligned} V(z + \Delta z, \omega) &= V(z, \omega) - R\Delta z I(z, \omega) - i\omega\Delta z L I(z, \omega) \\ I(z + \Delta z, \omega) &= I(z) - \Delta z G V(z, \omega) - i\omega\Delta z C V(z, \omega) \end{aligned}$$

In the continuous limit, we can rewrite this into a differential Helmholtz equation:

$$\begin{aligned} \frac{dV(z, \omega)}{dz} &= -(i\omega L + R)I(z, \omega) \\ \frac{dI(z, \omega)}{dz} &= -(i\omega C + G)V(z, \omega) \end{aligned}$$

Equivalently:

$$\begin{aligned} \frac{d^2V(z, \omega)}{dz^2} &= (i\omega L + R)(i\omega C + G)V(z, \omega) \\ \frac{d^2I(z, \omega)}{dz^2} &= (i\omega L + R)(i\omega C + G)I(z, \omega) \end{aligned}$$

From this, we see that the decay constant and phase associated with the wave propagation through the waveguide are given by the real resp. complex part of:

$$\gamma = \alpha + i\beta = \sqrt{(i\omega L + R)(i\omega C + G)}$$

To see that this is in fact a wave equation, one would simply need to transform back to time domain, the result of which is known as the telegraph equation. The solution is a linear combination of forward and backward traveling waves. In frequency domain:

$$V(z, \omega) = V_0^+ e^{-\gamma z} + V_0^- e^{\gamma z}$$

Here V_0^\pm denotes the voltage associated with forward resp. backward propagating waves at the input of the line. For the current:

$$\begin{aligned} I(z, \omega) &= I_0^+ e^{-\gamma z} + I_0^- e^{\gamma z} \\ &= \frac{-1}{i\omega L + R} \frac{dV(z, \omega)}{dz} = \frac{\gamma}{i\omega L + R} (V_0^+ e^{-\gamma z} - V_0^- e^{\gamma z}) \end{aligned}$$

the characteristic impedance Z_0 of the waveguide is now read off as:

$$Z_0 = \frac{V_0^+}{I_0^+} = -\frac{V_0^-}{I_0^-} = \sqrt{\frac{i\omega L + R}{i\omega C + G}}$$

For a coplanar waveguide, the capacitance and inductance can be calculated from geometric parameters.[50][51] We neglect the presence of kinetic inductance in the superconducting niobium.[52]

$$\begin{aligned} C &= 4\epsilon_0\epsilon_{eff} \frac{K(k)}{K(k')} \\ L &= \mu_0 \frac{K(k')}{4K(k)} \\ \epsilon_{eff} &= 1 + \frac{\epsilon_r - 1}{2} \frac{K(k')K(k_1)}{K(k)K(k')} \end{aligned}$$

With $\frac{K(k)}{K(k')}$ the elliptical integral, which originates from the conformal theory.[53]

$$\frac{K(k)}{K(k')} = \begin{cases} \frac{1}{\pi} \ln \left(\frac{2+2\sqrt{k'}}{1-\sqrt{k'}} \right)^{-1} & 0 \leq k \leq 0.7 \\ \frac{1}{\pi} \ln \left(\frac{2+2\sqrt{k}}{1-\sqrt{k}} \right) & 0.7 \leq k \leq 1.0 \end{cases}$$

And $k = \frac{S}{S+2W}$, $k' = \sqrt{1-k^2}$, where S, W are the signal, resp. signal-to-ground gap width of the CPW as defined in figure 2.2. ϵ_r is the relative dielectric constant of the substrate. For silicon, it is ~ 11.4 at very low temperatures.

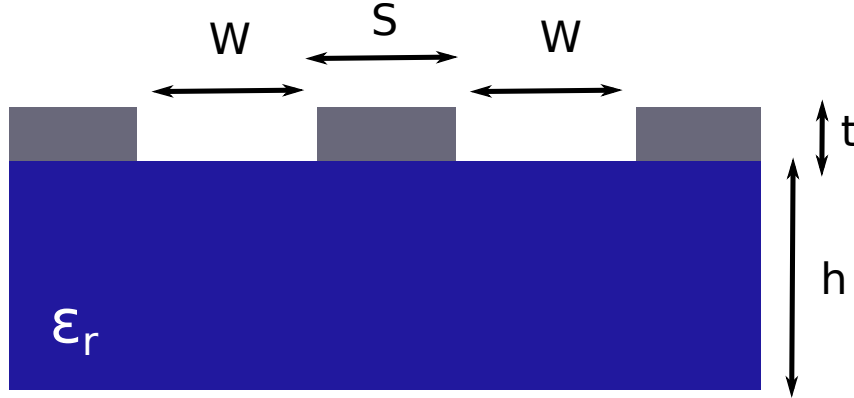


Figure 2.2: Cross section of the CPW geometry. The bottom (blue) part is the dielectric substrate, while the top is the conductor. The central conductor carries the signal, while the lateral conductors serve as ground. Ideally, the ground extends to infinity to the left and right, and that the metal thickness is $t \ll h$.

The transmission and reflection of the signal input to microwave and RF circuits are usually characterised by S -parameters. They are defined as the ratio of incoming to outgoing wave amplitudes and can be measured directly by a vector network analyser (VNA). A transmission line is an example of a symmetric 2-port network. In that case the relevant S parameters are [55]:

$$S_{12} = S_{21} = \frac{V_2^{out}}{V_1^{in}}$$

$$S_{22} = S_{11} = \frac{V_1^{out}}{V_1^{in}}$$

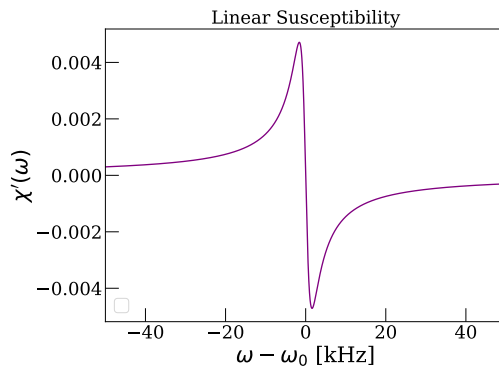
The transmission can be calculated as:

$$S_{21} = \frac{(1 - \Gamma^2)\gamma}{1 - \gamma^2\Gamma^2}$$

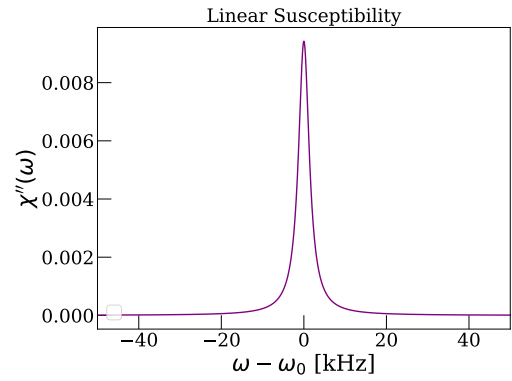
$$\Gamma = \frac{Z_0 - Z_L}{Z_0 + Z_L}$$

$$\gamma = \exp(-\ell\sqrt{(R + i\omega L)(G + i\omega C)})$$

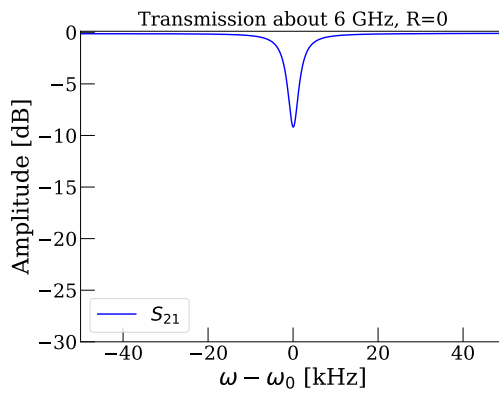
Here Z_L is the reference load, that is usually taken to be 50Ω . Using these equations one can simulate the theoretical magnetic resonance response of a coplanar transmission line coupled to a spin ensemble. This is shown in figure 2.3. What should be conveyed from differences between S_{21} for finite and zero resistance is that presence of losses might also cause a distortion of the characteristic absorption profile.



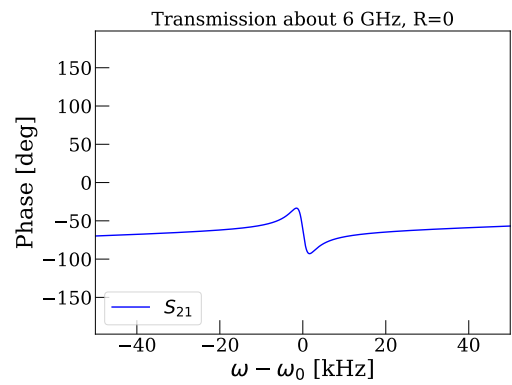
(a) Real part of susceptibility.



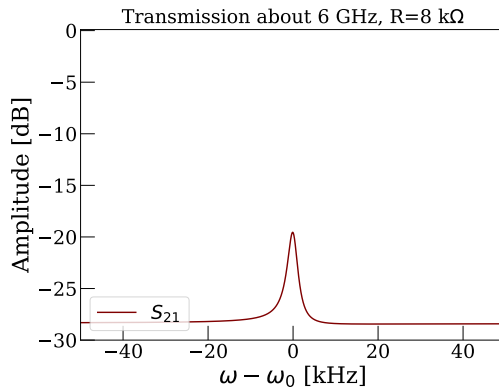
(b) Imaginary part of susceptibility.



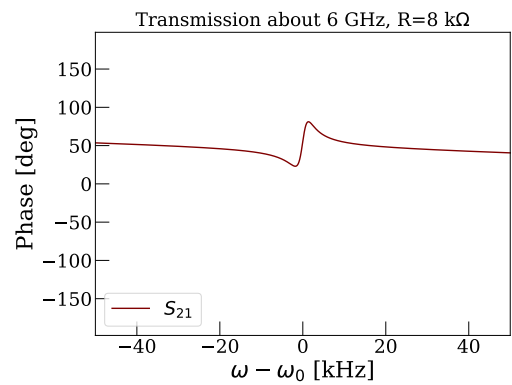
(c) Transmission Amplitude



(d) Transmission Phase



(e) Transmission Amplitude



(f) Transmission Phase.

Figure 2.3: Theoretical linear susceptibility and CPW transmission with the following parameters: $S = 20\mu\text{m}$, $W = 12\mu\text{m}$, $\epsilon_r = 11.4$, $h = 1\text{ mm}$, $\ell = 5\text{cm}$, $T_1 = 1\text{ s}$, $T_2 = 0.1\mu\text{s}$, $\omega_0 = 6\text{ GHz}$, $\chi_0 = 5 \cdot 10^{-6}$, $G = 50\ \mu\text{S/m}$ and R is indicated for two different cases. These parameters will give: $C = 16\text{ nF/m}$ and $L = 0.6\ \mu\text{H/m}$

2.2 Spin Description

2.2.1 Ensemble Treatment

In section 1.2 a treatment of the spin Hamiltonian was given. This Hamiltonian can in principle be deduced from the atomic properties of the paramagnetic ion and the host crystal. It tells us at which frequencies transitions will occur, but not their linewidths. In the previous section the Bloch equations were covered, describing the interaction of classical magnetic moments with an external field. This required *ad hoc* terms describing the transverse and longitudinal relaxation. In this section the longitudinal relaxation time is derived. The measurements presented in chapter 3 were not performed on a single spin, but on a thermodynamic ensemble of spins. Therefore a natural pathway to describing this ensemble is given by the density matrix formalism, which allows for the representation of statistical ensembles as mixed states.[56]

The fact that we are dealing with an ensemble is taken into account by introducing a density matrix that appropriately models the statistics of this ensemble. For example, a spin ensemble in thermal equilibrium can be modeled by $\rho = \otimes_{\ell} \rho_{\ell}$, with the single spin thermal density matrix: $\rho_{\ell} = e^{-\frac{H}{k_B T}}$.

In the presence of interactions such a tensor product state will get entangled over time, but in the standard literature this entanglement is usually neglected. [23] Within this simplification, the derivations can be based upon the dynamics of a single spin coupled to a bath, which can be solved analytically in relatively many cases. Part of this research work is seeking how to improve upon this simplification. The results obtained by this bath model are however reproduced here, to clarify exactly where doubtful assumptions are made and to give an introduction to therelevant formalism.

While the results reproduced below are to be found in most classic magnetic resonance literature, the way they are derived is not. Usually, an approach based on Fermi's golden rule is taken. This is not done here because it is the author's conviction that this leaves many of the non-trivial mathematical assumptions hidden. To provide a strategic view of the luscious valleys below, altitude must be gained by making a detour.

We note here that we will work with the convention $\hbar = 1$, and introduce our notation for the spin operators $S_{\ell}^x, S_{\ell}^y, S_{\ell}^z$ for a spin ℓ , that obey the relation $[S_{\ell}^i, S_{\ell'}^j] = \epsilon_{ijk} \delta_{\ell\ell'} S_{\ell}^k$.

Also important are the spin excitation and relaxation operators $S_\ell^\pm = S_\ell^x \pm iS_\ell^y$, that obey $[S_\ell^\pm, S_{\ell'}^z] = \pm\delta_{\ell\ell'}S_\ell^\pm$ and $[S_\ell^-, S_{\ell'}^+] = \delta_{\ell\ell'}S_\ell^z$.

Redfield Equation

The evolution of the density matrix is given by the quantum Liouville theorem:

$$\frac{d\rho}{dt} = -i[H, \rho(t)] \quad (2.11)$$

We assume that the Hamiltonian is of the form $H = H_S + H_B + H_I$, where H_S and H_B act exclusively on the Hilbert space of the spin or bath respectively.

With the unitary $U(t) = \exp i(H_S + H_B)t$ we transform the Hamiltonian to a rotating frame, applying the well-known relation:

$$H \mapsto H(t) = U(t)HU^\dagger(t) + i\frac{dU(t)}{dt}U^\dagger(t)$$

In general this will be of the form $H(t) = H_I(t) = U(t)H_IU^\dagger(t)$. By applying the Leibniz rule, one finds that the evolution of the density matrix $\rho_{\text{rot}}(t) = U(t)\rho_{\text{lab}}(t)U^\dagger(t) \stackrel{\text{redef.}}{=} \rho(t)$ in this frame is given by:

$$\frac{d\rho(t)}{dt} = -i[H_I(t), \rho(t)]$$

It has the formal solution:

$$\rho(t) = \rho(0) - i \int_0^t [H_I(\tau), \rho(\tau)] d\tau$$

From this, we obtain an equation of motion for the spin density matrix by taking the derivative again and tracing out the bath.

$$\frac{d\rho_S(t)}{dt} = - \int_0^t \text{tr}_B([H_I(t), [H_I(\tau), \rho(\tau)]]) d\tau \quad (2.12)$$

Continuing onward, non-trivial assumptions about the nature of the environment have to be made. Namely, we will assume that while the spin is being affected by the bath, the spin does not cause a change in the dynamics of the bath. Mathematically speaking, the state of the bath is stationary, i.e. time-independent and it does not become entangled with the spin. Physically speaking, it implies that the bath contains significantly more degrees of freedom than the spin system, such that the statistical behaviour of the bath

overshadows the entanglement of its individual subsystems, to the degree that it becomes unobservable. This is known as the Born approximation [57] and changes eq 2.12 into:

$$\frac{d\rho_S(t)}{dt} = - \int_0^t \text{tr}_B([H_I(t), [H_I(\tau), \rho_S(\tau) \otimes \rho_B(0)]] d\tau$$

We also introduce the Markov approximation for the dynamics of the spin. A process is called Markovian if it obeys the Kolmogorov criterion. Mathematically this is expressed as follows. If $P(x, t)$ denotes the probability for an observable to be measured having the value x at time t , then for these probabilities it holds that:

$$P(x, t''|z, t) = \sum_y P(x, t''|y, t')P(y, t'|z, t) \text{ for } t < t' < t''$$

The implication is that the spin-bath interaction is practically memoryless, and the future state of the spin is fully determined by its current one. We can then approximate $\rho_S(\tau) \approx \rho_S(t)$ in the integrand and take the upper limit of the integral to go to infinity, obtaining:

$$\frac{d\rho_S(t)}{dt} = - \int_0^\infty \text{tr}_B([H_I(t), [H_I(\tau), \rho_S(t) \otimes \rho_B(0)]] d\tau \quad (2.13)$$

This result (eq. 2.13) is known as the Redfield equation, and it will be used here to derive the standard expression for the relaxation time T_1 .

2.2.2 Spin-Lattice Relaxation

The term spin-lattice relaxation is an appropriate synonym for longitudinal relaxation, since in contrast to electronic transitions, there can be no relaxation of a Kramers doublet by direct coupling to the electromagnetic field.[23] Even for non-Kramers transitions the direct coupling to photons is too weak to explain the relaxation times observed in experiments. Instead, it is now generally accepted that the relaxation instead occurs through interaction with lattice vibrations, mediated by the crystal field. Initially, it was suggested this happens via a direct magnetic interaction between the spin and the magnetic component of the oscillating crystal field.[58] It was shown later that would result in relaxation times too long to comply with experimental results. Instead, the electrostatic interaction between the electron and the field is more dominant, which can affect the spin degree of freedom through spin-orbit coupling.[59][60]

Using the methods of second quantisation the lattice vibrations of the strain field can be represented as a thermal bath of quantised modes. This is the well-known Debye model. [62] The quasiparticles connected to this modes k are called phonons, and are mathematically described using creation a_k^\dagger and annihilation a_k operators, that obey the Weyl-Heisenberg algebra $[a_k, a_k^\dagger] = 1$.

The Hamiltonian is taken here to describe the coupling between a single spin of frequency ω_0 and the phonon bath is given by [27]:

$$H = -\omega_0 S^z + \sum_k \omega_k a_k^\dagger a_k + \sum_k (\bar{g}_k a_k S^+ + g_k a_k^\dagger S^-) \quad (2.14)$$

The coupling constants g_k relate to the energy spectral density of acoustic phonons as $\sum_k |g_k|^2 = \int J(\omega) d\omega$. [61] In the isotropic Debye model the latter is given by [62][63]:

$$J(\omega) = \alpha \frac{3V}{2\pi^2 v_s^3} \omega^3 \theta(\omega_D - \omega)$$

Here v_s is the material speed of sound and α is a coupling constant. In reality, v_s is not isotropic and also is different for longitudinal and transverse phonons. This would change the prefactor in $J(\omega)$, while the proportionality stays the same. In the following calculations, these subtleties are ignored.

This Hamiltonian corresponds to the so-called direct process, where the interaction involves only a single resonant phonon. Other relaxation mechanisms are the non-resonant Raman and Orbach processes, involving multiple of phonons. Both are strongly suppressed at millikelvin temperatures. [44]

The interaction part of the Hamiltonian in the rotating frame takes the form:

$$H_I(t) = \sum_k (\bar{g}_k e^{-i(\omega_k - \omega_0)t} a_k S^+ + g_k e^{i(\omega_k - \omega_0)t} a_k^\dagger S^-)$$

The innermost commutator in eq. 2.13 will give:

$$\begin{aligned} [H(\tau), \rho(t)] = & \sum_k g_k e^{i(\omega_k - \omega_0)t} ((S^- \rho_S(t))(a_k^\dagger \rho_B) - (\rho_S(t) S^-)(\rho_B a_k^\dagger)) \\ & + \bar{g}_k e^{-i(\omega_k - \omega_0)t} ((S^+ \rho_S(t))(a_k \rho_B) - (\rho_S(t) S^+)(\rho_B a_k)) \end{aligned}$$

When calculating the second commutator the exponential time dependence of the operators will give you terms of two kinds, namely $e^{\pm i(\omega_k - \omega_0)(t - \tau)}$ and $e^{\pm i(\omega_k - \omega_0)(t + \tau)}$. The latter corresponds to terms containing $\langle (a_k^\dagger)^2 \rangle$, $\langle a_k^2 \rangle$, which are zero since the thermal density matrix is diagonal in the Fock basis.

We also drop terms that mix different phonon modes, since we expect their expectation values, $\text{tr}_B(a_k^\dagger a_\ell \rho_B) = \langle a_k^\dagger a_\ell \rangle$, etc. to be zero. We use the cyclic property of the trace to sort Weyl resp. non-Weyl ordered phononic terms together.

$$\begin{aligned} \frac{d\rho_S(t)}{dt} = & - \int_0^\infty d\tau \sum_k |g_k|^2 \\ & \times \text{tr}_B \left(e^{-i(\omega_k - \omega_0)(t - \tau)} \left((S^+ S^- \rho_S(t) - S^- \rho_S(t) S^+) a_k a_k^\dagger \rho_B \right. \right. \\ & \quad \left. \left. + (\rho_S(t) S^- S^+ - S^+ \rho_S(t) S^-) a_k^\dagger a_k \rho_B \right) \right. \\ & \left. + e^{i(\omega_k - \omega_0)(t - \tau)} \left((\rho_S(t) S^+ S^- - S^- \rho_S(t) S^+) a_k a_k^\dagger \rho_B \right. \right. \\ & \quad \left. \left. + (S^- S^+ \rho_S(t) - S^+ \rho_S(t) S^-) a_k^\dagger a_k \rho_B \right) \right) \end{aligned}$$

Applying the commutator $[a_k, a_k^\dagger] = 1$ results in:

$$\begin{aligned} \frac{d\rho_S(t)}{dt} = & - \int_0^\infty d\tau \sum_k |g_k|^2 \\ & \times \text{tr}_B \left(e^{-i(\omega_k - \omega_0)(t - \tau)} \left((S^+ S^- \rho_S(t) - S^- \rho_S(t) S^+) \right. \right. \\ & \left. \left. + (S^+ S^- \rho_S(t) - S^- \rho_S(t) S^+ + \rho_S(t) S^- S^+ - S^+ \rho_S(t) S^-) a_k^\dagger a_k \rho_B \right) \right. \\ & \left. + e^{i(\omega_k - \omega_0)(t - \tau)} \left((\rho_S(t) S^+ S^- - S^- \rho_S(t) S^+) \right. \right. \\ & \left. \left. + (\rho_S(t) S^+ S^- - S^- \rho_S(t) S^+ + S^- S^+ \rho_S(t) - S^+ \rho_S(t) S^-) a_k^\dagger a_k \rho_B \right) \right) \end{aligned}$$

For a two-level system, the density matrix can be represented as a vector on the Bloch sphere. Specifically for a spin $\frac{1}{2}$ transition, the components of this vector correspond exactly to those of the expectation value of the spin vector. Mathematically this is expressed in the ordered basis $\{|\uparrow\rangle, |\downarrow\rangle\}$ as:

$$\rho_S(t) = \begin{pmatrix} \frac{1}{2} + \langle S^z \rangle(t) & \langle S^x \rangle(t) - i \langle S^y \rangle(t) \\ \langle S^x \rangle(t) + i \langle S^y \rangle(t) & \frac{1}{2} - \langle S^z \rangle(t) \end{pmatrix}$$

Using the matrix representations $S^- = |\uparrow\rangle\langle\downarrow|$, $S^+ = |\downarrow\rangle\langle\uparrow|$, one finds after a tedious calculation:

$$\begin{aligned} \frac{d\rho_S}{dt} = & - \int_0^\infty d\tau \sum_k |g_k|^2 (2\langle n_k \rangle + 1) \\ & \times \begin{pmatrix} 2\langle S^z \rangle \cos(\omega_k - \omega)(\tau - t) & e^{-i(\omega_k - \omega_0)(t - \tau)} (\langle S^x \rangle - i\langle S^y \rangle) \\ e^{i(\omega_k - \omega_0)(t - \tau)} (\langle S^x \rangle + i\langle S^y \rangle) & -2\langle S^z \rangle \cos(\omega_k - \omega)(\tau - t) \end{pmatrix} \\ & + |g_k|^2 \begin{pmatrix} -\cos(\omega_k - \omega_0)(\tau - t) & 0 \\ 0 & \cos(\omega_k - \omega_0)(\tau - t) \end{pmatrix} \end{aligned}$$

We take care of the time integral by applying the Fourier relation:

$$\int_0^\infty d\tau e^{\pm i(\omega_k - \omega_0)\tau} = \delta(\omega_k - \omega_0)$$

We take the continuum limit in k , and transform the sum over coupling terms to an integral over the energy spectral density:

$$\sum_k |g_k|^2 (2\langle n_k \rangle + 1) \delta(\omega_k - \omega_0) = \int_0^\infty J(\omega) (2n(\omega) + 1) \delta(\omega - \omega_0) d\omega$$

In the Debye model the phonon distribution function is given by:

$$n(\omega) = \frac{1}{e^{\omega/k_B T} - 1}$$

such that $2n(\omega) + 1 = \coth\left(\frac{\omega}{2k_B T}\right)$. What remains is:

$$\begin{aligned} \frac{d\rho_S}{dt} = & J(\omega_0) \coth\left(\frac{\omega_0}{2k_B T}\right) \\ & \times \begin{pmatrix} -2\langle S^z \rangle & (\langle S^x \rangle - i\langle S^y \rangle) \\ (\langle S^x \rangle + i\langle S^y \rangle) & 2\langle S^z \rangle \end{pmatrix} \\ & + J(\omega_0) \begin{pmatrix} 1 & 0 \\ 0 & -1 \end{pmatrix} \end{aligned}$$

From the differential equation for ρ_S , one can read off the differential equations for the individual spin components:

$$\begin{aligned} \frac{d}{dt} \langle S^x \rangle &= -J(\omega_0) \coth\left(\frac{\omega_0}{2k_B T}\right) \langle S^x \rangle \\ \frac{d}{dt} \langle S^y \rangle &= -J(\omega_0) \coth\left(\frac{\omega_0}{2k_B T}\right) \langle S^y \rangle \\ \frac{d}{dt} \langle S^z \rangle &= -2J(\omega_0) \coth\left(\frac{\omega_0}{2k_B T}\right) \left(\langle S^z \rangle - \frac{1}{2}\right) \end{aligned}$$

Now one can calculate or read-off the characteristic relaxation time to be $\frac{1}{T_1} = 2J(\omega_0) \coth \frac{\omega}{2k_B T}$, which goes as:

$$\frac{1}{T_1} \sim \omega^3 \coth \frac{\omega}{2k_B T}$$

This is the correct result for non-Kramers ions. In case the relevant states of the two-level system are spin degenerate a correction must be applied, to obtain the result measured in experiments.[21] [24] The main idea of the correction is sketched below.

Before spin degeneracy is broken, the level structure of the Kramers ion is determined by the splitting of the free atom states by the crystal field. Take the two lowest crystal field levels to correspond to basis states $|0\rangle$ and $|1\rangle$, that the crystal fields splits by an energy Δ . Kramers degeneracy means that a magnetic field would split these states further into $|0 \uparrow\rangle, |0 \downarrow\rangle$ and $|1 \uparrow\rangle, |1 \downarrow\rangle$. Let this smaller splitting be equal to $2\mu_B B_{eff} = \hbar\omega$, where \mathbf{B}_{eff} comes from either $\mathbf{B} \cdot \mathbf{g}$ or $\mathbf{I} \cdot \mathbf{A}$, or both. The crystal field does not break time-reversal symmetry, so at first glance we expect $\langle 0 \uparrow | V_{cf} | 0 \downarrow \rangle = 0$ and $\langle 1 \uparrow | V_{cf} | 1 \downarrow \rangle = 0$. This seems contradictory since the entire relaxation theory above was based upon lattice vibrations interacting with the spin degree of freedom through the crystal field.

A solution to the problem can be found by using a more refined form of perturbation theory, developed in for example Heitler (1944) [64]. The matrix elements of V_{cf} between e.g. $|0 \uparrow\rangle$ and $|0 \downarrow\rangle$ vanish, but these states can still interact through V_{cf} by means of an intermediate state. For $|0 \uparrow\rangle, |0 \downarrow\rangle$ these would be the $|1 \uparrow\rangle, |1 \downarrow\rangle$ states, since $\langle 0 | V_{cf} | 1 \rangle$ do not vanish. In leading order, the effective matrix is given by summing over intermediate states $|\phi\rangle$:

$$\begin{aligned} \langle 0 \uparrow | V_{cf} | \downarrow \rangle_{eff} &= \sum_{\phi} \frac{\langle 0 \uparrow | V_{cf} | \phi \rangle \langle \phi | V_{cf} | 0 \downarrow \rangle}{E_{0\downarrow} - E_n} \\ &= \frac{\langle 0 \uparrow | V_{cf} | 1 \downarrow \rangle \langle 1 \downarrow | V_{cf} | 0 \downarrow \rangle}{\Delta} - \frac{\langle 0 \uparrow | V_{cf} | 1 \uparrow \rangle \langle 1 \uparrow | V_{cf} | 0 \downarrow \rangle}{\Delta - \frac{1}{2}\hbar\omega} \end{aligned}$$

The change in sign from the second term comes from the subtleties in how $\langle 1 \uparrow | V_{cf} | 0 \downarrow \rangle$ from its Hermitian conjugate. Depending if the transition between $|0\rangle$ and $|1\rangle$ occurs (mathematically speaking) before or after the spin-flip, determines if the spin-orbit Hamiltonian is applied before or after the orbit-lattice Hamiltonian. It can be shown that the difference between the two cases causes a change in sign.[65]

Taking $\hbar\omega$ to be much smaller than Δ , the interaction strength will scale as:

$$\langle 0 \uparrow | V_{cf} | \downarrow \rangle_{eff} \sim \frac{\hbar\omega}{\Delta} \langle 0 \uparrow | V_{eff} | \downarrow \rangle$$

To take this into account, the coupling terms must be rescaled as: $|g_k|^2 \mapsto \frac{\omega^2}{\Delta^2} |g_k|^2$. One obtains for Kramers ions:

$$\frac{1}{T_1} \sim \frac{\omega^5}{\Delta^2} \coth \frac{\omega}{2k_B T}$$

2.2.3 Phonon Bottleneck

In the previous section, the resonant energy transfer from the spin ensemble into lattice vibrations was extensively discussed. Briefly mentioned were the different mechanisms of non-resonant spin-lattice relaxation and it was argued that there are not relevant at experiments done in a dilution refrigerator. In deriving the rate for the more relevant direct process the following assumptions were made to justify certain necessary approximations, namely:

- The phonon bath contains significantly more degrees of freedom than the spin system, such that the Born approximation can be made.
- The phonon bath is memoryless, such that the Markov approximation can be made.

The first assumption is usually wrong.[22] To understand how this will affect the ensemble energy transfer we must also consider the heat capacities of the respective systems. For spin 1/2 and phonon systems with frequency ω in thermal equilibrium with a temperature T these are given by resp.:

$$C_{\text{spin}} = k_B \left(\frac{\hbar\omega}{k_B T} \right)^2 \text{sech}^2 \frac{\hbar\omega}{2k_B T} \quad (2.15)$$

$$C_{\text{phonon}} = k_B \left(\frac{\hbar\omega}{k_B T} \right)^2 \text{cosech}^2 \frac{\hbar\omega}{2k_B T} \quad (2.16)$$

In the limit $\hbar\omega \gg k_B T$, the heat capacities equalise. *Vis à Vis* the ratio of spin to phonon mode density, this result implies that at cryogenic temperatures the relaxation of excited spins will cause a net heating of the resonant band of the phonon bath, and induce a non-equilibrium in the phonon mode occupation density. The heating of the phonon bath limits the rate T_1

by which the spins can relax. This limitation on T_1 induced by the phonon bath dynamics is the phonon bottleneck that was mentioned in the introduction. The introduction of a scaled T_1 , with the scaling depending on the ratio of the heat capacities.[66] But strictly speaking, the heat capacities given in eq. 2.16 assume a thermal distribution. It is not immediately clear if this approach is justified in describing the pump-probe measurements of this work for example. This issue is considered in more depth in section 2.3.

Another interesting aspect in the standard description of the bottleneck is the origin of the phonon relaxation time T_{ph} , which is usually added *ad hoc* to the theory. There exist several potential relaxation mechanisms that could determine the actual value of T_{ph} . Below the two possible mechanisms for the relaxation of acoustic phonons are mentioned. Before going into those, it is mentioned here that defect scattering does not contribute to the relaxation rate since it is mostly elastic, and only causes the momentum distribution to become more anisotropic.[67]

Spontaneous Relaxation

What is referred to as spontaneous relaxation are the general 3 and 4 phonon scattering interactions that transfer energy from one mode \mathbf{q}_1 or two modes $\mathbf{q}_1 + \mathbf{q}_2$ into two other modes $\mathbf{q}_3 + \mathbf{q}_4$, under the restriction of momentum and energy conservation. The up-scattering of phonons into higher frequency modes with $\hbar\omega > k_B T$ is suppressed.[68][69][70] Consider the case of 3 phonon decay:

$$\omega(\mathbf{q}_1) \longrightarrow \omega(\mathbf{q}_2) + \omega(\mathbf{q}_3) \quad (2.17)$$

Energy conservation implies.

$$\omega(\mathbf{q}_1) = \omega(\mathbf{q}_2) + \omega(\mathbf{q}_3) \quad (2.18)$$

The most occurring case is that the three momenta are not colinear. The triangle inequality then states that $\|\mathbf{q}_1\| \leq \|\mathbf{q}_2\| + \|\mathbf{q}_3\|$. Acoustic phonons obey a linear dispersion relation, which implies that.

$$\frac{\omega(\mathbf{q}_1)}{v_1} \leq \frac{\omega(\mathbf{q}_2)}{v_2} + \frac{\omega(\mathbf{q}_3)}{v_3} \quad (2.19)$$

To obey all of the equations 2.17,2.18,2.19, the velocity v_1 must be greater than both of v_2 and v_3 . A fact that was mentioned but neglected in subsection 2.2. is that longitudinal and transverse phonons have a different sound velocity, with $v_\ell > v_t$. This leads to the conclusion that only longitudinal phonons can relax through a 3-phonon decay. Transverse phonons

can only decay in a 4-phonon process, or by undergoing a 3-phonon excitation process into a longitudinal phonon mode of higher energy. Both of these processes have much slower rates than the 3-phonon decay, 6 orders of magnitude slower some estimates show. [71][67]

In literature the rate of the 3 phonon decay is estimated from Fermi's golden rule to go as:

$$\frac{1}{\tau_{3ph}} = \gamma \omega_D \left(\frac{\omega}{\omega_D} \right)^5 \quad (2.20)$$

with $\gamma \approx 0.2$. [75]

The Debije frequency of a crystal is related to the average sound velocity and its melting point. For YSO it is $\nu_D \approx 12$ THz.[63] So for a longitudinal phonon in the ESR regime of $\nu = 10$ GHz, this would mean: $\tau_{3ph} \approx 1$ hour. For a $\nu = 1$ GHz longitudinal phonon it will be on the order of 10 years.

As was mentioned before, T_1 of some RE dopants in YSO has been shown to be on the order of days in some experiments.[5] Therefore, if spontaneous decay can realistically be the mechanism that limits the phonon-lattice relaxation might highly depend on the dopant being used, and on the transition frequency that is being measured. It is still unclear what role the transverse phonons would play in that case. Even if the longitudinal phonons decay faster than $1/T_1$, the bottleneck might still be caused by the accumulation of transverse phonons.[72] That is unless such transverse phonon heating somehow enhances the phonon-spin scattering rate. To make more precise predictions the actual scattering mechanism by which phonons and spins interact should be studied in more detail, as was done by for example in the works of Chudnovsky and others.[76][77][78][79][80] All in all, if these estimations hold any merit it seems unlikely that spontaneous decay is the mechanism by which the resonant phonon bath relaxes. However, if they do, it should be visible by a general downward movement in the saturation of the ESR spectrum, due to phonons cross-relaxing into lower bands.

Relaxation through Thermal Contact

When mentioning the concept of a bath temperature this was done in a thermodynamic sense. The quantum mechanical system under study should be in good thermal contact with a classical system that serves as a thermostat. This thermostat presently being a dilution refrigerator and the thermal contact is provided by the interface between the crystal and the silicon chip, the latter being kept at a constant temperature by the cooling power of the dilution refrigerator. This is the concept of Kapitza boundary resistance, where

the heat flux is related to the temperature difference.[81]. It can be motivated from a microscopic viewpoint by viewing the heat flux as a net rate of phonons scattering across the interface as acoustic waves. In this view, the heat flux across the interface between materials 1 and 2 is given by:

$$\frac{dQ}{dt} = \frac{1}{2}Av_{s1}\Gamma \int (n_1(\omega) - n_2(\omega))\frac{d\omega}{2\pi}$$

Where v_{s1} is the speed of sound in material 1, A is the interface cross-section, and $n_i(\nu)$ is the frequency-dependent phonon density per unit volume. Γ is given by integrating the Fresnel reflection coefficient over all incoming and outgoing scattering angles. For YSO it can be estimated to be $\Gamma = 0.3$. [82] Now consider there to only be a finite difference in the distributions $n_i(\omega)$ at a single frequency $\omega = \omega_0$. For a YSO crystal of dimensions $1 \times 1 \times 1 \text{ mm}^3$, where one face is in thermal contact with silicon, this leads to the following rate equation for the number of phonons at ω_0 that traverse the boundary:

$$\frac{dN(\omega)}{dt} \approx 0.14\text{sec}^{-1} \cdot (N_1(\omega) - N_2(\omega))$$

This rough estimate implies that if nonequilibrium phonons are generated by the spin ensemble at a rate $1/T_1$, these phonons will decay out of the crystal at a rate $1/T_{ph}$ that is roughly 10 times slower.

From these estimations, it seems more likely that relaxation through the thermal contact limits the value of T_{ph} , instead of spontaneous decay mechanisms. For the specific case of a YSO-Silicon interface this opens up the possibility of a bottleneck effect, although not a very significant one. In this context, it must be noted that recent and not-so-recent experiments have shown that the acoustic scattering approach overestimates the interface scattering rate, sometimes significantly.[83][84] In addition, the thin superconductor covering the Silicon will also slow down the process. So the above calculations might only be sufficient to point out if a phonon bottleneck is possible at all, and by which mechanism. It should not be used to estimate how strong the effect will be.

2.3 Thermodynamic Model

2.3.1 Nonequilibrium Statistical Operator

In the previous subsection it was argued that the standard models for the relaxation do not cover all of the magnetisation behaviour that is observed in experiments at low temperatures. In this section a different model is introduced that might relate better to modern experiments. It makes use of the concept of a nonequilibrium statistical operator (NSO), first introduced by Zubarev.[85][86] An application of the NSO to the problem of spin relaxation has already been attempted before by Buishvili and others.[87][88][89][90][91][92]. Experimental verification of these older models is however lacking. There are other aspects that make them unusable for the describing the experiments done for this thesis. Namely as will be described below, there are two ways of applying the NSO method. The first method, used by all of the literature cited above, is to derive equations for thermodynamic quantities, such as for example spin temperature. The problem with this approach is that the resulting system of equations only becomes somewhat analysable when the high-temperature approximation is invoked. It was shown that if the same method is applied without this approximation some more fundamental problems appear[93]. In addition, it does not allow for a straightforward treatment of decoherence processes. Therefore, the method applied in this work is that of deriving kinetic equations for quantum mechanical operators, whose expectation values are with respect to quasi-thermal states. Below the general idea behind the NSO method is explained first, and afterward the kinetic equations for the spin-lattice system are derived.

First some words on the exact purpose of the theorising done below. A true quantum theoretical underpinning of thermodynamics is still controversial, and the author does not hold the pretense to clarify these issues anyhow here.[94] Instead, our aim *in primis et ante omnia* is to find a correction to the Bloch equations. The correction might be informed by quantum mechanics but only serves to slightly tune what we expect to measure in experiments *vis à vis* the phonon bottleneck.

Relevant Entropy

To explain the essence of the NSO, we start by considering the thermal equilibrium solutions to the Liouville equation already presented in section 2.2.

$$\frac{d\rho}{dt} = -i[H, \rho(t)]$$

In the density matrix formalism, the entropy is defined as:

$$S[\rho] = -k_B \text{tr}(\rho \ln(\rho))$$

The thermal equilibrium solution ρ_{eq} to the Liouville equation should satisfy the following constraints:

$$\begin{aligned} S[\rho_{eq}] &= \max_{\rho} S[\rho] \\ \langle C_n \rangle_{th} &= \text{tr}(\rho_{eq} C_n) \\ \text{tr}(\rho_{eq}) &= 1 \end{aligned}$$

Here $\{C_n\}$ is the set of integrals of motion. The functional form of ρ_{eq} is found from the variational principle by applying Lagrange's method of multipliers given these constraints. For example, the temperature $\lambda_n = T$ is the multiplier ensuring conservation of energy $\langle C_n \rangle_{eq} = E$. The solution ρ_{eq} will then be given by the Gibbs distribution:

$$\rho_{eq} = \frac{1}{Z} e^{-\sum_n \lambda_n C_n}$$

where the partition sum $Z = \text{tr}(\exp(-\sum_n \lambda_n C_n))$ ensuring normalisation. This is all textbook material.

In regular quantum theory the expectation of an observable A should at any time t be given by:

$$\langle A \rangle(t) = \begin{cases} \text{tr}(\rho(t)A) & \text{Schrödinger picture} \\ \text{tr}(\rho A(t)) & \text{Heisenberg picture} \end{cases}$$

It seems natural to demand that if the initial state of system is not the thermal equilibrium, the Liouville equation would describe the relaxation to equilibrium. According to the second law of thermodynamics, the expectation value of the entropy $S(t) = \langle \ln \rho(t) \rangle$ should be a monotonically increasing function of time. However using the standard formalism, one can easily show that $\dot{S}(t) = 0$ for all t if ρ obeys the Liouville equation.

In unaltered form, the density matrix formalism is unable to describe the relaxation to equilibrium of a closed system. Solving this discrepancy is the goal of the NSO.[85] The main idea is to extend the constraints on ρ_{eq} to not only include the conserved observables $\{C_n\}$, but an extended set of relevant observables $\{R_n\}$. Some $\langle B_n \rangle(t)$ may increase in time, as well as

their Lagrange multipliers $\lambda_n(t)$. The solution is an extended Gibbs distribution, which is called the relevant statistical operator:

$$\rho_{rel} = \frac{1}{Z(t)} e^{-\sum_n \lambda_n(t) R_n}$$

Defining the relevant entropy $S_{rel}(t)$ analogous to the thermodynamic entropy and using the solution for $\rho_{rel}(t)$ given above, one can show that:

$$\frac{dS_{rel}(t)}{dt} = \sum_n \lambda_n(t) \langle \dot{R}_n \rangle (t) = i \sum_n \lambda_n(t) \langle [H, R_n] \rangle (t)$$

This derivative can be finite as long as some of $\langle \dot{R}_n \rangle (t)$ are, in contrast to the thermodynamic entropy. ρ_{rel} does not obey the Liouville equation. It was the insight of Zubarev that ρ_{rel} should be added to the Liouville equation as initial condition.[95]

Zubarev Initial Conditions

Generally, the evolution of the density matrix is given by:

$$\rho(t) = U(t; t_0) \rho(t_0) U^\dagger(t; t_0)$$

With the unitary generator defined as $U(t; t_0) = \mathcal{T}_\tau \exp(-i \int_{t_0}^t H(\tau) d\tau)$. We now assume that at some initial time t_0 , the state of the system was given by $\rho_{rel}(t_0)$. The following objections appear:

- Is there any physical reality to this construction of ρ_{rel} ? If so which R_n to choose?
- Does the assumed initial condition for $\rho(t)$ reproduce realistic dynamics?

The argument that justifies the steps taken above goes back to Bogoliubov.[96][97] In his monograph on statistical dynamics, he introduces the following concepts:

- Within the system evolution to equilibrium there exists a hierarchy of relaxation times.
- During the evolution of a thermodynamic system, a weakening of correlations occurs.

The hierarchy of relaxation times implies that even before the system reaches a macroscopically defined equilibrium state, defined by thermodynamic quantities, the system will already reach a state where single-particle distribution

functions can be defined. The distribution functions properly start describing the kinetics of the particle ensemble or subensemble, while a bulk system temperature is not yet definable. For our specific problem, it allows us to state that each phononic mode k can be treated as a subsystem with its own ensemble energy $\langle H_k \rangle(t)$ and temperature $T_k(t)$, which are well defined since ρ_k is a thermal distribution. Because equilibrium has not been reached yet $T_k \neq T$, so these quantities are allowed to change in time until $T_k = T_k = T$. The mode temperatures and analogous quantities defined using the Gibbs distribution for relevant parameters seem physical since they obey thermodynamic relations and tend to expected equilibrium values as $t \rightarrow \infty$. There exists however no thermometer that can measure T_k .

There remains the question of choosing proper R_n for $\rho_{rel}(t_0)$. The principle of weakening initial correlations states that any correlation important for $\rho(t)$, but not implemented in $\rho_{rel}(t_0)$ will anyway be produced by the dynamical evolution of the system. Crucial is only that $\{C_n\} \subset \{R_n\}$, but the dynamics of any unconserved observables will occur in the theory correctly due to ergodicity. The more complete the set $\{R_n\}$ is, the faster the physical behaviour for $\rho(t)$ is reproduced, but to ensure that the choice of R_n does not influence $\rho(t)$ the proper form of the NSO is found by taking the limit $t_0 \rightarrow -\infty$. Then according to a theorem due to Abel[98], this is equivalent to stating:

$$\rho_{NSO}(t) = \lim_{\epsilon \rightarrow 0} \rho_\epsilon(t) = \lim_{\epsilon \rightarrow 0} \epsilon \int_{-\infty}^t e^{\epsilon(\tau-t)} U(t; \tau) \rho_{rel}(\tau) U^\dagger(t; \tau) d\tau \quad (2.21)$$

In this formulation $\rho_{rel}(t_0)$ can be taken as initial condition on $\rho_{NSO}(t)$ for any $-\infty < t_0 < t$. Taking the time derivative of ρ_ϵ leads to adjusted form of the Liouville equation:

$$\frac{d\rho_\epsilon(t)}{dt} = -i[H, \rho_\epsilon(t)] - \epsilon(\rho_\epsilon(t) - \rho_{rel}(t))$$

One sees that as the source term appears on the right-hand side. Analogous to the role of a Lindblad operator, the source term breaks the time reversibility of the quantum evolution to allow for a thermal equilibrium to appear.[99][100]

2.3.2 Application to the Spin-Lattice Interaction

Now that there has been argued for the existence of a NSO, it can be used to derive a kinetic theory for the relevant observables R_n . In this, we follow the

approach taken by Pokrovskii [101]. The equations are derived in appendix A, and are given by:

$$\begin{aligned} \langle \dot{R}_k \rangle &= i \sum_m c_{km} \langle R_m \rangle + i \langle [H_I, R_k] \rangle_{rel} \\ &\quad - \lim_{\epsilon \rightarrow 0} \int_{-\infty}^0 d\tau e^{\epsilon\tau} \left(\langle [H_I(\tau), [H_I, R_k]] \rangle_{rel} \right. \\ &\quad \left. + i \sum_{m\ell} \frac{\partial \langle [H_I, R_k] \rangle_{rel}}{\partial \langle R_m \rangle} \frac{\partial \langle R_m \rangle}{\partial \lambda_n} \frac{\partial \lambda_n}{\partial \langle R_\ell \rangle} \langle [H_I(\tau), R_\ell] \rangle_{rel} \right) + \mathcal{O}(H_I^3) \end{aligned}$$

The derived kinetic operator equation will be applied to the system already treated in section 2.2 using Redfield theory. We start from a Hamiltonian similar to that of eq. 2.14, but now explicitly incorporating the ensemble of many spins.

$$H = - \sum_i \omega_i S_i^z + \sum_k \omega_k a_k^\dagger a_k + \sum_{ik} (\bar{g}_k a_k S_i^+ + g_k a_k^\dagger S_i^-)$$

We assume that each spin S_i^z is part of an inhomogeneously broadened lineprofile. We calculate equations of motion for the expectation values of $\{S_i^z, S_i^-, S_i^+\}, \{a_k^\dagger a_k\}$. Many of the steps in the calculation will be conceptually similar to those taken in section 2.2. Note that we do not take into account the spatial diffusion of phonons, even while this was a crucial part of the experiments. An attempt to do this was made by Solov'ev.[102]

Longitudinal Spin Equation

Starting with S_i^z we obtain:

$$[H_0, S_i^z] = 0, [H_I, S_i^z] = \sum_k (\bar{g}_k a_k S_i^+ - g_k a_k^\dagger S_i^-)$$

For the double commutator, we drop double phonon and phonon mixing terms $a_k^2, a_k^\dagger a_\ell$, etc. Analogous to the argument of section 2.2, we assume that once the expectation value with respect to ρ_{rel} is taken, all these terms will disappear, since ρ_{rel} will be diagonal in the phonon Fock basis. Moreover, we will also drop spin mixing and quadratic terms $(S_i^-)^2, S_i^+ S_j^-$ etc., because their time correlations are assumed to be non-secular. Concluding:

$$\begin{aligned} \langle [H_I(\tau), [H_I, S_i^z]] \rangle_{rel} &\sim \langle \sum_k |g_k|^2 (a_k^\dagger a_k(\tau) S_i^- S_i^+(\tau) - a_k(\tau) a_k^\dagger S_i^+(\tau) S_i^- \\ &\quad + a_k^\dagger(\tau) a_k S_i^-(\tau) S_i^+ - a_k a_k^\dagger(\tau) S_i^+ S_i^-(\tau)) \rangle_{rel} \end{aligned}$$

Due to the occurrence of individual terms a_k , also $\langle [H_I, S_i^z] \rangle_{rel} = 0$, and therefore we can also ignore the other second order term proportional to $\frac{\partial}{\partial \langle R_m \rangle} \langle [H_I, S_i^z] \rangle_{rel}$.

To obtain equations that are actually useful, some assumptions on the explicit form of the correlation functions must be made. First of all, it is assumed that in leading order the spins and phonons are uncorrelated, for example:

$$\langle a_k^\dagger(\tau) a_k S_i^-(\tau) S_i^+ \rangle_{rel} \approx \langle a_k^\dagger(\tau) a_k \rangle_{rel} \langle S_i^-(\tau) S_i^+ \rangle_{rel}$$

We take

$$\langle S_i^+(\tau) S_i^- \rangle_{rel} = f(\tau) e^{i\omega_i \tau} \langle S_i^+ S_i^- \rangle_{rel}$$

where $f(\tau)$ is related to the normalised homogeneous linewidth $f(\omega - \omega_i)$ by the Fourier transform, as is stated by the Wiener-Khinchin theorem. For the phonons we simply take their correlation to be that of free particles:

$$\langle a_k^\dagger(\tau) a_k \rangle_{rel} = e^{i\omega_k \tau} \langle a_k^\dagger a_k \rangle_{rel}$$

Using these relations, $\langle a_k^\dagger a_k \rangle_{rel} = n_k$, $\langle S_i^+ S_i^- \rangle_{rel} = \frac{1}{2} - \langle S_i^z \rangle_{rel} = \frac{1}{2} - \langle S_i^z \rangle$, and also the standard commutations/anticommutations, the double commutator can be simplified to:

$$\langle [H_I(\tau), [H_I, S_i^z]] \rangle_{rel} = 2 \sum_k |g_k|^2 f(\tau) \cos((\omega_k - \omega_i)\tau) \left((2n_k + 1) \langle S_i^z \rangle - \frac{1}{2} \right)$$

The τ dependence enters the equation for $\langle \dot{S}_i^z \rangle_{rel}$ as:

$$\lim_{\epsilon \rightarrow 0} \int_{-\infty}^0 d\tau e^{\epsilon \tau} f(\tau) \cos((\omega_k - \omega_i)\tau)$$

Assuming now that $f(\omega - \omega_i)$ is a Cauchy-Lorentz distribution with linewidth Γ , then $f(\tau) = e^{-\Gamma|\tau|}$. This integral can then be rewritten as Fourier cosine transform:

$$\begin{aligned} \lim_{\epsilon \rightarrow 0} \int_0^\infty d\tau e^{-(\epsilon + \Gamma)\tau} \cos((\omega_k - \omega_i)\tau) &= \mathcal{F}_c[e^{-(\epsilon + \Gamma)\tau}] \\ &= \lim_{\epsilon \rightarrow 0} \frac{(\Gamma + \epsilon)/\pi}{(\omega_k - \omega_i)^2 + (\Gamma + \epsilon)^2} = \frac{\Gamma/\pi}{(\omega_k - \omega_i)^2 + \Gamma^2} \end{aligned}$$

We also reparametrise $z_k = \frac{n_k - n_k^0}{n_k^0 + \frac{1}{2}}$, where n_k^0 is the phonon thermal equilibrium distribution. Compare Faughan and Strandberg [66]. In that case:

$$(2n_k + 1) \langle S_i^z \rangle - \frac{1}{2} = (2n_k^0 + 1) \left((z_k + 1) \langle S_i^z \rangle - \frac{1/2}{n_0 + \frac{1}{2}} \right) \\ \stackrel{\text{def}}{=} (2n_k^0 + 1) \left((z_k + 1) \langle S_i^z \rangle - \langle S_i^z \rangle_{eq} \right)$$

We obtain:

$$\frac{d}{dt} \langle S_i^z \rangle = -2 \sum_k |g_k|^2 f(\omega_k - \omega_i) (2n_k^0 + 1) \left((z_k + 1) \langle S_i^z \rangle - \langle S_i^z \rangle_{eq} \right)$$

The continuum limit is taken, and it is assumed that the spectral density and phonon distribution, vary much slower in the Fourier domain than the linewidth, such that we can rewrite:

$$\sum_k |g_{k_0}|^2 (2n_{k_0}^0 + 1) f(\omega_k - \omega_0) \longrightarrow \int J(\omega) (2n_\omega^0 + 1) f(\omega - \omega_i) \\ \approx J(\omega_0) (2n_{\omega_0}^0 + 1) \int d\omega f(\omega - \omega_i)$$

$$\frac{d}{dt} \langle S_i^z \rangle = -\frac{1}{T_1} \int d\omega f(\omega - \omega_i) \left((z_\omega + 1) \langle S_i^z \rangle - \langle S_i^z \rangle_{eq} \right)$$

Here we identified the expression for T_1 we found in section 2.2.

Transverse Spin and Phonon Equations

The derivation of the transverse spin and phonon equation of motions proceed in a similar manner. They are calculated explicitly for only one member of the Hermitian conjugated pair $S_i^- = (S_i^+)^\dagger$.

$$[H_0, S_i^-] = -\omega_i S_i^-, [H_I, S_i^-] = -\sum_k \bar{g}_k a_k S_i^z \\ [H_0, a_k^\dagger a_k] = 0, [H_I, a_k^\dagger a_k] = \sum_i \bar{g}_k a_k S_i^+ - g_k a_k^\dagger S_i^-$$

As before the expectation values of the single commutators are zero. For the spin double commutators we obtain, under the same assumptions as above:

$$\langle [H_I(\tau), [H_I, S_i^-]] \rangle_{rel} \\ = -\sum_k |g_k| e^{i\omega_k \tau} \left(n_k \langle S_i^z S_i^- \rangle_{rel}(\tau) - \langle S_i^- \rangle_{rel}(\tau) \langle S_i^z \rangle_{rel}(\tau) \right) + \frac{1}{2} \langle S_i^z S_i^- \rangle_{rel}(\tau)$$

For the correlation functions the following estimation is made:

$$\begin{aligned} & \langle S_i^z S_i^-(\tau) \rangle_{rel} \\ = & \frac{1}{2} \langle (S_i^- S_i^+ - S_i^+ S_i^-) S_i^-(\tau) \rangle_{rel} \approx \frac{1}{2} \langle S_i^- \rangle \langle S_i^+ S_i^-(\tau) \rangle_{rel} = \frac{1}{2} f(\tau) e^{-i\omega_i \tau} \langle S_i^- \rangle \end{aligned}$$

Which implies:

$$\langle [H_I(\tau), [H_I, S_i^-]] \rangle_{rel} = - \sum_k |g_k| e^{i(\omega_k - \omega_i)\tau} (2n_k^0 + 1) (z_k + 1) \langle S_i^- \rangle$$

Such that we obtain in the continuous limit:

$$\frac{d}{dt} \langle S_i^- \rangle = i\omega_i \langle S_i^- \rangle - \frac{1}{2T_1} \int d\omega f(\omega - \omega_i) (z_\omega + 1) \langle S_i^- \rangle$$

The double commutator on the phonon number operator gives:

$$\begin{aligned} & \lim_{\epsilon \rightarrow 0} \int_{-\infty}^0 d\tau e^{\epsilon\tau} \langle [H_I(\tau), [H_I, a_k^\dagger a_k]] \rangle_{rel} \\ = & -2 \sum_i |g_k|^2 f(\omega_k - \omega_i) (2n_k^0 + 1) ((z_k + 1) \langle S_i^z \rangle - \langle S_i^z \rangle_{eq}) \end{aligned}$$

We now desire the continuum limit for the spins as well. In that case, we approximate:

$$\sum_i \longrightarrow N \int d\tilde{\omega} g(\tilde{\omega} - \omega_0)$$

Here N is the total number of spins, and $g(\tilde{\omega} - \omega_0)$ is the normalised inhomogeneous lineshape centered around ω_0 . We now define a Bottleneck factor, that models the ratio of inflow to the outflow of energy into the phonon bath, given by:

$$b(\omega) = \frac{Ng(\omega - \omega_0)}{J(\omega_0)}$$

Using:

$$\frac{dn_k}{dt} = (n_k^0 + \frac{1}{2}) \frac{dz_k}{dt}$$

We obtain

$$\frac{dz_\omega}{dt} = \frac{1}{T_1} \int d\tilde{\omega} b(\tilde{\omega}) f(\omega - \tilde{\omega}) ((z_\omega + 1) \langle S_i^z \rangle - \langle S_i^z \rangle_{eq})$$

System of Equations

We found the evolution of the spin ensemble and resonant phonon bath under influence of H_I . Now more terms will be added *ad hoc* to these equations to make them more realistic. This can be seen as an educated guess of what the effect of a more realistic interaction Hamiltonian would be.

- First of all, to the equation for $\langle S_{\tilde{\omega}}^- \rangle$ we add a term that reflects the transverse relaxation by spin-spin interactions. It is defined by a timescale T_φ
- To the equation for z_ω we add a term that reflects the relaxation of the phonons through the thermal contact. Defined by a timescale T_{ph}
- We add driving terms to equations for $\langle S_{\tilde{\omega}}^z \rangle$ and $\langle S_{\tilde{\omega}}^- \rangle$. What they should be can be read-off directly from the Bloch equations 2.1, or alternatively can be calculated by taking:

$$H_0 \mapsto H_0 + 2\gamma B_{mw} \cos(\Omega t) \sum_i f(\Omega - \omega_i) S_i^x$$

The additional factor $f(\Omega - \omega_i)$ is added to ensure that only spins within the homogeneous linewidth subject to the driving respond to it. This approach was also taken by for example by Grinberg [103] and Al'tshuler [104].

The system of equations becomes:

$$\begin{aligned} \frac{d}{dt} \langle S_{\tilde{\omega}}^z \rangle &= -\frac{1}{T_1} \int d\omega f(\omega - \tilde{\omega}) ((z_\omega + 1) \langle S_{\tilde{\omega}}^z \rangle - \langle S_{\tilde{\omega}}^z \rangle_{eq}) \\ &\quad - 2\gamma B_{mw} \cos(\Omega t) f(\Omega - \tilde{\omega}) \Re[\langle S_{\tilde{\omega}}^- \rangle] \\ \frac{d}{dt} \langle S_{\tilde{\omega}}^- \rangle &= -i\tilde{\omega} \langle S_{\tilde{\omega}}^- \rangle - \frac{1}{2T_1} \int d\omega f(\omega - \tilde{\omega}) (z_\omega + 1) \langle S_{\tilde{\omega}}^- \rangle \\ &\quad - \frac{1}{T_\varphi} \langle S_{\tilde{\omega}}^- \rangle + 2i\gamma B_{mw} \cos(\Omega t) f(\Omega - \tilde{\omega}) \langle S_{\tilde{\omega}}^z \rangle \\ \frac{d}{dt} z_\omega &= \frac{1}{T_1} \int d\tilde{\omega} b(\tilde{\omega}) f(\omega - \tilde{\omega}) ((z_\omega + 1) \langle S_{\tilde{\omega}}^z \rangle - \langle S_{\tilde{\omega}}^z \rangle_{eq}) - \frac{z_\omega}{T_{ph}} \end{aligned}$$

Analogous to section 2.1, we perform simulations of both the steady-state and transient response of the magnetisation.

To make the analysis of the steady response simpler, we transform the spin operators to a rotating frame, with a unitary transformation generated by

$U = \otimes_{\omega} U_{\omega} = \otimes_{\tilde{\omega}} U_{\tilde{\omega}} = \otimes_{\tilde{\omega}} \exp i\Omega S_{\tilde{\omega}}^z$. In that case:

$$\begin{aligned} S_{\tilde{\omega}}^z &\mapsto \tilde{S}_{\tilde{\omega}}^z = U_{\tilde{\omega}}^{\dagger} S_{\tilde{\omega}}^z U_{\tilde{\omega}} = S_{\tilde{\omega}}^z \\ S_{\tilde{\omega}}^{-} &\mapsto \tilde{S}_{\tilde{\omega}}^{-} = U_{\tilde{\omega}}^{\dagger} S^{-} U_{\tilde{\omega}} = e^{-i\Omega t} S_{\tilde{\omega}}^{-} \end{aligned}$$

Using that $S_{\tilde{\omega}}^{-} = S_{\tilde{\omega}}^x + iS_{\tilde{\omega}}^y$, the driving term in the $\langle S_{\tilde{\omega}}^z \rangle$ equation can be rewritten in the secular approximation as:

$$\gamma B_{mw} \cos(\Omega t) \Re[\langle \tilde{S}_{\tilde{\omega}}^{-} \rangle] = \gamma B_{mw} \Re[\cos(\Omega t) e^{-i\Omega t} \langle S_{\tilde{\omega}}^{-} \rangle] \approx \gamma B_{mw} \langle S_{\tilde{\omega}}^x \rangle$$

While the $\langle \tilde{S}^{-} \rangle$ equation becomes:

$$\begin{aligned} \frac{d}{dt} \langle \tilde{S}_{\tilde{\omega}}^{-} \rangle &= \frac{d}{dt} \langle e^{-i\Omega t} S_{\tilde{\omega}}^{-} \rangle = e^{i\Omega t} \frac{d}{dt} \langle S_{\tilde{\omega}}^{-} \rangle + i\Omega e^{i\Omega t} \langle S_{\tilde{\omega}}^{-} \rangle \\ &= i\tilde{\omega} \langle S_{\tilde{\omega}}^{-} \rangle + \dots + 2i\gamma B_{mw} f(\Omega - \tilde{\omega}) \cos \Omega t \langle S_{\tilde{\omega}}^z \rangle \\ \implies \frac{d}{dt} \langle S_{\tilde{\omega}}^{-} \rangle &\approx i(\tilde{\omega} - \Omega) \langle S^{-} \rangle + \dots + i\gamma B_{mw} f(\Omega - \tilde{\omega}) \langle S^z \rangle \end{aligned}$$

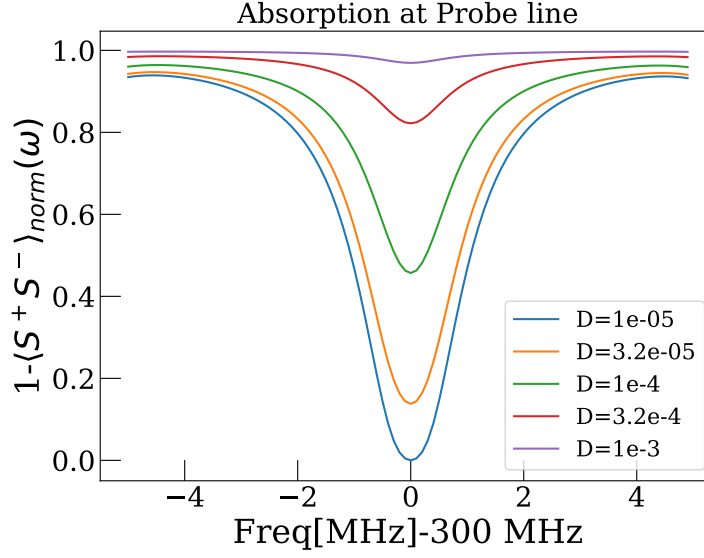
Decomposing the spin quadrature operators back into x and y operators, one obtains the following simplified system in the rotating frame:

$$\begin{aligned} \frac{d}{dt} \langle S_{\tilde{\omega}}^z \rangle &= -\frac{1}{T_1} \int d\omega f(\omega - \tilde{\omega}) ((z_{\omega} + 1) \langle S_{\tilde{\omega}}^z \rangle - \langle S_{\tilde{\omega}}^z \rangle_{eq}) \\ &\quad - \gamma B_{mw} f(\Omega - \tilde{\omega}) \Re[\langle S_{\tilde{\omega}}^{-} \rangle] \\ \frac{d}{dt} \langle S_{\tilde{\omega}}^{-} \rangle &= i(\tilde{\omega} - \Omega) \langle S_{\tilde{\omega}}^{-} \rangle - \frac{1}{2T_1} \int d\omega f(\omega - \tilde{\omega}) (z_{\omega} + 1) \langle S_{\tilde{\omega}}^{-} \rangle \\ &\quad - \frac{1}{T_{\phi}} \langle S_{\tilde{\omega}}^{-} \rangle + i\gamma B_{mw} f(\Omega - \tilde{\omega}) \langle S_{\tilde{\omega}}^z \rangle \\ \frac{d}{dt} z_{\omega} &= \frac{1}{T_1} \int d\tilde{\omega} b(\tilde{\omega}) f(\omega - \tilde{\omega}) ((z_{\omega} + 1) \langle S_{\tilde{\omega}}^z \rangle - \langle S_{\tilde{\omega}}^z \rangle_{eq}) - \frac{z_{\omega}}{T_{ph}} \end{aligned}$$

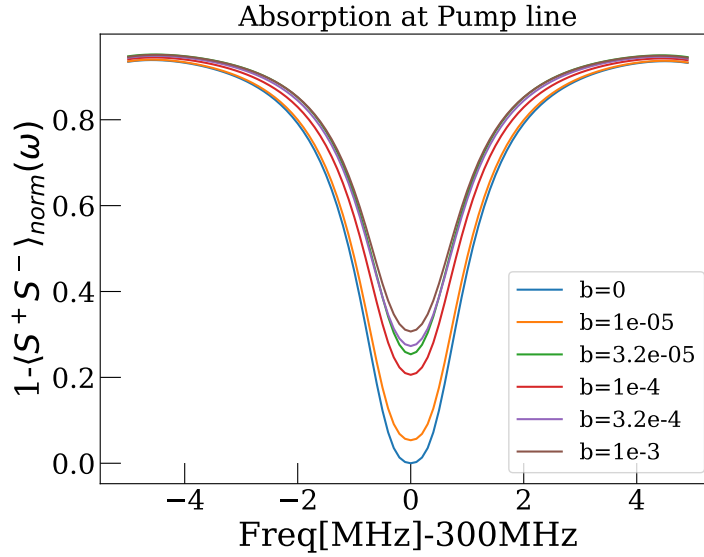
The rotating frame and lab frame equations were simulated. It must be noted beforehand that the chosen parameters were not the most realistic, but were motivated by making the simulations run fast and smoothly. Figures show steady-state results in the rotating frame 2.4 and 2.5, while figure 2.6 shows a transient response in the lab frame. The difference between figures 2.4a and 2.4b the simulations should reflect the situation at the probe and pump line respectively. With steady-state is meant that the simulations lasted until all parameters became stable under driving. The plotted spectra

are simply the latest values of a time domain simulation. For the pump simulation, the rotating frame equations were used as they are, but for the probe line b was set to zero, and instead a phonon source term $Dh(\omega)$ was added to the equation of motion for z_ω . Here the distribution $h(\omega)$ was the phonon distribution obtained from the pump simulations for $b = 10^{-4}$. The point of this source term was to see the effect on the lineshape $\langle S^+ S^- \rangle(\omega)$ when a steady stream of phonons was being generated by an external source. In both simulations, the lineshape showed saturation effects due to the presence of a non-equilibrium distribution of phonons. The CW spectroscopy measurements can be considered in the light of these simulations to get an indication on the accuracy of this model. Unfortunately, time limitations prevented more extensive exploration of simulations.

Figure 2.6 shows the relaxation of $\langle S_{\omega_0}^x \rangle$ for different combinations of T_{ph} and b . The first thing it is trying to convey is that the phonon bottleneck might cause decoherence. Secondly, it seems that if T_{ph} is short enough, the bottleneck factor b does not affect the spin relaxation at all.



(a) $\langle S^+ S^- \rangle (\omega)$ normalised w.r.t to the $D = 0$ result. For each simulation $b = 0$.



(b) $\langle S^+ S^- \rangle (\omega)$ normalised w.r.t to the $b = 0$ result. For each simulation $D = 0$

Figure 2.4: Steady state response of $1 - \langle S^+ S^- \rangle (\omega)$, at several values of the bottleneck factor b resp. source term D . Other parameters where $\omega_0 = 300$ MHz, $T_1 = 1 \mu\text{s}$, $T_2 = 0.1 \mu\text{s}$, $T_{ph} = 10 \mu\text{s}$ inhomog. broadening with Gaussian linewidth $\sigma = 15$ MHz, homog. broadening with Lorentzian linewidth $\Gamma = 5$ MHz, $\gamma B_{mw} = 50$ MHz and $\Omega = \omega_0$

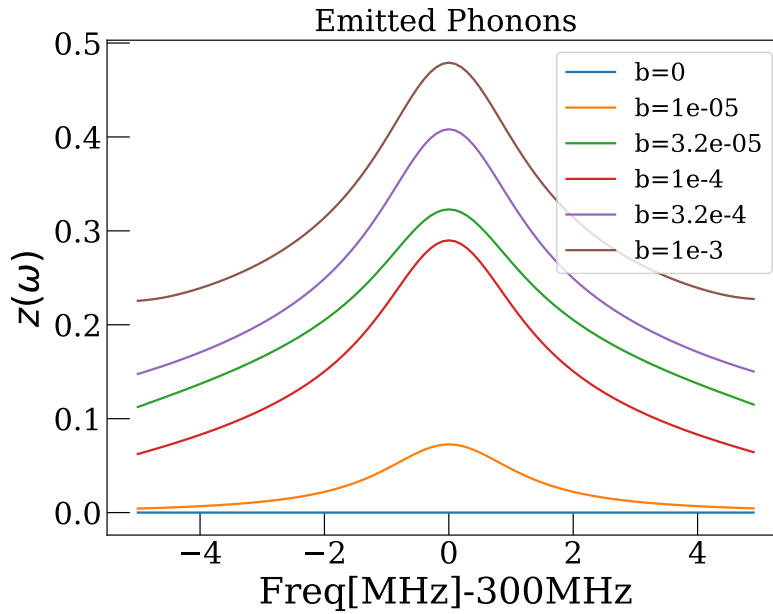


Figure 2.5: Spectrum of non-equilibrium phonons for different values of b , quantified by $z(\omega)$. The other simulation parameters were the same as that of figure 2.4a.

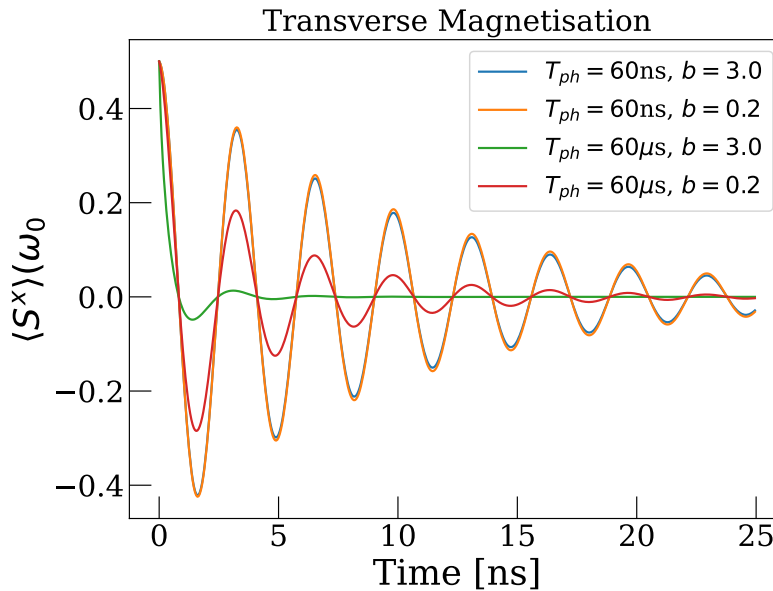


Figure 2.6: Transient response of the x -magnetisation for different values of phonon relaxation time T_{ph} and bottleneck factor b . Other parameters where $\omega_0 = 300$ MHz, $T_1 = 60$ ns, $T_2 = 10$ ns, inhomog. broadening with Gaussian linewidth $\sigma = 15$ MHz, homog. broadening with Lorentzian linewidth $\Gamma = 5$ MHz, $\gamma B_{mw} = 0$.

Experiment

3.1 Measurement Device

As was mentioned in the introduction, the experimental part of the thesis work was the fabrication of superconducting coplanar waveguides. Subsequently, these circuits were used to perform cryogenic measurements on spin ensembles in $^{167}\text{-Er:Y}_2\text{SiO}_5$. The designed chip layout consisted of two spatially separated waveguides, with the goal of studying the thermal transfer of energy between the spin ensembles coupled at each respective line.

3.1.1 Design of Coplanar Waveguides

The measurements were done using a device based on the chip design shown in figure 3.1. The basic idea behind the design is as follows. The chip consists of a $12\times 12\text{mm}$ silicon substrate of approximately 0.5 mm thickness, covered by a thin film of the type II superconductor niobium ($T_c = 18.3\text{K}$), of thickness 150 nm . The superconducting film is patterned into a coplanar waveguide. The fabrication procedure used to achieve this is treated in the next section. In figure 3.1 there are two patterned CPWs. They consist of a meandering CPW line, and at each end a wider section, that serves as bonding pad. From the bonding pad, the chip is contacted to other circuitry using aluminum wirebonds.

The following aims motivated the chip design:

- The microwave transmission of each line should be as high as possible, while reflection and losses should be as small as possible. The latter aim is achieved by using superconductors for the chip metallisation and wirebonds. The former two by having the impedance of the CPW match that of all other microwave circuitry, which is 50Ω .
- A master student should be able to connect wirebonds to the bonding pad, for this reason, they were designed with spacious 0.5×0.5 mm wide bonding pads to allow for comfortable bonding.
- The filling factor of the ESR set-up should be appropriate for the aims of the experiment. The CPW signal line width partly determines the induced magnetic field intensity profile, which determines the filling factor. The shape of the meander naturally also influences the filling factor. See the PhD dissertation of Clauss for an extensive discussion. [105] In the end the choice was made based more on the positive experience with narrower lines of group members that have worked plenty with these devices, than on a calculation of sorts.
- There should be no direct electromagnetic coupling between the different folds of the CPW meanders. In addition, there should be no electromagnetic coupling between the different CPWs.
- The chips had to be fabricated in-house, which added additional constraints.

The 3D design and electromagnetic simulations were performed with the finite element simulator *CST Studio Suite* 2018 developed by Dassault Systèmes. This software calculates, *inter alia*, the impedance, transmission, reflection and electromagnetic field distributions in time, frequency, and space for custom 3D models. The 3D geometry is constructed from simple or user-defined shapes and curves, while specifying the electric parameters of the material that these shapes should represent. To perform a simulation a 'port' must be specified. The ports indicate the location where signals are sent in and measured on the model. They have a rectangular shape, which determines the cross-section across which signals are transmitted for measurement or driving. The superconducting niobium is simulated as perfect conductor. To obtain accurate simulation results the following things were taken especially into account:

- The resolution of the meshgrid must be sufficiently fine. The software comes with an 'adaptive meshing' option, which would mean that the

simulation is run several times, refining the mesh in areas where the field is dense after each run. This requires many simulation runs, however. An alternative is to change the meshing manually and judge by eye if the resolution will be sufficient. For CPW structures, in practice, this means that the signal line and gap have their own set of mesh cells, in other words, that gap, ground and signal line nowhere share a mesh cell. When adaptive meshing was initiated after applying this rule of thumb the consequent changes in the simulation results were marginal.

- The ports must be sufficiently large. As a rule of thumb: large enough that the field intensity orthogonal to the signal propagation direction fully decays within the area covered by the port. To estimate a lower bound on the size of the port in unshielded structures such as CPWs, one could do repeated simulations with increasing port sizes, until the simulation results become practically independent of the changing port size. In shielded structures, such as a COAX connection, the port simply must cover all of the shielded area.
- Choosing proper boundary conditions. The most realistic results have been obtained with open boundary conditions. While this is in fact unphysical because silicon chips are finite. More physical would be to simulate the surrounding vacuum in addition to the actual chip. This however resulted in unexpected resonances, that are not measured experimentally. Complementary to this is that none of the port boundaries should coincide with those of the model.

Considering the geometrical parameters in figure 2.2, the finalised values that the design process converged upon for the CPW line were:

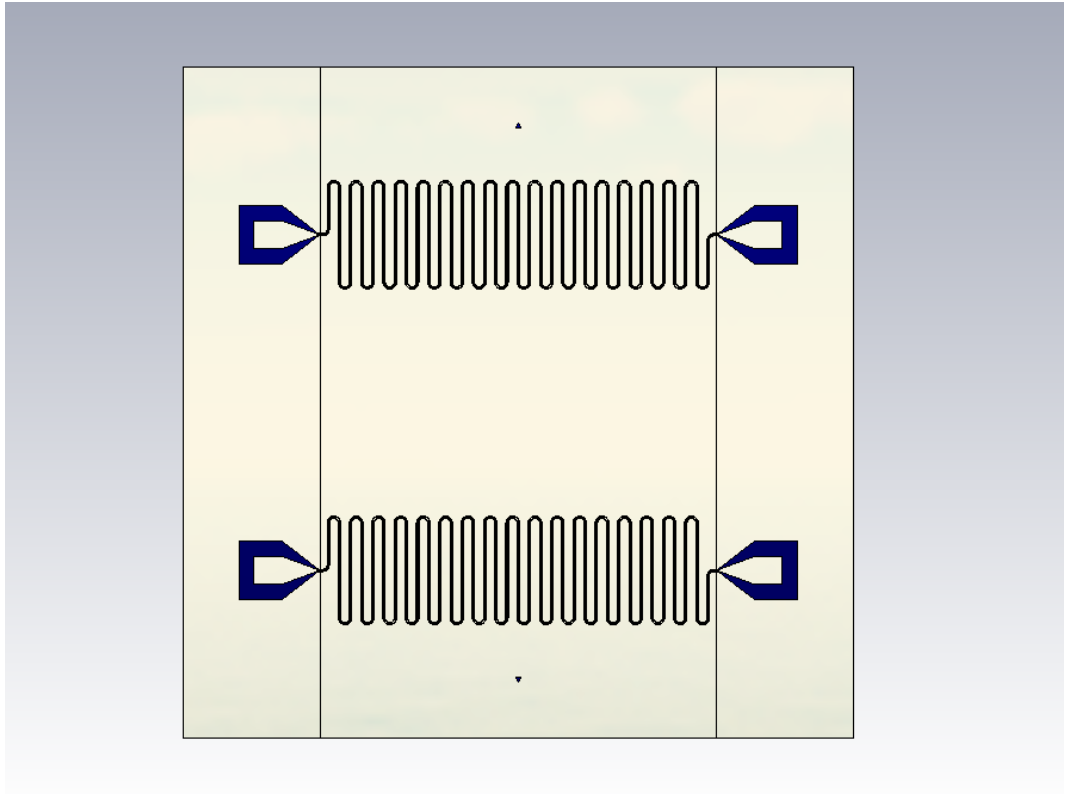
$$S = 20 \mu\text{m}$$

$$W = 12 \mu\text{m}$$

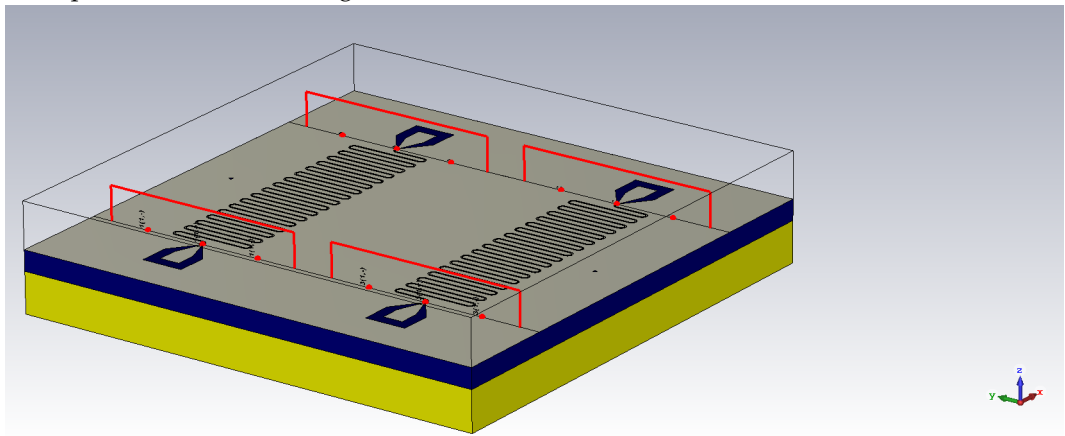
The central axes of the two lines were separated by 6 mm. The other relevant dimensions are shown in figure 3.1c. The scattering parameters of this design are shown in figure 3.2. The field distributions are shown in figures 3.3 and 3.4. From the field distributions, one can conclude that the microwave mode is indeed quasi-TEM and quasi-circular polarised. The tapers were individually simulated as well, and equally desirable results were obtained.

3.1.2 Microfabrication of Measurement Chips

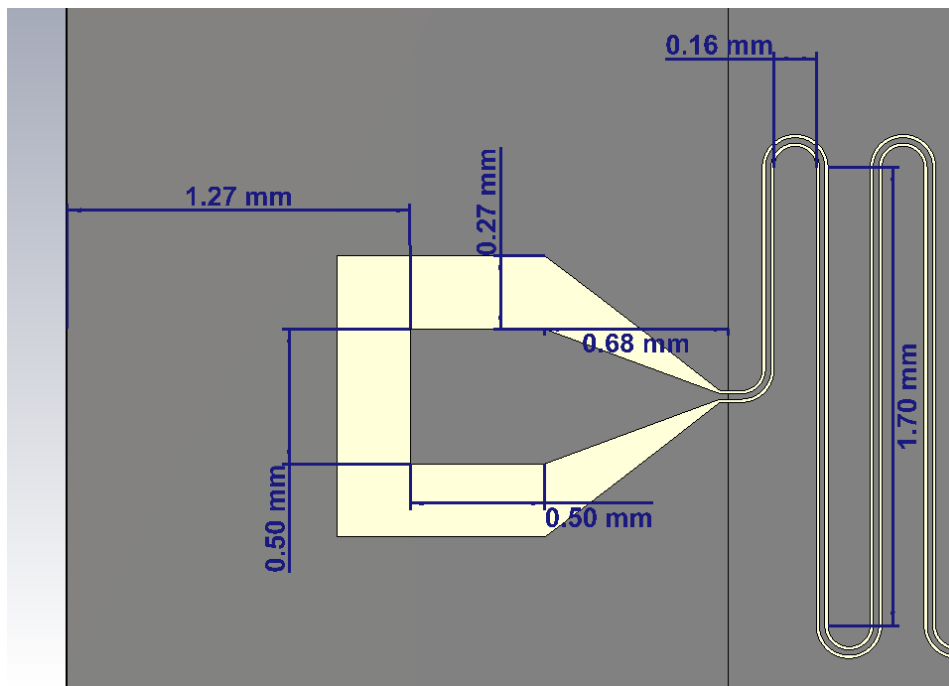
The entire fabrication process is schematically given in figure 3.5.



(a) Top view of the final design.



(b) Perspective view of the final design. Note that x is defined as the direction parallel to an imaginary line connecting the bonding pads of a single transmission line.



(c) Close-up of the taper, showing all relevant dimensions.

Figure 3.1: Finalised Chip Design in CST

The used substrates were cut from a silicon wafer into 12x12 mm chips, and had a shunting resistance of 2 k Ω ·cm. The first fabrication step always is the cleaning of the substrate. This is done in hot acetone in an ultrasonic bath, followed by a dip in isopropanol (IPA), because IPA leaves no marks when it evaporates.

Niobium Sputtering

Sputtering is a form of physical vapour deposition and is used to deposit the niobium thin film on the silicon substrate. This was done in the machine known as "Plassys". The procedure takes place in an ultra-high vacuum (UHV) chamber, pumped down by a turbo pump. The sample attached to a holder is installed with a load-lock. The solid niobium is in a sort of crucible, referred to as target. A precise atmosphere of argon ions is then inserted and maintained using a throttle valve. The target and another separate component form a cathode-anode system, and when a bias voltage is applied the Argon gas will partly ionize. The positively charged Argon ions then are accelerated towards the target, colliding with niobium atoms. A part of the niobium atoms will be released from the target and hit the substrate.

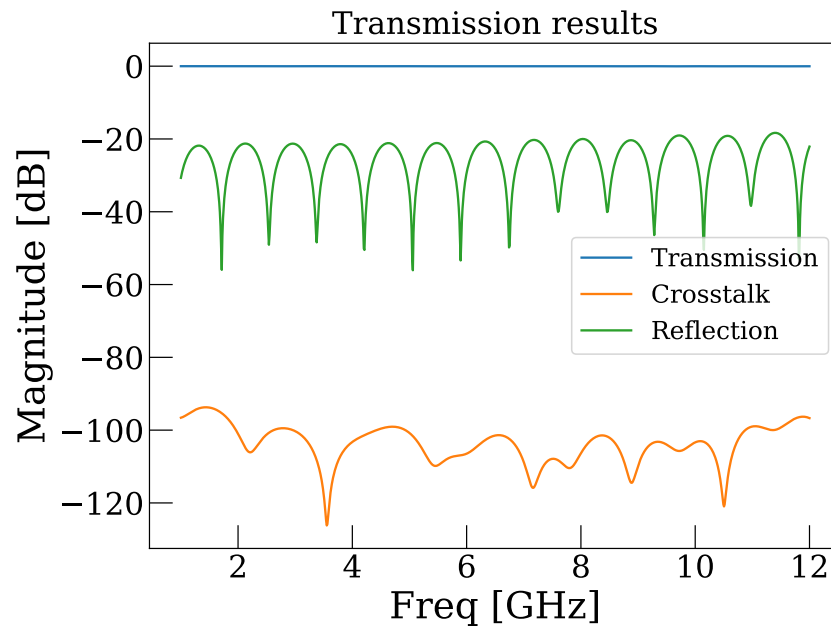


Figure 3.2: Results for the different scattering parameters. Because of symmetry not all are shown here. Transmission refers to input and output one at each end of the transmission line (S_{21} in case of a single transmission line). Reflection refers to reflection measured with single port at the end of a line (S_{11} in case of a single transmission line). For the crosstalk the input and output are diagonally opposite, both measuring at a different line.

The mechanical displacement of atoms in the substrate due to the collision will cause a niobium film to stick to the silicon.

Optical Lithography

After metallization, the CPWs must be patterned into the thin film. Patterning is done by a masked etch of the thin film. The mask is produced on the thin film by the lithography of a resist layer. The minimum feature size required for this process is given by the width of the gap between signal and ground in the CPW, being $12\ \mu\text{m}$ as mentioned in the previous section. This is still attainable using the resolution of optical lithography. This makes optical lithography preferable over electron beam lithography, because optical lithography is generally a faster process, and does not require the operation of a vacuum chamber.

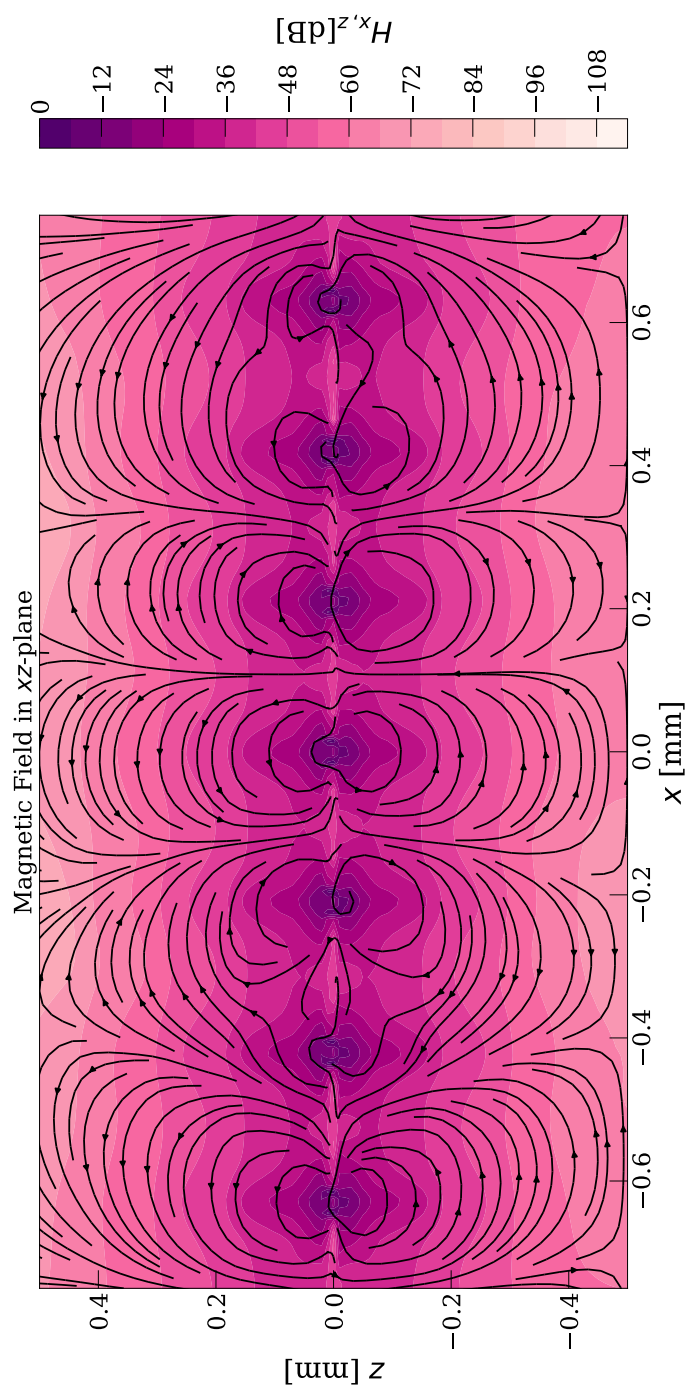


Figure 3.3: Field distribution along the central axis of the transmission line. Seven folds of the CPW meander can be seen. Intensity is normalised with respect to the maximum intensity. Data taken from CST simulation. Origin refers to centre of chip surface, with $z = 0$ the interface between silicon and niobium.

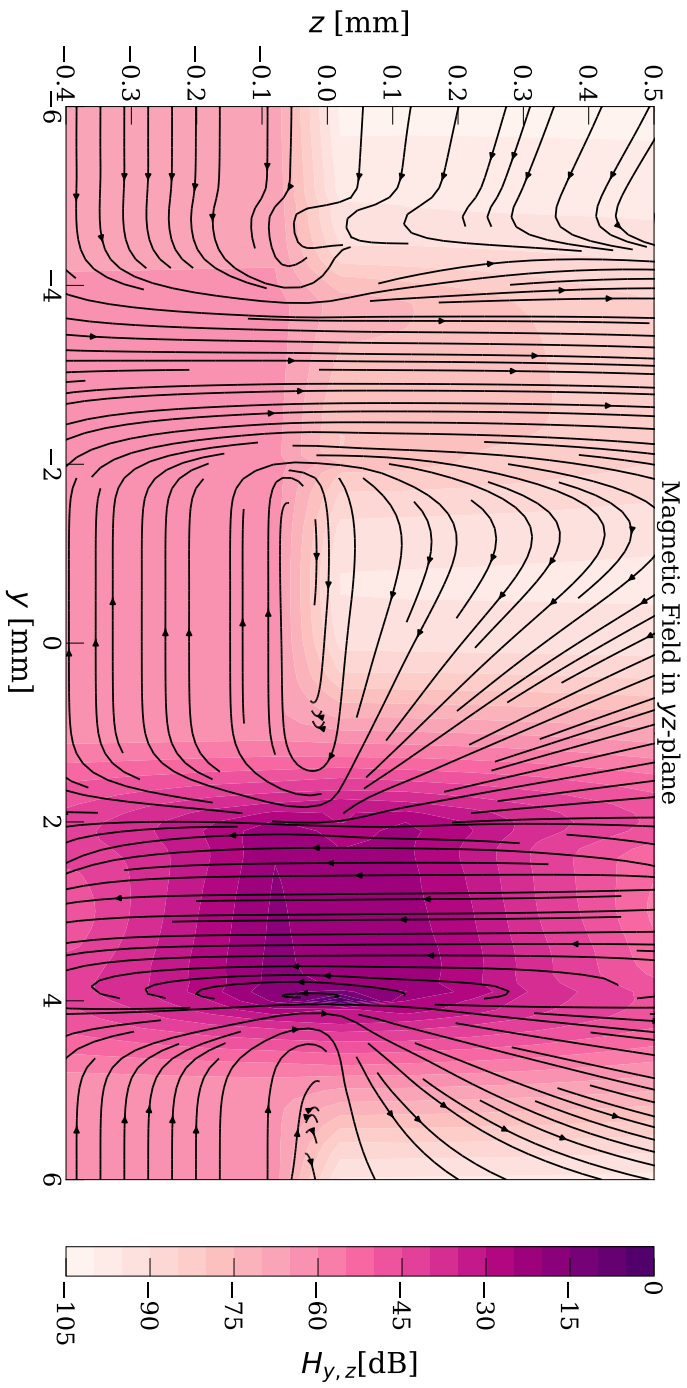


Figure 3.4: Field distribution along the y -axis, crossing both CPW structures along the microwave propagation direction. Intensity is normalised with respect to the maximum intensity. Data taken from CST simulation. Data taken from CST simulation. Origin refers to centre of chip surface, with $z = 0$ the interface between silicon and niobium.

In this process, the thin film is spincoated with a photoresist. The used photoresist AZ MiR 701 is a viscous reddish substance consisting of polymers and solvents, deposited to the thin film surface using a precision pipette. Immediately after deposition, the sample is spun on a rotating platform at several rpm.

The platform has a small hole, to which a tube connects to a pump. By pumping a low vacuum the sample is kept in place on the platform. The centrifugal force causes the resist to uniformly coat the sample surface, a process known as spin-coating or *Lackschleudigen*.

The sample is then baked on a hotplate, evaporating a part of the solvents, such that the resist solidifies into a thin film with a thickness on the order of 1 μm . The sample is then exposed in the laserwriter to a 405 nm laser, that writes the mask into the resist. The laserwriter consists of two laser units attached to a transfer stage, that moves the lasers over a platform. One laser is used for patterning, the other 650 nm laser is used to measure the focus and keep the set-up aligned. Analogous to the spin coater, the chip is kept in place on the platform by a low vacuum. At positions where the resist is exposed to the laser light, the polymers undergo a chemical reaction, changing the general solubility. This reaction happens within a certain spot size around the exposed point. This spot size limits the resolution of the lithography. In the used setup the minimal spot size was 300 nm. After exposure, the photoresist is baked again and consequently developed in a base solution, namely AZ726 MIF. The second baking step is to complete the photoreaction in the resist. The differential solubility induced by the laser exposure causes only the exposed pattern dissolves. This results in an etching mask on top of the thin niobium film.

Reactive Ion Etching

The mask allows for selective etching into the niobium. A dry etching process known as Reactive Ion Etching (RIE) was used. The RIE process takes place in a UHV chamber. A gas is released into the chamber, in the used Nb etch recipe this was pure SF_6 . The sample rests on a silicon wafer that is fixed to a platform. The platform is electrically disconnected from the chamber walls. An RF voltage is applied over the platform-chamber system. The RF ionises the gas. The resulting positively charged plasma and electron gas will both be inductively coupled to the RF potential. Because electrons have the smallest inertia, they tend to the chamber walls more than the plasma, turning the platform and chamber into an anode resp. cathode.

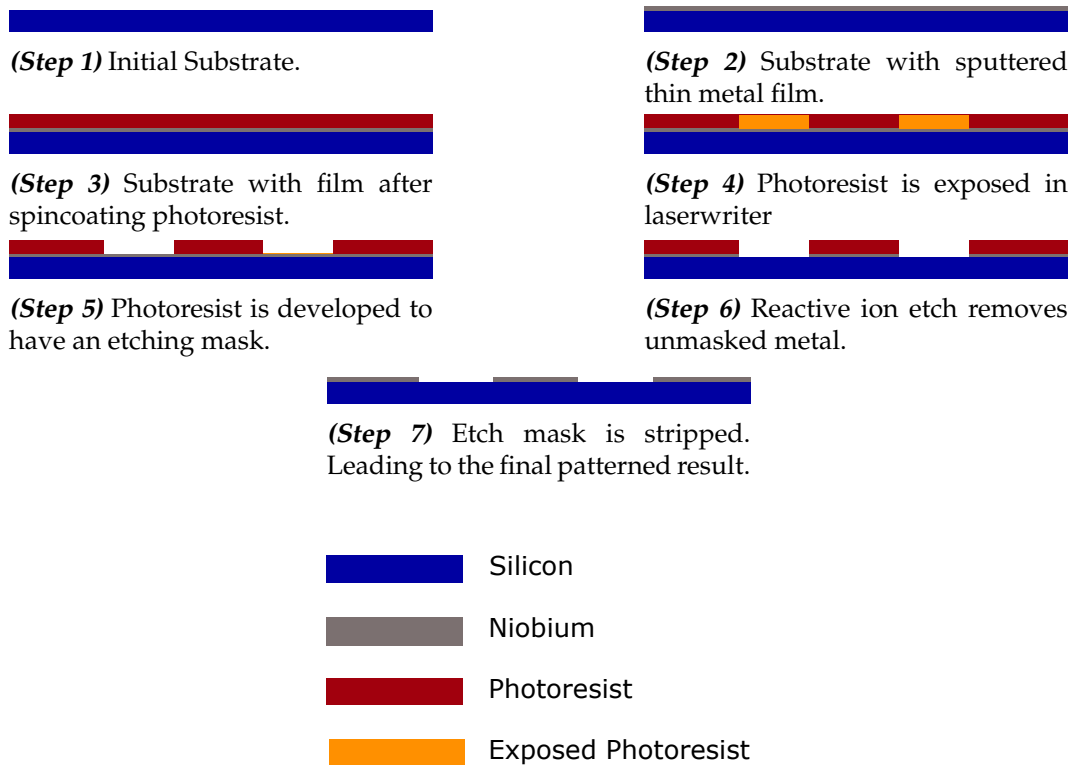
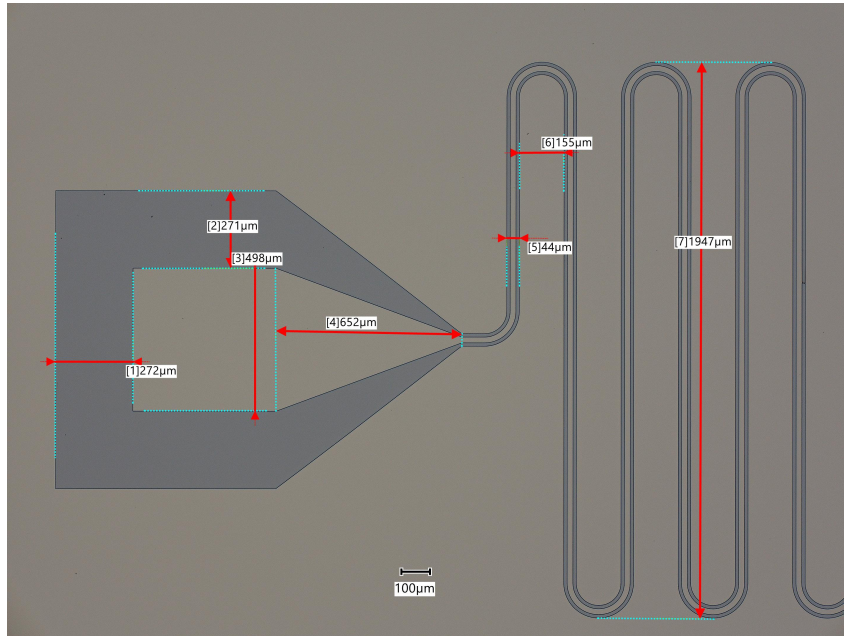


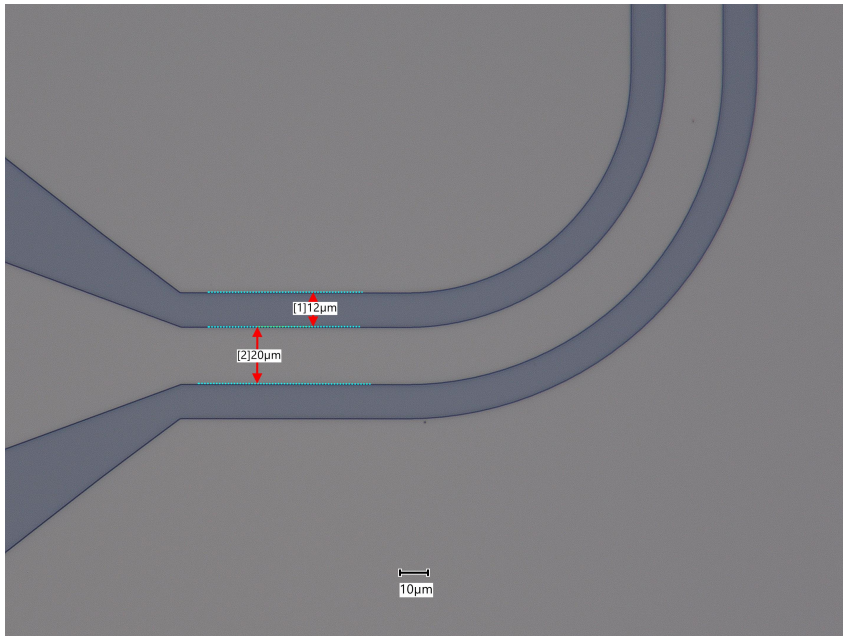
Figure 3.5: Diagram illustrating the fabrication process.

The plasma is accelerated onto the sample, where it chemically interacts with the niobium. At areas where resist was developed, the Niobium is etched away. RIE is a very rapid process, taking only a few minutes. Important is that the UHV chamber is very clean and that the etching procedure lasts long enough to fully etch through the exposed Nb film, exposing the Si substrate underneath. Important is that the vacuum of the RIE is very clean, for the process to be reliable.

Once the etch is complete, the remaining resist is stripped from the sample. This is done in another base solution, called Technistrip P1331. The sample is once more cleaned in hot acetone and hot IPA to remove any water that was not evaporated after the stripping procedure. In figure 3.6 microscope images of fabricated samples can be seen.



(a) Image of taper and line section with indicated dimensions. Compare to figure 3.1c.



(b) Image of the CPW itself, the gap was always the smallest feature size in the fabrication.



(c) Image of a short in the CPW. These type of defects were the most common for fabricated samples to turn out unusable. Most likely they were caused by bubbles or dirt in the photoresist.

Figure 3.6: Microscope colour pictures of fabrication samples.

3.1.3 Sample Packaging

Printed Circuit Boards

The on-chip superconducting circuit must be connected to microwave lines that link the sample in the dilution refrigerator to devices at room temperature. A copper plate was designed by the author and fabricated by the institute's fine mechanical department, with a central plateau to hold the chip. Around the plateau, the plate has enough space to hold printed circuit boards (PCBs). The PCBs were designed by the author and fabricated by the company Contag AG, based in Berlin.

The final design shown, in figure 3.7, was made using the open-source software KiCad, while electromagnetic simulations of these structures were performed in CST Studio Suite. The functional form is that of a simple CPW that leads from one edge of the board to the other. On one end the PCB is wirebonded to the superconducting circuit, on the other end it is contacted by an SMA connector. Two PCBs connect to 4 SMAs. The PCB consists of a Rogers RO4003C substrate of thickness 1.524 mm, covered on both surfaces by a 25 μm copper layer. The copper has a direct immersion gold (DIG)

coating. One of the two copper layers has the CPW patterned into it. Except for the appropriate layout, the following considerations went into the design:

- The conducting CPW must be matched to the standard impedance of 50Ω . This is done by choosing the correct CPW geometry. $S = 0.5\text{mm}$ and $W = 0.075\text{mm}$ was chosen.
- The layout demanded that the CPW makes a curve. The radius of this curve should not be on the order of $S + 2W$, but at least 2 to 3 times bigger. If this radius is too small it would cause reflections in the signal.
- The PCB surface should be suitable for wirebonding with aluminum. This is the case for DIG.
- Along the CPW vias (metallised through-holes) are fabricated for contact between the upper and lower grounds. For circuits in the low microwave regime, it is best to keep the distance between vias, and the distance from the vias to the CPW as small as possible.[107] The via radius should simply not be in resonance with wavelengths used for measurements.
- All of the materials that make up the PCBs must be non-magnetic. This is why DIG was chosen instead of a more commonly used electroless nickel immersion gold coating (ENIG).
- RO4003C maintains good dielectric properties at cryogenic temperatures and the in-plane thermal expansion coefficient is similar to that of copper and gold.

Sample Holder

As mentioned in the previous paragraph a copper plate was designed to hold the chip, PCBs, and SMA connectors. The mechanical design was performed in the software Autodesk Inventor. Besides having the correct layout, the only other non-trivial consideration was that screwholes generally should be through-holes, to allow for the air underneath the screw to escape when the dilution refrigerator is pumped to vacuum.

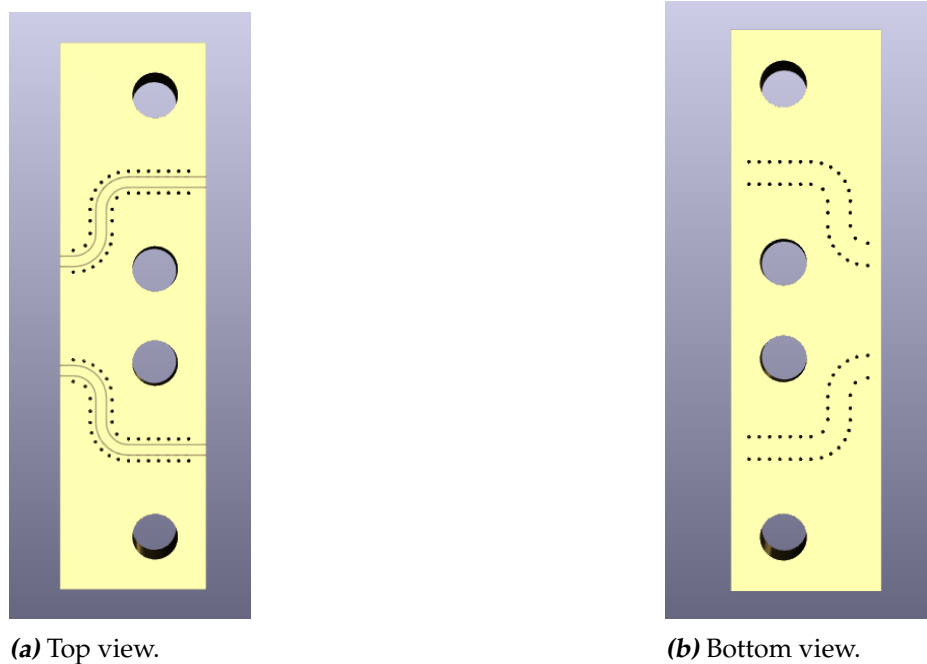


Figure 3.7: Layout of the designed PCBs. Images were extracted from the KICAD software. Visible are coplanar lines, vias, and screwholes for SMA connectors.

3.2 Measurements

3.2.1 Set-Up

Two of the fabricated chips were tested. All cryogenic spectroscopy measurements were performed with a Rohde Schwarz VNA, while room temperature measurements were performed with a Keysight VNA. Pump measurements additionally made use of an MGX signal generator. For the room temperature measurements the VNA was directly connected to the in- and outputs of the sample. The set-up for the cryogenic measurements is given in figure 3.8. Every sample was placed on the mixing chamber stage, and connected to both a lower and higher attenuated superconducting current line, to allow for a bigger difference in driving power between lines. Note that the incoming signal of the VNA is attenuated 20 dB more than that of the signal generator. The 10 dB room temperature attenuation was only used with the signal generator, and not when the VNA was connected to the low attenuation line. Several samples could be measured using a single output line connected to a switch. The switch is controlled by a custom-made electronics box. The output is then led through a circulator, that prevents high-temperature noise from propagating into the mixing chamber stage.

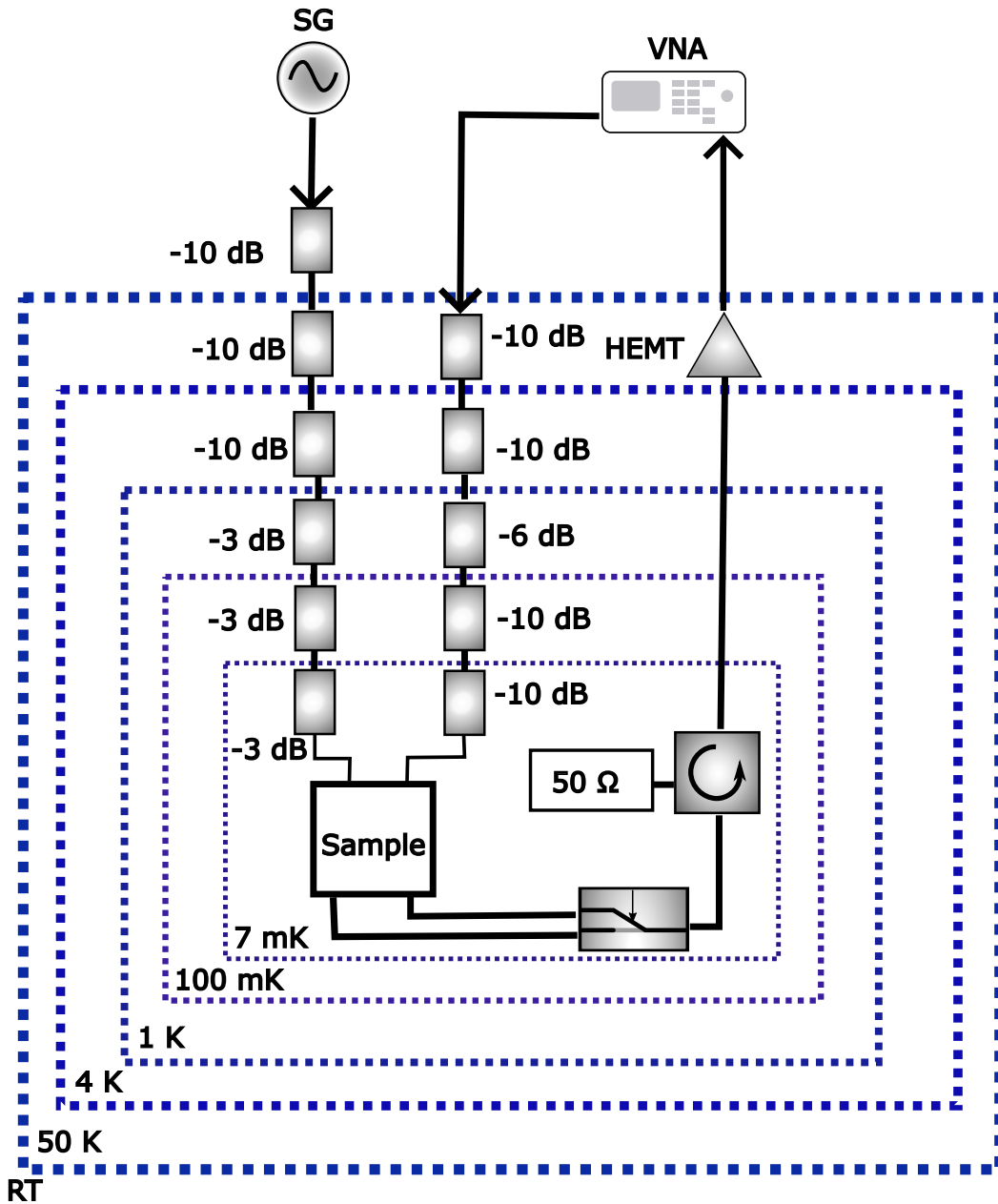


Figure 3.8: Diagram showing the measurement set-up in the dilution refrigerator. Indicated are the sample, attenuators, the HEMT amplifier, the signal switch (SW), a circulator, and the measuring equipment.

The output signals were amplified by a Low Noise Factory HEMT, with a documented amplification of roughly 20 dB at 5 K. For the room temperature measurements, no crystal was mounted. During cryogenic measurements, one of the chips hosted a crystal. It was mounted on top of the chip with a type of gum that can also be removable. The purpose of also measuring a second 'bare' chip was to obtain an indication of the reproducibility of the fabrication process.

3.2.2 Spectroscopy

The transmission parameter $S_{21}(\omega)$ of each line was measured at 7 millikelvin, as well as at room temperature. In the section below there will be referred many times to 'cold' or 7 millikelvin measurements, but one must note that 7 mK is the lowest temperature that the thermometer of the mixing chamber stage can register, so the temperature could also have been lower. Additionally, the switching process caused significant heating, but for the measurements presented below the temperature was never higher than 12 mK.

The room temperature results are given in figures 3.9. It is notable that both chips performed very poorly at room temperature. This was not unexpected, and it was also noticed by Clauss et al [20] that superconducting circuits that might perform very well when cooled down, are at ambient conditions mediocre compared to devices based on for example noble metals. At cryogenic temperature, the general transmission was significantly higher. The transmissions measured at 7 millikelvin can be seen in figure 3.10.

In addition to transmission, the crosstalk between lines was measured. What exactly is meant by this is that the VNA output was connected to the input of one of the transmission lines. The input of the VNA was then connected to the output of the other transmission line. The goal of this measurement was to give an estimate of the strength of the direct electromagnetic coupling between the two CPWs. The results for the two chips are given in figure 3.11.

We also present here the CW ESR spectroscopy results of four transitions, performed on the crystal mounted on the sample that was cooled down to 7 millikelvin. These four transitions were also probed for the study of thermal effects. The unprocessed power sweep data is given in figure 3.10. Considering that low attenuation lines have a flat background at -20 dB, that are attenuated by roughly -30 dB, while the HEMT amplifies maximally 20

dB. This means that the actual transmission can be estimated to be on the order of -10 dB.

Some global features can be seen in all four measured samples. Below 2.5 GHz the transmission starts to decrease significantly. From the power dependence, it is clear that the signal below this frequency is mostly noise. Additionally, there are many strong absorption dips above 5 GHz, the most prominent being at 6.5 GHz. This attenuation at both ends of the spectrum is simply the transmission profile of the circulator. The circulators used by the group were characterised before. The regime wherein the circulators should provide relatively flat transmission is also observed to have a much flatter transmission in the measurements. These results should be compared to figure 3.2, implying that the finite element simulations were generally accurate in predicting the transmission spectrum of the circuit.

To detect potential absorption by spins one must analyse the power dependence of the amplitude and phase of S_{21} , and look for saturation in features that look like an absorption profile. As is shown in simulations of figure 2.3, such a feature can take many shapes due to imperfections in the device. In addition, unresolved line pairs will also cause a distortion of the absorption profile. In figure 3.14 the transmission and group delay data of the relevant part of the spectrum is shown. From the transmission only it would be difficult to detect spin features, but this becomes easier if the phase or group delay is also considered, for which the power dependence is usually more significant. This can also be seen in figure 3.14a. For this work, the phase and group delay data was used to roughly locate the frequency of power-dependent features, after which transmission data was analysed to confirm the presence of saturation. Power-dependent features present also in the sample without crystal, could of course immediately be excluded from being spin resonances.

We consider in more detail four suspected spin resonances in the regime of 2 to 6 GHz. This is the regime where most of the ^{167}Er zero-field transitions should be found. The peaks are at approximately $f = 3.643$ GHz, 3.820 GHz, 4.730 GHz, and 4.891 GHz. The first two and last two we refer to as 'pairs' in the informal sense of the word. In figures 3.15a and 3.16a the transmission in the spectral regime concerning each pair is shown, together with Easyspin simulations of resonance frequencies. In figure ?? and figure 3.16 each resonance feature is shown in more detail, as well as the result after data processing. The method of data processing is described in detail in Appendix B. What the processed data shows is the power dependence of the linearised absorption amplitude with respect to the background absorption.

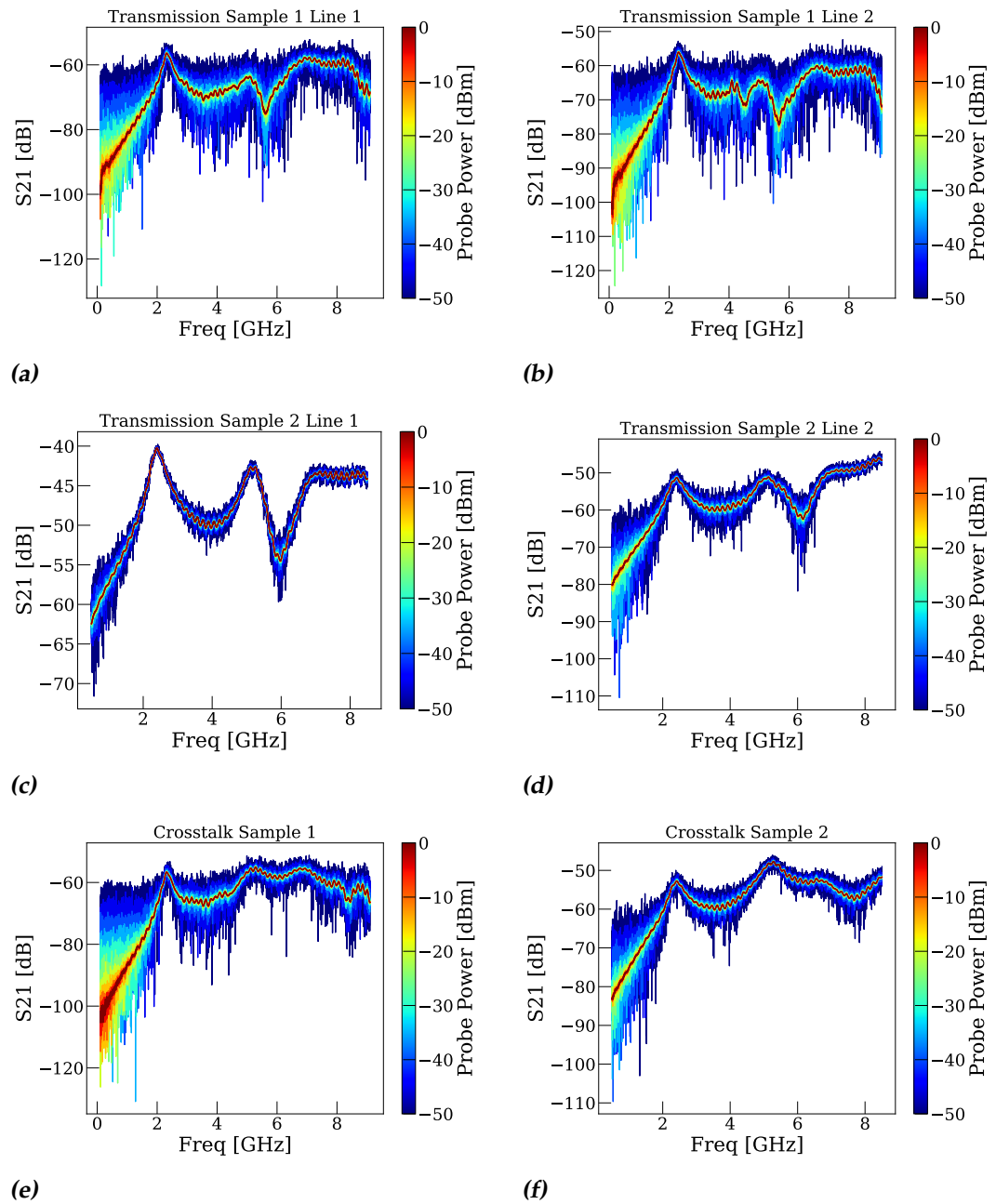


Figure 3.9: Unprocessed room temperature data of transmission (a-d) and crosstalk measurements (e,f).

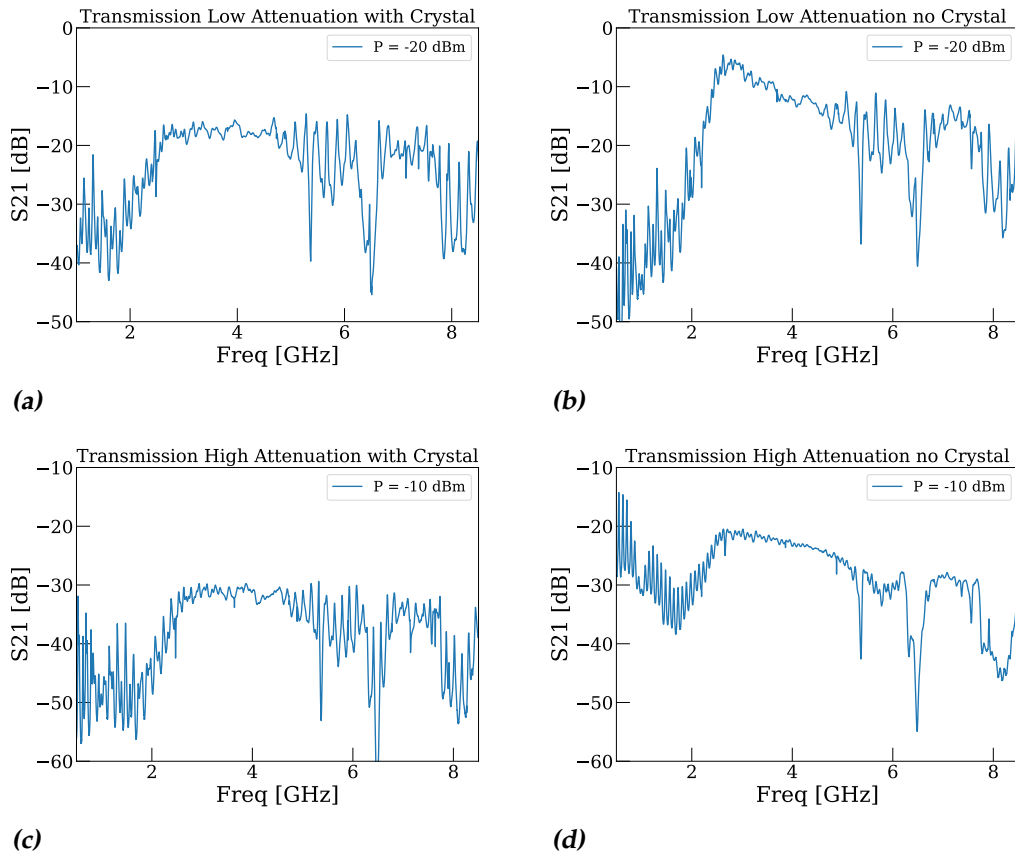


Figure 3.10: Cryogenic unprocessed transmission measurements data.

To obtain a better indication that these are actually spin resonances the data is compared with a zero-field Easyspin energy level and solid state spectrum simulations using data based on literature data [40], the latter being shown in figures 3.15a and 3.16a. The orientation of the used crystal is given in figure 3.12. This orientation is defined in terms of the optical extinction axes.[106] This orientation differed from the x, y, z orientation of the chip only by straight Euler angles, making conversions between the two frames straightforward.

As can be seen in figures 3.3 and 3.4, the longitudinal component of the field induced by the CPW is small compared to the other components. The CPW hosts a quasi-TEM circularly polarized mode. Considering the orientation of the crystal on the chip, see figure 3.13, the Easyspin simulations were performed with the field propagation direction along the b -axis.

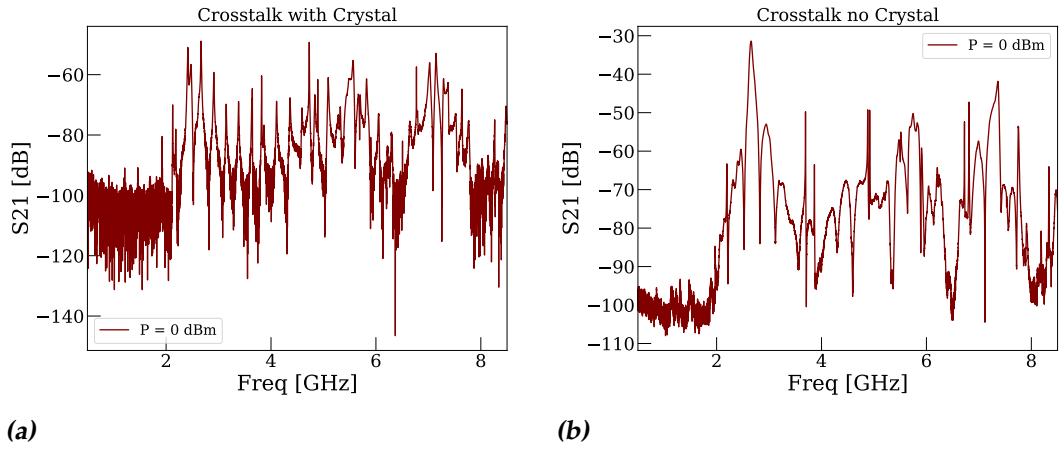


Figure 3.11: Cryogenic unprocessed crosstalk measurement data. Measured from high attenuation input to low attenuation output.

From the energy level simulations, we could identify to which state transfers the measured features most likely relate. The result is summarised in tables 3.1 and 3.2, using the convention $(m_S, m_I) \mapsto (m'_S, m'_I)$. For the pump-probe measurements presented below, we assumed these features were in fact spin resonance.

	3.643 GHz	3.820 GHz
Site 1	$(1/2, -5/2) \mapsto (-1/2, -7/2)$	$(1/2, 7/2) \mapsto (-1/2, 3/2)$
		$(1/2, 1/2) \mapsto (-1/2, -1/2)$
Site 2	-	-

Table 3.1: Potential transitions for features detected at 3.643 GHz and 3.820 GHz. For the latter, the signal might be a combination of two transitions.

	4.730 GHz	4.890 GHz
Site 1	$(1/2, 3/2) \mapsto (-1/2, -5/2)$	-
	$(1/2, 7/2) \mapsto (-1/2, -3/2)$	-
Site 2	-	$(1/2, 5/2 + 7/2) \mapsto (-1/2, -3/2)$

Table 3.2: Potential transitions for features detected at 4.730 GHz 4.890 GHz. For the former, the signal might be a combination of two transitions. For the latter the ground state is unresolved.

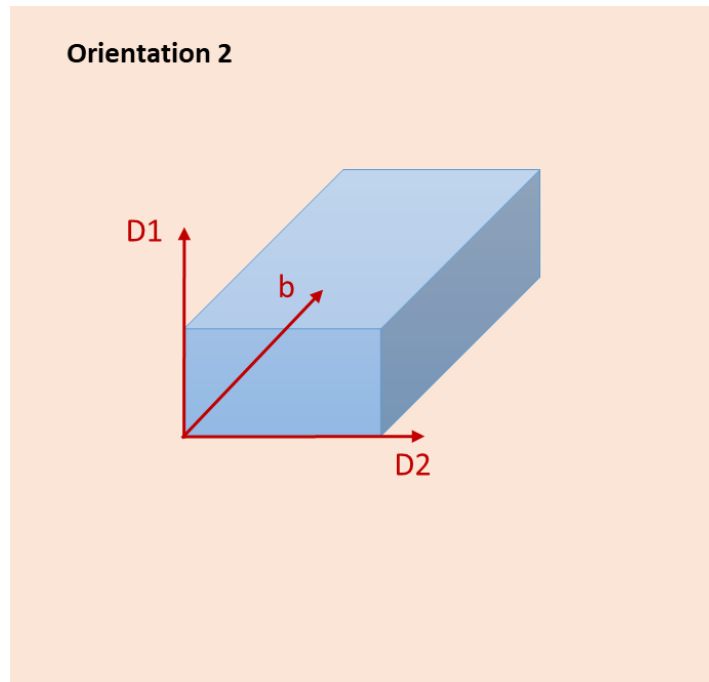


Figure 3.12: Orientation of the optical extinction axes in the used YSO crystal. During measurements the D_1 , D_2 , b axes corresponded with resp. the chip z , x , y axes.

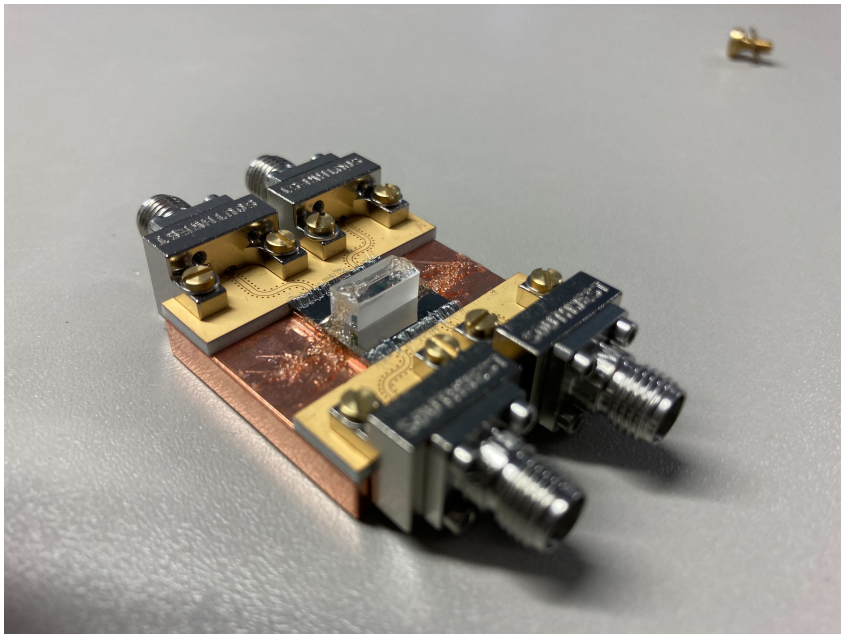


Figure 3.13: Colour photograph of the orientation of the crystal on the chip.

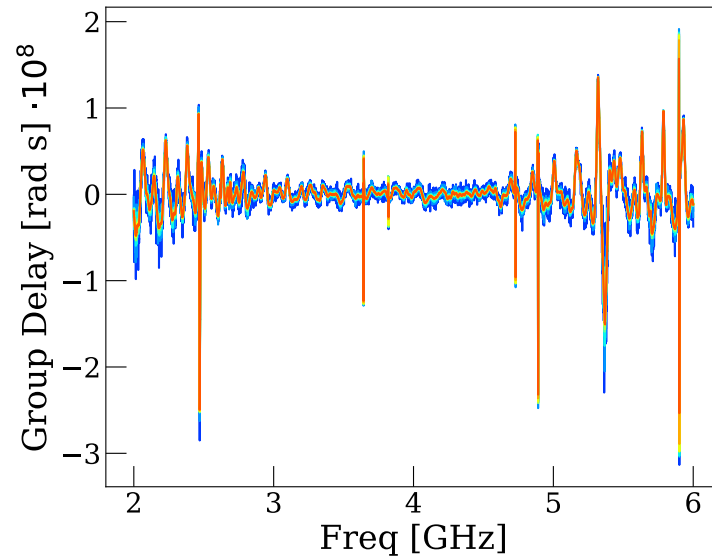
3.2.3 Pump-Probe

The rest of the presented measurements concern themselves with the effect of pumping on the second line, while CW spectroscopy is performed with the first (more attenuated) line. As shown in the previous section two pairs of transitions were studied, with the members of the pair separated by less than 1 GHz in the spectrum. The CW spectrum was using always the same VNA output power, while the power of the signal generator was varied. In this scheme, three such power sweeps were performed on each pair. Two of them with the pump frequency being close to the center of one of the two lineshapes. For the third measurement, the pump frequency was chosen to correspond to a section of the spectrum where no transitions were observed. We expect that the pumping leads to a steady state, where phonons are continuously emitted from the spins at the pumping line. In the presence of a phonon bottleneck, these phonons should survive long enough to reexcite other spins. By either continuous absorption-emission or direct diffusion the phonons will arrive at the spin ensemble coupled to the probe line. This is then expected to cause a measurable change in the steady state measured by the VNA. The non-resonant pumping serves as a null measurement. If the measured effect is indeed caused by a spin-phonon-spin energy transfer, this effect should disappear at non-resonant pumping.

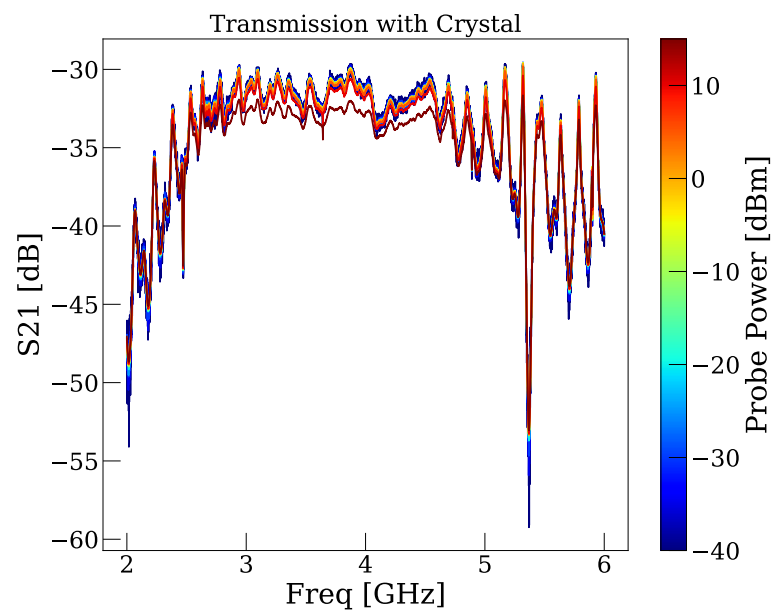
The VNA measurements were processed to derive the change in the linewidth of transition due to pumping. Additionally, if the pump was in resonance with the probe, the direct electromagnetic coupling between the pump and probe line would be visible in the spectrum as a very sharp peak, usually only slightly sharper than the frequency resolution of the measurement. It could always be detected and removed from the data easily. The fact that this occurs should be no surprise. The probing line will act as a pick-up coil for the pump signal, which can also be seen in figure 3.4. While the field strengths decay strongly over distance, it will still distort the VNA measurement if the probing power is low and the pumping power is high. Precise tests were done to see if this peak signal was correlated to any saturation. It was found that the peak occurred at whichever frequency was pumped, independent if it coincided with an absorption feature or not. If it did, then no additional saturation was detectable with respect to the broader saturation of the entire feature, even at 20 dBm pumping power, which was the highest power at which this was tested. Pumping powers used in actual measurements presented here never exceeded 10 dBm.

The details of peak removal and linewidth determination are explained in Appendix B. It must be said here that the latter was not a trivial procedure, and it limits how much can be scientifically concluded from these results.

In each of the pumping measurements, the VNA probing power was set at -10 dBm, while the pump power varied from -20 dBm to 10 dBm. The results of these measurements are given in figure 3.17. These figures show the power dependence of each linewidth at the three different pumping frequencies, and also the dependence of linewidth on VNA probing without pumping, i.e. the initial CW spectroscopy, for comparison. The straight lines drawn through the data points are a visual tool to show the general trend. They clearly are not accurate fits derived from a model of sorts, and therefore should not be taken to quantify anything except for the most basic nature of the power dependence. The interpretation of these results is given in section 4.

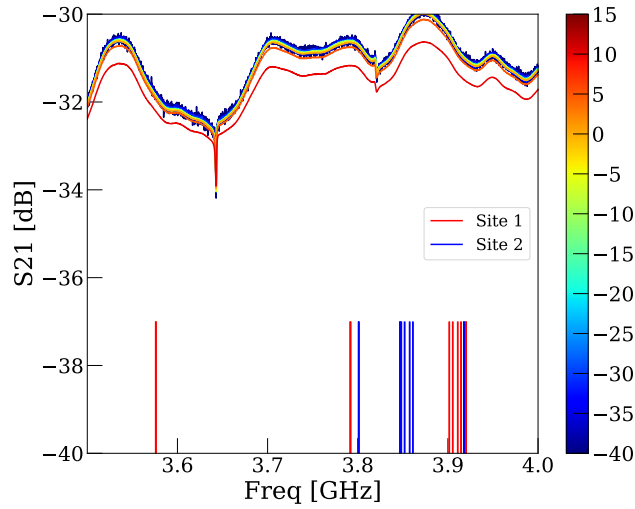


(a) Unprocessed measurement data of group delay

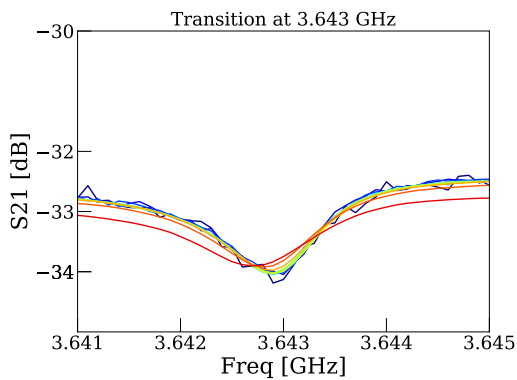


(b) unprocessed data of amplitude spectrum.

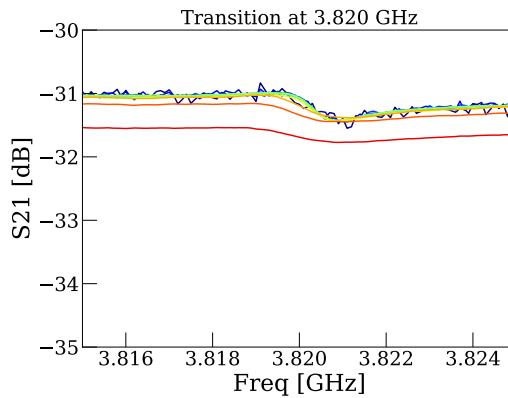
Figure 3.14: Broadband spectrum used to detect signatures of spin resonances by their power dependence.



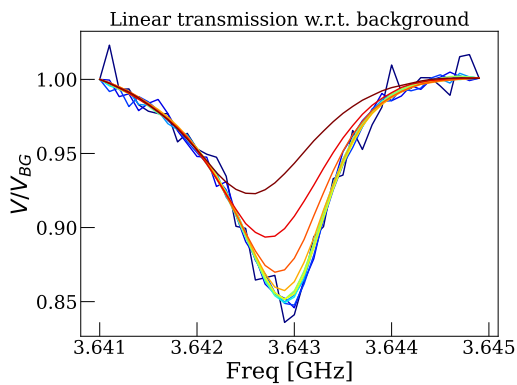
(a) Broadband transmission. unprocessed data and added peaks indicating resonance frequencies found with Easyspin.



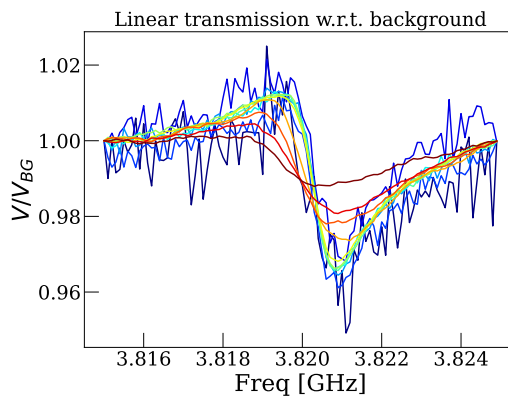
(b) Zoom of unprocessed data.



(c) Zoom of unprocessed data.

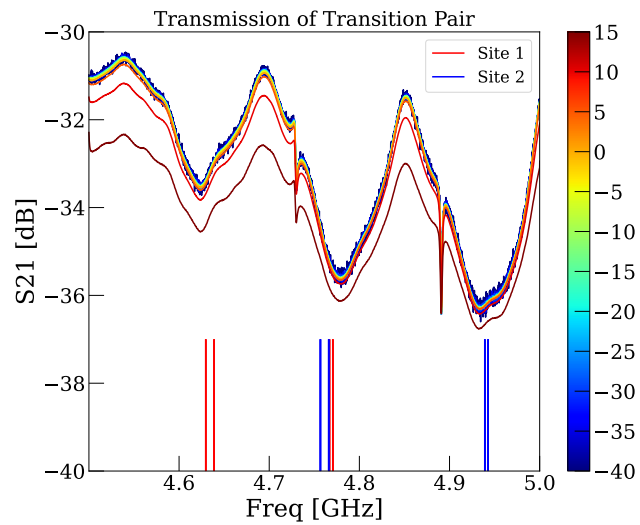


(d) Processed data.

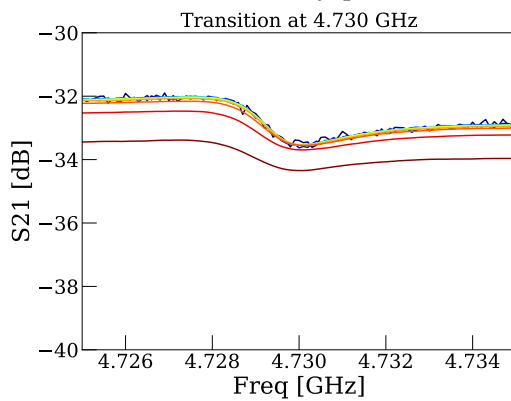


(e) Processed data.

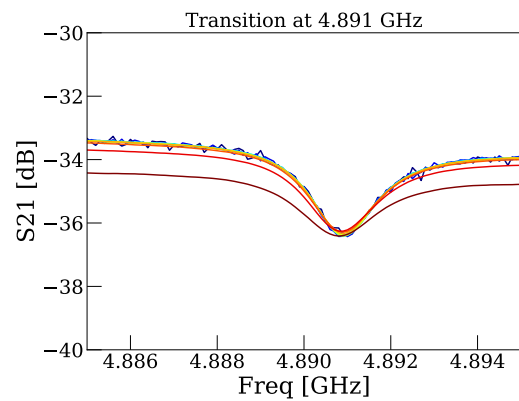
Figure 3.15: Data of peak pair about 3.7 GHz.



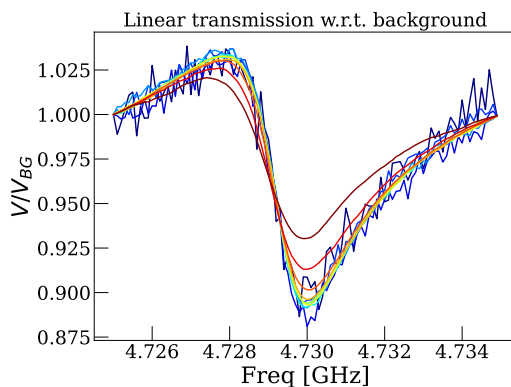
(a) Broadband transmission. unprocessed data and added peaks indicating resonance frequencies found with Easyspin.



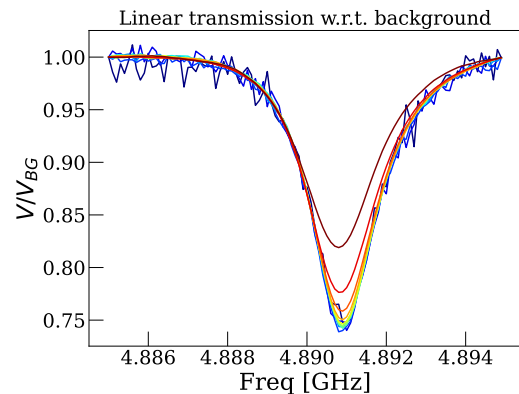
(b) Zoom of unprocessed data.



(c) Zoom of unprocessed data.



(d) Processed data.



(e) Processed data.

Figure 3.16: Peak pair about 4.8 GHz

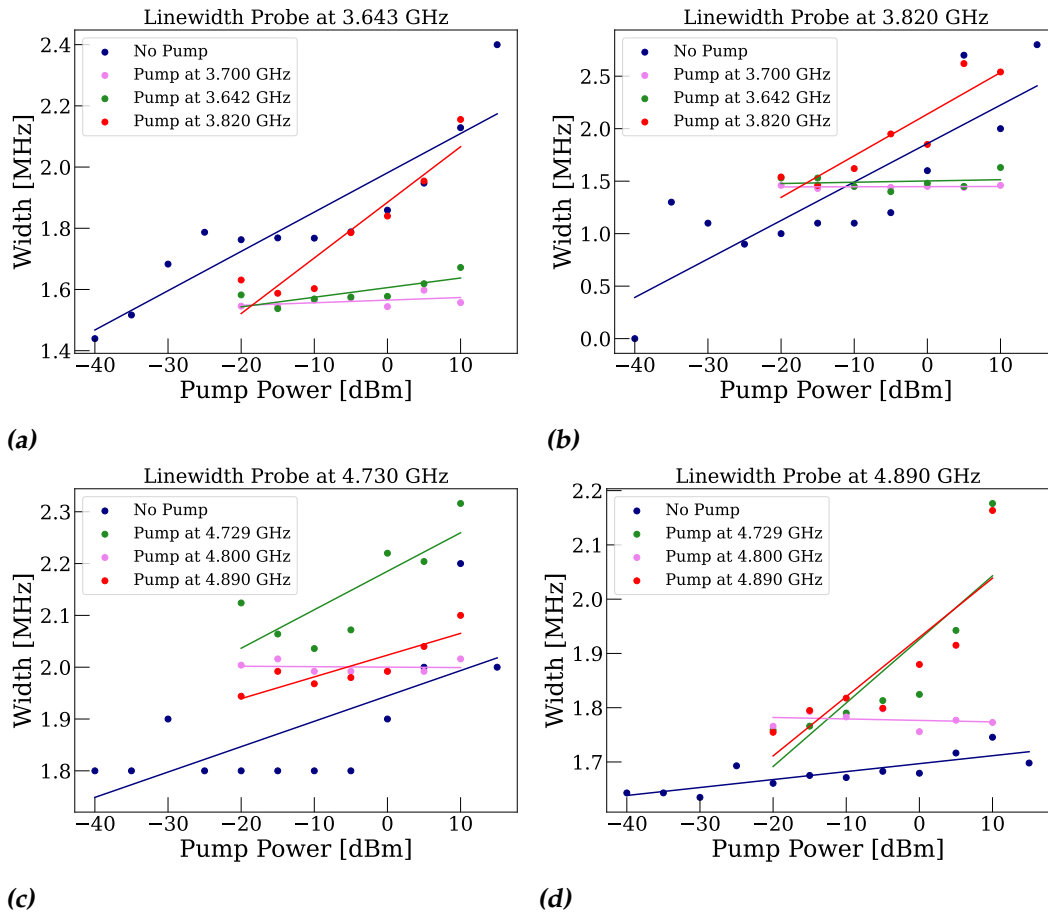


Figure 3.17: Power dependence of each determined linewidth. The 3.643 GHz and 4.890 GHz linewidths were determined by fitting, while those of 3.820 GHz and 4.730 GHz were estimated from the gradient of the data. Also shown is the power dependence when the probing power of the VNA was swept, without applying pumping.

Conclusion

Simulation and Fabrication

Finite element models were designed and simulated in the software CST Studio Suit. From this, the optimal geometric parameters of coplanar waveguides suitable for CW ESR spectroscopy were derived. Optimal in the sense of good broadband transmission, and proper impedance matching. Using these parameters a chip layout containing two CPWs was designed. This layout was also simulated and optimised for transmission, impedance, and small crosstalk between lines. This layout was also adjusted to fulfill the requirements for in-house fabrication.

Consequently, this layout was fabricated using the optical lithography of a thin niobium film on a silicon chip. The fabrication process made use of recipes that have become standard practice at the Walther-Meissner-Institut for the fabrication of niobium resonators and waveguides, used in for example transmon circuits.

The transmission and crosstalk of four waveguides on two different chips were measured at both room temperature and at 7 millikelvin. The room temperature measurements showed that the fabricated niobium waveguides are most likely unusable for room temperature ESR measurements. The cold measurements showed individual waveguide transmissions very comparable with simulations, and broadband behaviour in regimes where the circulator and amplifier transmission was relatively flat.

All in all, it seems that the fabrication installations at the Walther-Meissner-Institut, paired with cryogenic microwave measurement set-ups, can be used

to provide broadband solutions for CW ESR spectroscopy.

Magnetic Resonance Measurements

The transmission at 7 millikelvin of a double waveguide chip with a ^{167}Er -doped YSO crystal was analysed for the presence of magnetic resonance phenomena. Several potential electron spin resonances were identified by their power saturation behaviour. These candidate resonance frequencies seem reasonable values when compared to the literature. To gain a better indication of the absence or presence of spin resonance at these frequencies, time-dependent measurements should be done. This would allow one to quantify their relaxation behaviour and compare it to the background behaviour. Lack of time prevented such measurements to become part of this work.

Under the assumption that the mentioned features are in fact spin resonances, a pump-probe measurement scheme was performed. The results were analysed for the presence of phonon-mediated energy transfer between the respective spin ensembles coupled to each transmission line. This was qualified by the dependence of the absorption linewidth on the pump power. These results will now be interpreted.

The first important trend visible in figure 3.17, is that for all of probed (suspected) transitions the linewidth increased with pump power when the pump was directly in resonance with the transition. This is in agreement with the model presented in section 2.3. This is of course in confirmation with the idea of spin-phonon-spin transfer, but can just as well be caused by direct coupling of the electromagnetic field of the pump line to spins at the probe line. There are however several points of interest concerning the data that were in disagreement with the latter being the possibility.

Making use of the broadband capabilities of transmission line ESR, we can pump at one resonance, while probing the other. In essence, we want to check if there is a measurable change probed in a line not in resonance with the pump. There is no clear dependence between any of the transition linewidth and the pumps at background frequencies 3.7 GHz resp. 4.8 GHz. This seems to suggest that the linewidths do not change due to the absorption of microwave power by the dielectric and consequent general heating of the spin ensemble.

When the pumping is at the other resonance frequencies the response seems to differ depending on which of the lines was pumped or probed. For pumping at 4.890 GHz or 3.820 GHz, there seems to be a linewidth depen-

dence at the lower resonance frequencies 4.730 GHz resp. 3.643 GHz. For the latter, the response is even stronger than for resonant pumping. When measurements are performed the other way around, there is a power dependence of the linewidth at 4.89 GHz on pumping at 4.73 GHz. For the other pair, this is not true, which means that it is unclear how fast the non-equilibrium population of phonons relaxes back into a thermal distribution. The answer to this question would shine a light on Bogoliubov's assumption of a relaxation time hierarchy.

This relates back to questions asked in section 2.2.3 about the dominant source of phonon relaxation. Given the nature of the measurements, this question cannot be answered here. It is, however, surprising how much the linewidth seems to change compared to direct measurement and resonant pumping for both pairs since the assumed interaction mechanism behind this is phonon cross-relaxation. In light of this result, it seems that the estimates given on phonon cross-relaxation in section 2.2.3 overestimate the timescale of frequency down-conversion by phonon interaction.

The pump-probe measurements seem to indicate that a phonon bottleneck effect is present in the studied system at 7 millikelvin, and that this affects the electron spin linewidth. However, more measurements of the presented type, in addition to measurements on time dependence are needed to confirm the suspicions presented here, providing an interesting potential research direction. All in all, it seems too early to draw any strong conclusions.

Acknowledgments

The author is grateful towards Nadezdha Kukharchyk for allowing him to be part of the group and partaking in the fascinating world of rare earth spin physics, and also for the continuous guidance throughout the duration of the project. Also, the author is grateful towards prof. Rudolf Gross for hosting me at the institute and for grading the thesis. Also thanked are the other members of the REMWSys group for all the fruitful and fun discussions. Ana Strinic in particular is thanked for her help in preparing and performing the microwave measurements. Furthermore, gratitude is expressed towards Niklas BrÄEckmoser's guidance in all relating to the fabrication processes. And finally, the emotional support and comical relief from all the students in office 128 during the last 6 months must be mentioned, since it was a crucial ingredient in performing this work.

Appendix A

Derivation of Kinetic Equations

The kinetic equations for the expectation values of operators within the NSO formalism are derived here.

It can be shown that the integral of in equation 2.21 ensures onsistency $\lim_{\epsilon \rightarrow 0} \langle R_n \rangle_\epsilon(t) = \langle R_n \rangle_{rel}(t) = \langle R_n(t) \rangle_{NSO} \stackrel{\text{def}}{=} \langle R_n \rangle(t)$ under the condition that ρ_ϵ stays normalised.[85][108] It is the definition of the so called *invariant part* $\overline{\rho_{rel}}$. Note that such consistency is not ensured for expectation values of general quantities, for example, $\langle \dot{R}_n(t) \rangle_{rel} \neq \langle \dot{R}_n(t) \rangle$ in general. We rewrite:

$$\begin{aligned} \rho_\epsilon(t) &= \epsilon \int_{-\infty}^t e^{\epsilon(\tau-t)} U(t; \tau) \rho_{rel}(\tau) U^\dagger(t; \tau) d\tau \\ &= \epsilon \int_{-\infty}^0 e^{\epsilon(\tau)} U(t; t + \tau) \rho_{rel}(t + \tau) U^\dagger(t; t + \tau) d\tau = \overline{\rho_{rel}(t)} \end{aligned}$$

Where the latter implies:

$$\overline{\rho_{rel}(t)} = \frac{1}{Z(t)} e^{-\sum_n \lambda_n(t) R_n}$$

And:

$$\begin{aligned} \overline{\lambda_n(t) R_n} &= \epsilon \int_{-\infty}^0 d\tau e^{\epsilon\tau} \lambda_n(t + \tau) R_n(\tau) \\ &= \lambda_n(t) R_n - \int_{-\infty}^0 d\tau e^{\epsilon\tau} (\dot{\lambda}_n(t + \tau) R_n(\tau) + \lambda_n(t + \tau) \dot{R}_n(\tau)) \end{aligned}$$

In the last line integration by parts was used. During this procedure, for the terms $R_n(\tau)$ in the integrand a Heisenberg time dependence is implied. Concluding, the NSO is written as:

$$\rho_{NSO}(t) = \frac{1}{Z(t)} \exp \left(- \sum_n \lambda_n(t) R_n \right. \\ \left. + \lim_{\epsilon \rightarrow 0} \sum_n \int_{-\infty}^0 d\tau e^{\epsilon\tau} (\dot{\lambda}_n(t+\tau) R_n(\tau) + \lambda_n(t+\tau) \dot{R}_n(\tau)) \right)$$

If we define the entropy as operator $S = \ln \rho$, which is a functional of $\lambda_n(t) R_n$, we are able to write the variables $\lambda_n(t)$ and $\langle R_n \rangle(t)$ as conjugate pair of distribution derivatives.

$$\langle R_n \rangle = - \frac{\delta Z}{\delta \lambda_n} \\ \langle \lambda_n \rangle = \frac{\delta S}{\delta \langle R_n \rangle}$$

Now the kind of systems of interest to us is of the form:

$$H = H_0 + H_I$$

with the interaction H_I weak compared to the free particle term H_0 . Furthermore, it is assumed that the free motion of the relevant operators is of the form:

$$[H_0, R_n] = \sum_m c_{nm} R_m$$

such that:

$$\frac{d}{dt} R_n = \dot{R}_n = i[H, R_n] = i \sum_m c_{nm} R_m + i[H_I, R_n]$$

On the same note:

$$\frac{d\lambda_n(t)}{dt} = \sum_\ell \frac{\partial \lambda_n(t)}{\partial \langle R_\ell \rangle} \langle \dot{R}_\ell \rangle = \sum_\ell \frac{\partial \lambda_n(t)}{\partial \langle R_\ell \rangle} \left(i \sum_m c_{\ell m} \langle R_m \rangle + i \langle [H_I, R_\ell] \rangle \right)$$

Now a less trivial statement is made. As was discussed in the main text, $\rho_{rel}(t_0)$ is taken to be the initial condition to the equilibration process described by $\rho_{NSO}(t)$. In the sense of Bogoliubov's hierarchy of timescales, at t_0 the system has sufficiently relaxed that we may take $\rho_{rel}(t_0)$ to be a Gibbs distribution in the variables $\lambda_n(t) R_n$. During times $t > t_0$ the system will

relax further into full thermal equilibrium. We now assume that this second part of the dynamics is fully governed by H_I , such that we may take:

$$\sum_{nm} \lambda_n c_{nm} R_m = \langle [H_0, \sum_n \lambda_n R_n] \rangle = 0$$

From this is derived:

$$0 = \frac{\partial}{\partial \lambda_k} 0 = \frac{\partial}{\partial \lambda_k} \langle [H_0, \sum_n \lambda_n R_n] \rangle = \sum_n \lambda_n c_{nk} + \sum_{nm} \frac{\partial \lambda_n}{\partial \langle R_k \rangle} c_{nm} \langle R_m \rangle$$

And from the commutativity of derivatives:

$$\frac{\partial \langle R_\ell \rangle}{\partial \lambda_k} = - \frac{\delta^2 Z}{\delta \lambda_k \delta \lambda_\ell} = \frac{\partial \langle R_k \rangle}{\lambda_\ell}$$

From the last two equations we can identify:

$$\sum_{\ell m} \frac{\partial \lambda_n}{\partial \langle R_\ell \rangle} c_{\ell m} \langle R_m \rangle = - \sum_k \lambda_k c_{kn}$$

Such that:

$$\frac{d\lambda_n(t)}{dt} = -i \sum_k \lambda_k c_{kn} + i \sum_\ell \frac{\partial \lambda_n(t)}{\partial \langle R_\ell \rangle} \langle [H_I, R_\ell] \rangle$$

We then can can rewrite ρ_{NSO} as:

$$\rho_{NSO}(t) = \frac{1}{Z(t)} \exp \left(- \sum_n \lambda_n(t) R_n + \lim_{\epsilon \rightarrow 0} \sum_n \int_{-\infty}^0 d\tau e^{\epsilon \tau} \right. \\ \left. \times \left(i \sum_\ell \frac{\partial \lambda_n(t+\tau)}{\partial \langle R_\ell \rangle} \langle [H_I(t+\tau), R_\ell(t+\tau)] \rangle R_n(\tau) + i \lambda_n(t+\tau) [H_I(\tau), R_n(\tau)] \right) \right)$$

We now consider the equations of motion of $\langle R_n \rangle(t)$ in the nonequilibrium state. The Heisenberg equation gives:

$$\langle \dot{R}_k \rangle(t) = i \langle [H, R_k(t)] \rangle = i \sum_m c_{km} \langle R_m \rangle(t) + i \langle [H_I, R_k(t)] \rangle$$

Using the explicit form of what was found for $\rho_{NSO}(t)$, the goal is to expand the equation into powers of the interaction H_I , and to truncate this expansion at appropriate order.

The first term in the exponent of ρ_{NSO} is $-\sum_n \lambda_n R_n$, which does not contain H_I and is simply the exponent of ρ_{rel} . Therefore the zeroth and first order terms of the expansion are simply:

$$\langle \dot{R}_k \rangle^{(0,1)}(t) = i \sum_m c_{km} \langle R_m(t) \rangle + i \langle [H_I, R_k(t)] \rangle_{rel}$$

For the second order term, we approximate the dynamics using the correlation functions of the form $C_\beta\{A, B\} = \int_0^1 ds \langle A e^{-\beta s} (B - \langle B \rangle_{rel}) e^{\beta s} \rangle_{rel}$, in our case with $\beta = \sum_n \lambda_n R_n$

This results in:

$$\begin{aligned} \langle \dot{R}_k \rangle^{(2)}(t) &= \lim_{\epsilon \rightarrow 0} (i)^2 \sum_n \int_{-\infty}^0 d\tau e^{\epsilon\tau} (C_\beta\{[H_I, R_k], [H_I(\tau), R_n(\tau)]\} \lambda_n(t + \tau) \\ &\quad + C_\beta\{[H_I, R_k], R_n(\tau)\} \sum_\ell \frac{\partial \lambda_n(t + \tau)}{\partial \langle R_\ell \rangle} \langle [H_I(\tau), R_\ell(\tau)] \rangle_{rel}) \end{aligned}$$

The second order will be included in the expansion but is done so within the Markov approximation, taking $\lambda_n(t + \tau) R_n(\tau) \approx \lambda_n(t) R_n$ in the integrand. In that case, if we approximate $\frac{\partial}{\partial \lambda_k} \exp(-\sum_n \lambda_n R_n) \approx \int_0^1 ds e^{-\beta s} R_k e^{\beta s}$, it can be proven, by taking the derivative explicitly, that:

$$C_\beta\{[H_I, R_k], R_n(\tau)\} = i \frac{\partial \langle \dot{R}_k \rangle^{(1)}}{\partial \lambda_n} = i \sum_m \frac{\partial \langle \dot{R}_k \rangle^{(1)}}{\partial \langle R_m \rangle} \frac{\partial \langle R_m \rangle}{\partial \lambda_n}$$

It can also be identified that:

$$\begin{aligned} &\int_{-\infty}^0 d\tau e^{\epsilon\tau} C_\beta\{[H_I, R_k], [H_I(\tau), R_n]\} \lambda_n(t) \\ &= \int_{-\infty}^0 d\tau e^{\epsilon\tau} \int_0^1 ds \langle [H_I, R_k] e^{-\beta s} ([H_I(\tau), \lambda_n(t) R_n] - \langle [H_I(\tau), \lambda_n(t) R_n] \rangle_{rel}) e^{\beta s} \rangle_{rel} \\ &= \int_{-\infty}^0 d\tau e^{\epsilon\tau} \int_0^1 ds \langle [H_I, R_k] \frac{d}{ds} e^{-\beta s} (H_I(\tau) - \langle H_I \rangle_{rel}) e^{\beta s} \rangle_{rel} \\ &= \int_{-\infty}^0 d\tau e^{\epsilon\tau} \langle [H_I(\tau), [H_I, R_k]] \rangle_{rel} \end{aligned}$$

The final result is the kinetic equation for $\langle R_k \rangle$ in second order:

$$\begin{aligned} \langle \dot{R}_k \rangle = & i \sum_m c_{km} \langle R_m \rangle + i \langle [H_I, R_k] \rangle_{rel} \\ & - \lim_{\epsilon \rightarrow 0} \int_{-\infty}^0 d\tau e^{\epsilon\tau} \left(\langle [H_I(\tau), [H_I, R_k]] \rangle_{rel} \right. \\ & \left. + i \sum_{m\ell} \frac{\partial \langle [H_I, R_k] \rangle_{rel}}{\partial \langle R_m \rangle} \frac{\partial \langle R_m \rangle}{\partial \lambda_n} \frac{\partial \lambda_n}{\partial \langle R_\ell \rangle} \langle [H_I(\tau), R_\ell] \rangle_{rel} \right) + \mathcal{O}(H_I^3) \end{aligned}$$

Data Analysis

B.1 Linearisation

As was mentioned in section 3.2, power-dependent features were found in the transmission spectra by looking at both the amplitude and phase of $S_{21}(\omega)$. Once such a feature was identified, the next step was usually to do another measurement over a more narrow frequency band around the feature, with better resolution and more averages. This second dataset would then be processed further. This was done in the following steps.

The potential absorption feature would be sliced out of the dataset with a sufficient amount of background data. If the direct signature of a pump was present, this would be removed, see also next section. The next steps are also illustrated in figure B.1b.

The background at frequencies surrounding the absorption feature was taken to be (locally) linear. The background was thus extrapolated as a straight line:

$$S_{21}^{BG}(\omega) = a \cdot \omega + S_{21}(\omega_0)$$

with S_{21} still in dB and ω_0 the lowest frequency of the sliced dataset. If ω_1 was the highest frequency of the slices dataset, then a is given by:

$$a = \frac{S_{21}(\omega_1) - S_{21}(\omega_0)}{\omega_1 - \omega_0}$$

This line was then subtracted from S_{21} , to obtain the logarithmic transmission with respect to the background, $S_{21}^n(\omega)$.

$$S_{21}^n(\omega) = S_{21}(\omega) - S_{21}^{BG}(\omega)$$

Note that this ensures $S_{21}^n(\omega_1) = S_{21}^n(\omega_0) = 0$ dB. The relation between the logarithmic and linear transmission is given by:

$$S_{21}[-] = \frac{V_2^- [\text{Volt}]}{V_1^+ [\text{Volt}]} \sim \frac{V_{out} [\text{Volt}]}{V_{in} [\text{Volt}]} = 10^{\frac{S_{21}[\text{dB}]}{20}}$$

This means that:

$$\begin{aligned} S_{21}(\omega)[\text{dB}] - S_{21}^{BG}(\omega)[\text{dB}] &= 20\log(V_{out}/V_{in}) - 20\log(V_{out}^{BG}/V_{in}) \\ &= 20\log(V_{out}/V_{out}^{BG}) \end{aligned}$$

So this means that we can convert to a linear scale by:

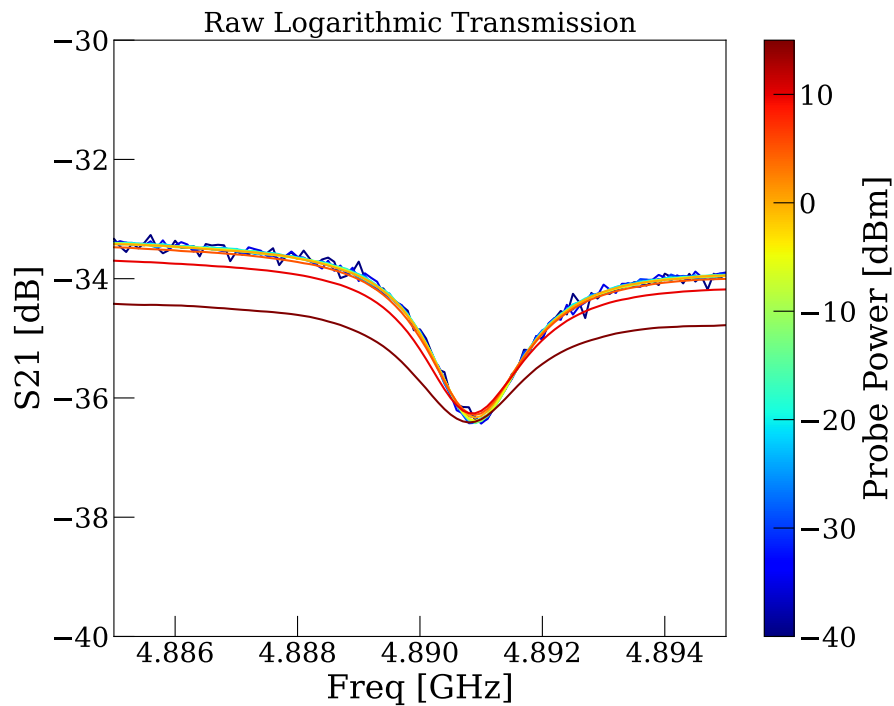
$$\frac{V_{out}}{V_{out}^{BG}} = 10^{S_{21}^n[\text{dB}]/20}$$

B.2 Pump Removal

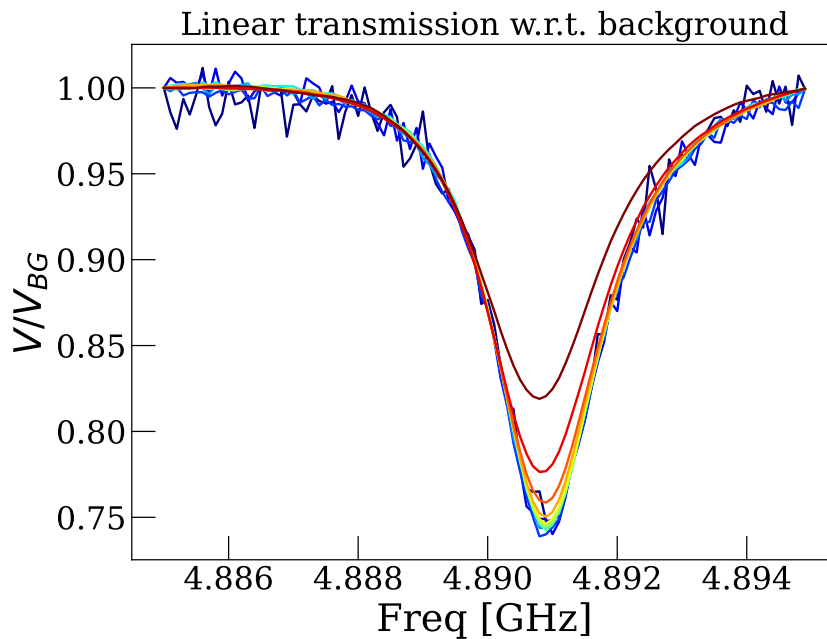
For resonant pump data, there would be a sharp peak in the VNA measurement at the frequency coinciding with that of the pump. If this coincided with the measured absorption feature, it would be removed from the data. This was done simply by detecting at which frequency bins it occurred and replacing the measured signal at these points by linear extrapolation from the surrounding signal. Figure B.2 illustrates the process.

B.3 Linewidth Determination

Linewidths were determined after linearisation using one of two methods, depending on the shape of the absorption. We distinguish 'nice' and 'bad' absorptions. For the data presented, the features at 3.643 GHz and 4.890 GHz are considered nice, while those at 3.820 GHz and 4.730 GHz are ugly. The nice ones could be fitted by either a Lorentzian or Gaussian distribution and the linewidth would be determined from the best fit. The author was not able to find good realistic fits that could consistently fit the ugly transmissions. For these profiles, instead of fitting, the gradient with respect to the frequency axis was calculated, resulting in an asymmetric curve, that always has a clear global minimum and maximum. The linewidth would then be taken as the peak-to-peak frequency spacing of the gradient. To accurately determine the frequencies corresponding to the gradient minimum and maximum, a moving average filter was applied to remove noise.

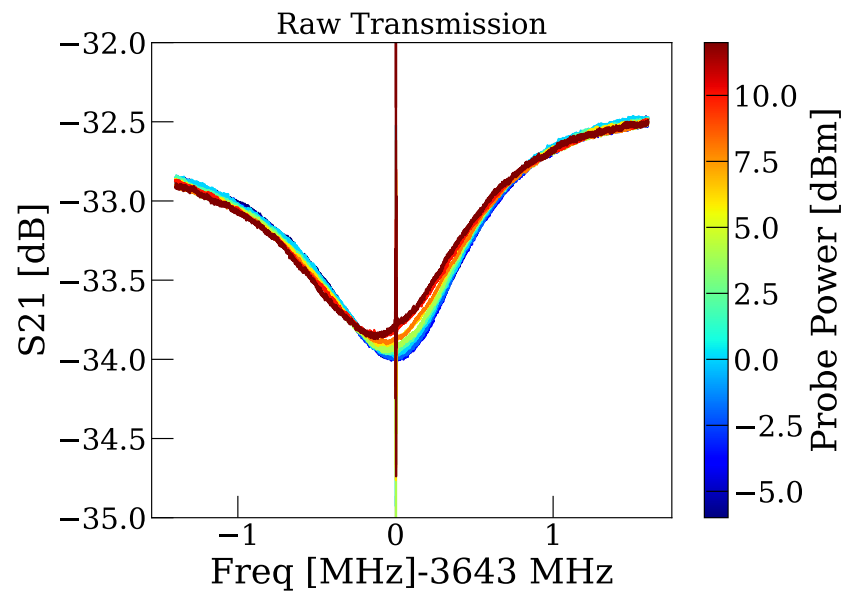


(a) unprocessed transmission data from a nice looking, i.e. fittable feature.



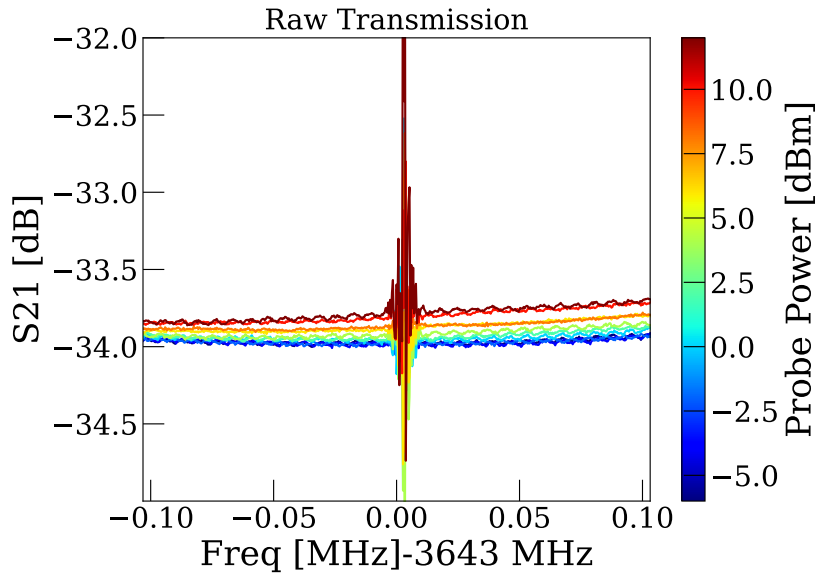
(b) Transmission data, normalised with respect to the background and converted to a linear scale. Note that the background is now at 1.

Figure B.1: Set of plots illustrating background subtraction and linearisation of unprocessed data.

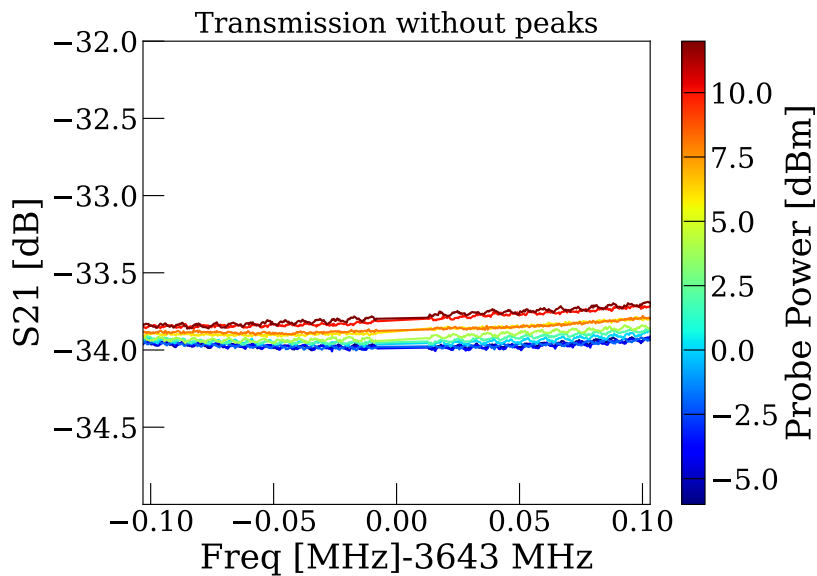


(a) unprocessed data from pump measurement. Note the obvious peak, distinguishable from the global power-dependence.

This method could be applied consistently to all ugly, but also to all the nice curves. In fact, if a data set contained both ugly and nice absorptions, the method would first be applied to the nice ones. From this, the appropriate window size for the moving average filter could be determined, such that the method resulted in linewidths that most closely matched those of the best fit. Using this choice of filter the method would be applied to the other ugly profiles. In figures B.3 and B.4 the method is illustrated for a nice and ugly absorption respectively.

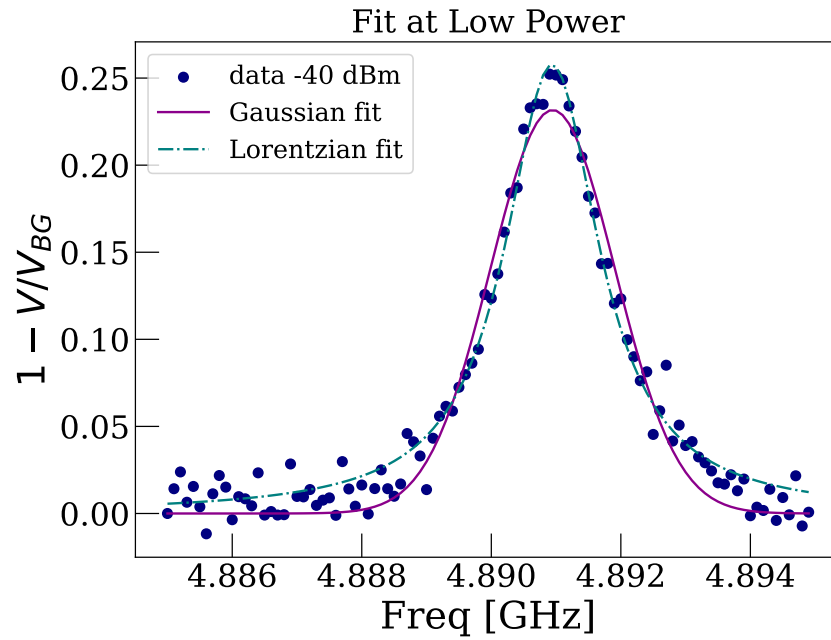


(b) unprocessed data from pump measurement, zoomed in to the peak caused by direct electromagnetic coupling between transmission lines.

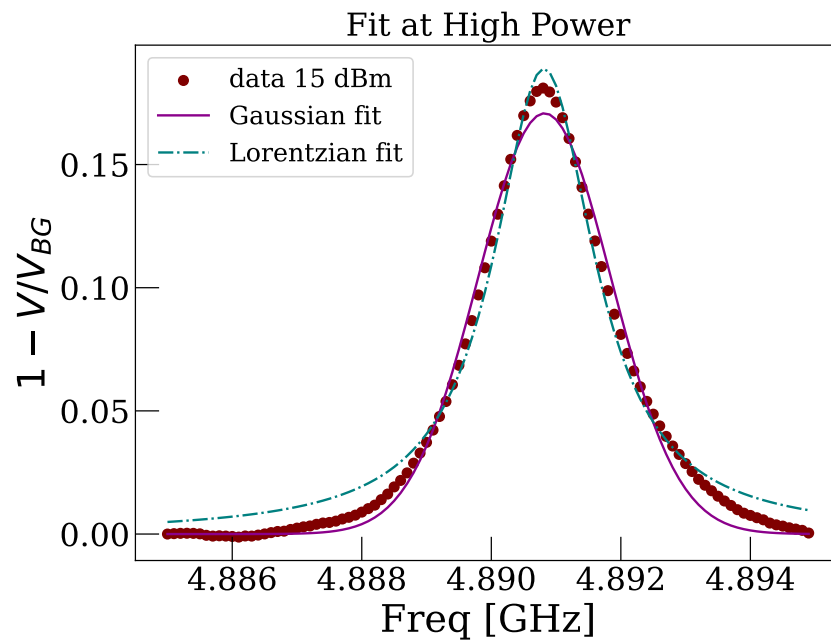


(c) Transmission data, but the peak is removed and replaced by linear extrapolation of the global lineprofile.

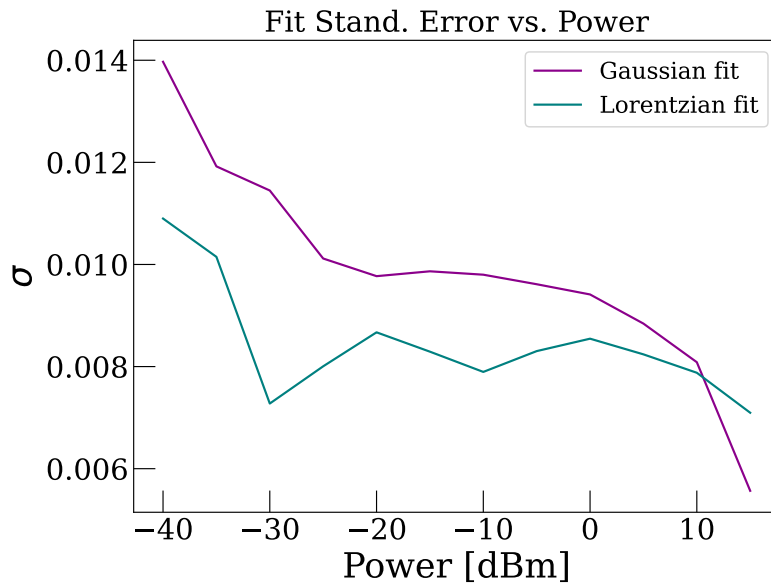
Figure B.2: Plots illustrating the process of removing the direct coupling peak from some of the pump spectra.



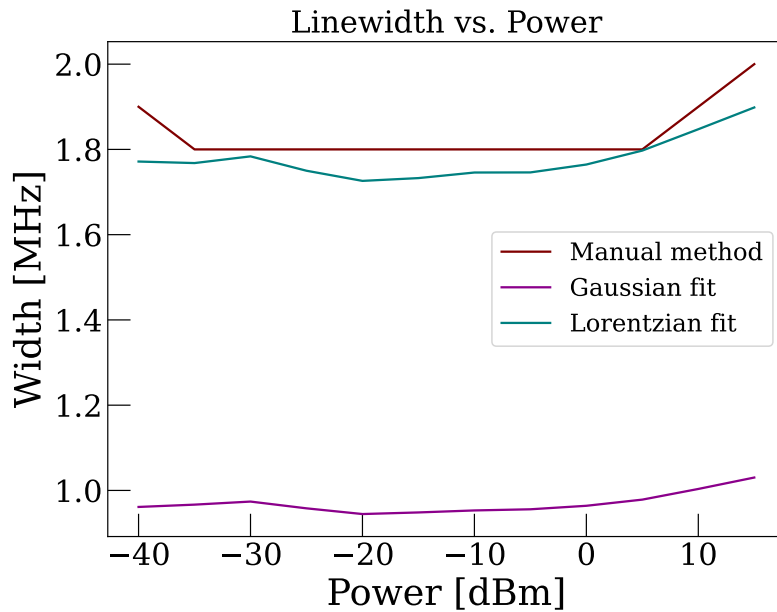
(a) Example of Lorentzian and Gaussian fit at low VNA power.



(b) Example of Lorentzian and Gaussian fit at high VNA power.

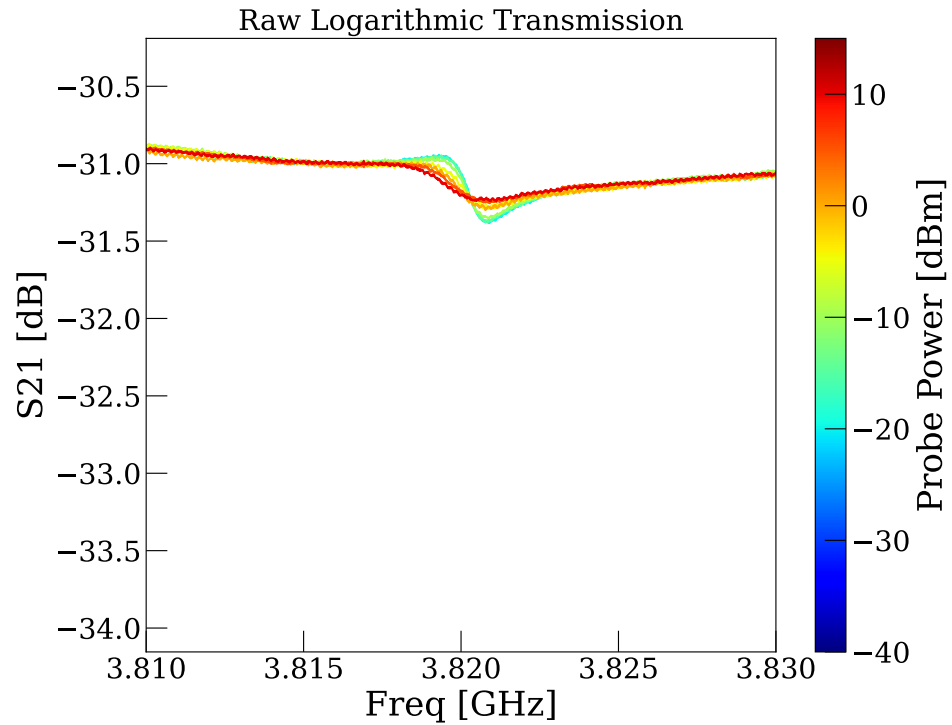


(c) Standard deviation of fit with respect to the data for a Gaussian and Lorentzian fit.

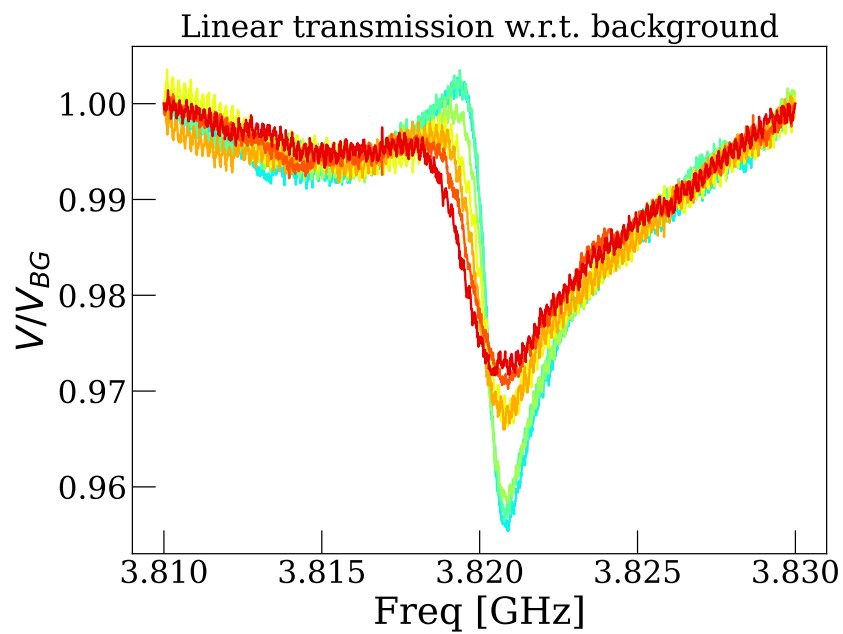


(d) Power dependence of the linewidth as determined by Gaussian or Lorentzian fitting and by the described method based on taking the data gradient. The best fit, Lorentzian, matches well with the result from the manual method.

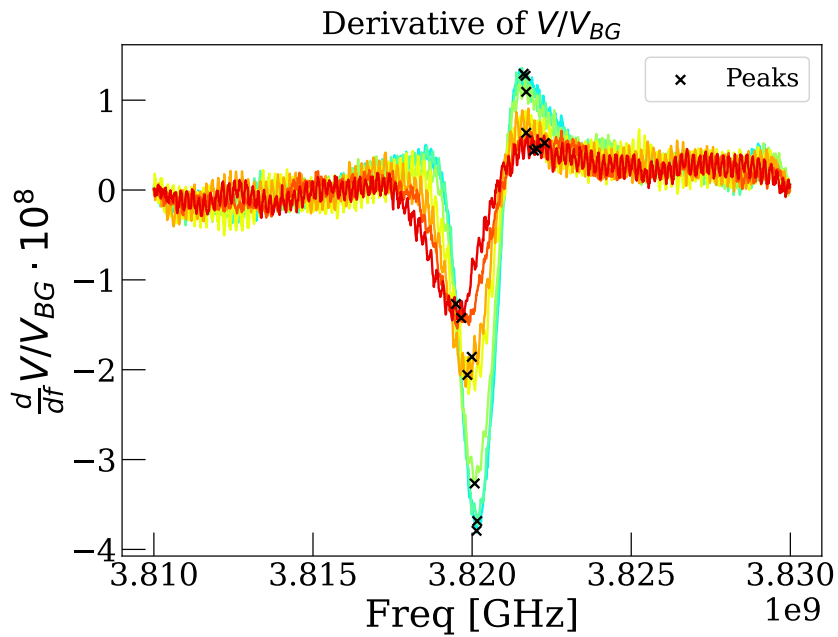
Figure B.3: Plots illustrating linewidth determined from optimal fit parameters for nice peaks.



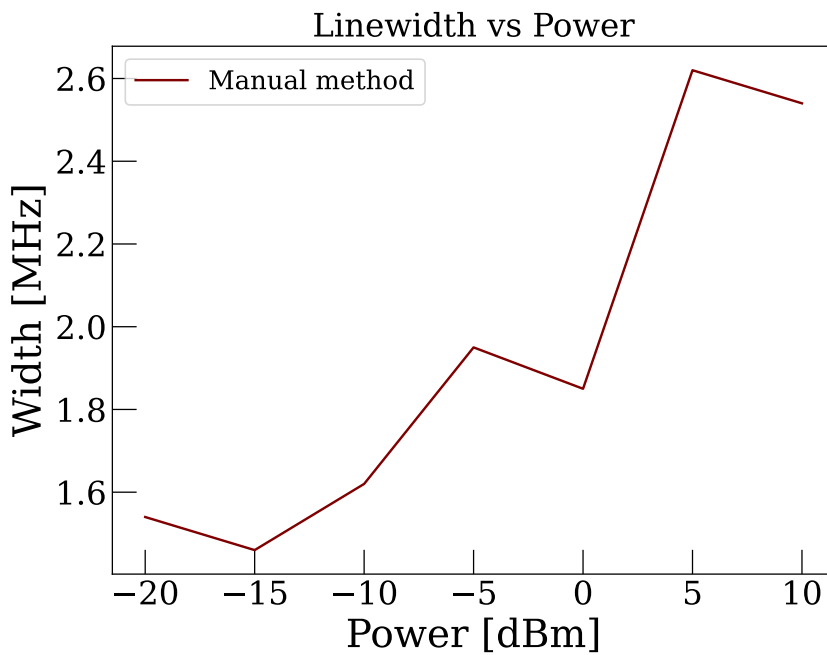
(a) unprocessed transmission of ugly feature.



(b) Linearised transmission with respect to the background of ugly feature.



(c) Gradient of linearised transmission feature that has gone through a moving average filter. Detected peaks are indicated.



(d) Resulting power dependence of the linewidth determined by taking the gradient of the processed data.

Figure B.4: Plots illustrating linewidth determined from peak-to-peak width of derivative for ugly peaks.

Fabrication Recipe

Initial Substrate Cleaning

- Bathe in 80 °C acetone for 5 minutes.
- In ultrasonic bath with acetone for 2 min at 25 °C bath temperature and Leistung 9.
- Quick room temperature IPA dip.
- Blow dry with nitrogen gun.

Sputtering in Plassys

- Niobium sputtering with DC power $P = 300\text{W}$, $T = 255^\circ\text{C}$ $p = 3.7\text{mTor}$ for in total $7\frac{1}{2}$ minutes, leading to an approximate film thickness of 150 nm.

Optical Lithography

- Spincoating of 40 microliter photoresist AZ MiR 701.
- Prebake for 75s at 90°C.
- Laserwriter settings: 300 nm spot size, 120 mJ dosage. Grid size 100nm, and adaptive feedforward switched on at 200nm.
- Postbake for 90s at 110°C.

Development

- Stir sample for 70s in AZ726 Mif, then stir in two different water beakers, for at least 10 seconds each.

- Blow dry with nitrogen gun.

Reactive Ion Etch

- Etching at SF₆ only flow of 20 sccm at 100 W feedforward power and 50 W RF power. Reflected power should be close to 0 W.
- Etching should last 2:50 min.

Resist Stripping

- Place sample in beaker with Technistrip P1331 into ultrasonic bath for 2 min, 25 °C, Leistung 5.
- Heat beaker with sample on hot plate at 80 °C for 2 minutes.
- Stir sample in two water beakers for at least 10 seconds in each.

Final Cleansing

- 2 min ultrasonic bath Leistung 5 in 80 °C acetone, followed by
- 2 min ultrasonic bath Leistung 5 in 80 °C IPA.
- Blow dry with nitrogen gun.

Wire Bonding Unfortunately, no consistently working recipe was found. General guidelines:

- Make sure that the search height is not too far away from the actual height of the sample. It is unclear why this should matter, but in the author's experience, it does.
- If the wire does not bond, and moves back up with the wedge, increase US power.
- If the wire bonds, but is pulled loose again by the wedge, decrease US power.
- If the wire in the wedge does not fold over the wedge slightly towards you, the bond is very likely to fail.
- If a bond fails, do not try to bond with the same section of wire again.

Bibliography

- [1] Zhang, E.J. (2022) *High-Performance Superconducting Quantum Processors via Laser Annealing of Transmon Qubits*. Science Advances Vol. 8, eabi6690
- [2] de Riedmatten, H. et al. (2008) *A solid-state light-matter interface at the single-photon level* Nature Vol. 456, pp. 773-777
- [3] Jobez, P. et al. (2016) *Towards Highly Multimode Optical Quantum Memory for Quantum Repeaters*. Phys. Rev. A Vol. 93, 032327
- [4] Nunn, J. et al. (2008) *Multimode Memories in Atomic Ensembles*. Phys. Rev. Lett. Vol. 101, 260502
- [5] Rančić, M. et al. (2018) *Coherence Time of over a Second in a Telecom-Compatible Quantum Memory Storage Material*. Nature Physics Vol. 14 pp. 50-54
- [6] Könz, F. et al. (2003) *Temperature and Concentration Dependence of Optical Dephasing, Spectral-Hole Lifetime, and Anisotropic Absorption in $\text{Eu}^{3+}:\text{Y}_2\text{SiO}_5$* . Phys. Rev. B Vol. 68, 085109
- [7] Probst, S. et al. (2013) *Anisotropic Rare-Earth Spin Ensemble Strongly Coupled to a Superconducting Resonator* Phys. Rev. Lett. Vol. 110, 157001
- [8] Probst, S. et al. (2015) *Microwave Multimode Memory with an Erbium Spin Ensemble* Phys. Rev. B. Vol. 92, 014421
- [9] Malissa, H. et al. (2013) *Superconducting Coplanar Waveguide Resonators for Low Temperature Pulsed Electron Spin Resonance Spectroscopy*. Rev. Sci. Instrum. Vol. 84, 025116

-
- [10] Afzelius, M. et al. (2009) *Multimode Quantum Memory Based on Atomic Frequency Comb*. Phys. Rev. A Vol. 79, 052329
- [11] Julsgaard, B. et al. (2013) *Quantum Memory for Microwave Photons in an Inhomogeneously Broadened Spin Ensemble*. Phys. Rev. Lett. Vol. 110, 250503
- [12] Hahn, E.L. (1950) *Spin Echoes*. Phys. Rev. Vol. 80, 580
- [13] Fleischhauer, M. et al. (2005) *Electromagnetically Induced Transparency: Optics in Coherent Media*. Rev. Mod. Phys. Vol. 77, 633
- [14] Kukharchyk, N. et al. (2020) *Electromagnetically Induced Transparency in a Mono-Isotopic $^{167}\text{Er}^{3+}:\text{Y}_2\text{SiO}_5$ crystal below 1 Kelvin: Microwave Photonics Approach*. Optics Express Vol. 28, No. 20, 29166
- [15] Sangouard, N. et al. (2007) *Analysis of a Quantum Memory for Photons based on Controlled Reversible Inhomogeneous Broadening*. Phys. Rev. A Vol. 75, 032327
- [16] Ortu, A. et al. (2022) *Multi Mode Capacity of Atomic-Frequency Comb Quantum Memories*. Quantum Sci. Technol. Vol. 7, 035024
- [17] Arslanov, N.M. Moiseev, S.A. (2017) *Optimal Periodic Frequency Combs for High-Efficiency Optical Quantum Memory Based on Rare-Earth Ion Crystals*. Kvantovaya Elektronika Vol. 47, No. 9, pp. 783-789
- [18] Guo, M. et al. (2023) *Rare-Earth Quantum Memories: The Experimental Status Quo*. Frontiers of Physics Vol. 18, Iss. 2, 21303
- [19] Clauß, C. et al. (2013) *Broadband Electron Spin Resonance from 500 MHz to 40 GHz using Superconducting Coplanar Waveguides*. Appl. Phys. Lett. Vol. 102, 162601
- [20] Wiemann, Y. et al. (2015) *Observing Electron Spin Resonance between 0.1 and 67 GHz at Temperatures between 50 mK and 300 K using Broadband Metallic Coplanar Waveguides*. Appl. Phys. Lett. Vol. 106, 193505
- [21] Orbach, R. (1961) *Spin-Lattice Relaxation in Rare-Earth Salts*. Proc. R. Soc. A Vol. 264, Iss. 1319, pp. 458-484
- [22] van Vleck, J.H. (1941) *Paramagnetic Relaxation and the Equilibrium of Lattice Oscillators*. Phys. Rev. Vol. 59, 724
- [23] Abragam, A. Bleaney B. (1970) *Electron Paramagnetic Resonance of Transition Ions*. Clarendon Press, Oxford

- [24] Standley, K.J. Vaughan, R.A. (1969) *Electron Spin Relaxation Phenomena in Solids*. Plenum Press, New York
- [25] Budoyo, R.P. et al. (2018) *Phonon-Bottlenecked Spin Relaxation of $Er^{3+}:Y_2SiO_5$ at sub-Kelvin Temperatures*. Applied Physics Express Vol. 11, 043002
- [26] Kukharchyk, N. et al. (2018) *Optical Coherence of $^{166}Er^{3+}:LiYF_4$ Crystal below 1 K*. New. J. Phys. Vol. 20, 023044
- [27] Garanin, D.A. (2007) *Towards a Microscopic Understanding of the Phonon Bottleneck*. Physical Review B Vol. 75, 094409
- [28] Khutsishvili, G.R. (1965) *Spin Diffusion*. Usp. Fiz. Nauk Vol. 87, pp. 211-254
- [29] Merkel, B. (2021) *Enhancing the Emission and Coherence of Erbium Dopants*. Fakultät für Physik der Technischen Universität München
- [30] Böttger, T. (2006) *Optical Decoherence and Spectral Diffusion at 1.5 $\hat{C}Em$ in $Er^{3+}:Y_2SiO_5$ versus Magnetic Field, Temperature and Er^{3+} Concentration*. Phys. Rev. B Vol. 73, 075101
- [31] Mock, A. et al. (2018) *Anisotropy and Phonon Modes from Analysis of the Dielectric Function Tensor and the Inverse Dielectric Function Tensor of Monoclinic Yttrium Orthosilicate*. Phys. Rev. B Vol. 97, 165203
- [32] Kukharchyk, N. (2015) *Focused Ion Beam Implantation of Yttrium Orthosilicates with Erbium Ions for Applications in Quantum Computing*. Lehrstuhl für angewandte Festkörperphysik der Ruhr-Universität Bochum.
- [33] Wells, W.H. (2012) *The Lanthanides, Rare Earth Elements*. Patty's Toxicology, 6th Ed. Vol.1 John Wiley & Sons, New York
- [34] Elliott, J.P. et al. (1957) *Energy Levels in Rare-Earth Ions*. Proc. R. Soc. A Vol. 240, NO. 1223, pp. 509-523
- [35] Slichter, C.P. (1978) *Principles of Magnetic Resonance* (2nd Ed.) Springer Verlag, Berlin, Heidelberg
- [36] Vonsovskii, S.V. (1974) *Magnetism: Volume One* John Wiley & Sons, New York

- [37] Stevens, K.W.H. (1952) *Matrix Elements and Operator Equivalents Connected with the Magnetic Properties of Rare Earth Ions*. Proc. Phys. Soc. A Vol. 65, No.3 pp. 209-215
- [38] Bennati, Marina (2007) *EPR Interactions at Zero-field Splittings*. eMagRes, Vol. 6, pp. 271-282
- [39] Stoll, S. Goldfarb, D. (2007) *EPR Interactions at Nuclear Quadrupole Couplings*. eMagRehyps, Vol. 6, pp. 495-510
- [40] Guillot-Noël, O. et al. (2006) *Hyperfine Interaction of Er³⁺ ions in Y₂SiO₅: An Electron Paramagnetic Resonance Spectroscopy Study*. Physical Review B Vol. 74, 214409
- [41] Stoll, S. Schweiger, A. (2006) *EasySpin, a Comprehensive Software Package for Spectral Simulation and Analysis in EPR*. J. Magn. Reson. Vol. 178, No. 1, pp. 42-55
- [42] Schweiger, A. Jeschke, G. (2001) *Principles of Pulse Electron Paramagnetic Resonance*. University Press, Oxford
- [43] Portis, A.M. (1956) *Spectral Diffusion in Magnetic Resonance*. Phys. Rev. Vol. 104, 584
- [44] Rančić, M. et al. (2022) *Electron-Spin Spectral Diffusion in an Erbium Doped Crystal at millikelvin Temperatures*. Phys. Rev. B Vol. 106, 144412
- [45] Car, B. et al. (2019) *Optical Study of the Anisotropic Erbium Spin Flip-Flop Dynamics*. Phys. Rev. B Vol. 100, 165107
- [46] Portis, A.M. (1953) *Electronic Structure of F centers: Saturation of the Electron Spin Resonance*. Phys. Rev. Vol. 91, 1071
- [47] Eaton, G.R. et al. (2010) *Quantitative EPR*. Springer Verlag, Wien, New York
- [48] Somlo, P.I. (1963) *Some Aspects of the Measurement of the Q factor of Transmission Lines*. IEEE Transactions on Microwave Theory and Techniques. Vol. 11, Iss. 6, pp. 472-478
- [49] Steer, M.B. (2019) *Microwave and RF Design Volume 2: Transmission Lines*. (3rd Ed.) North Carolina State University Press, Raleigh
- [50] Pozar, D.M. (2011) *Microwave Engineering* (4th Ed.) John Wiley & Sons, New Jersey

- [51] Bahl, I. Bhartia, P. (2003) *Microwave Solid State Circuit Design* (2nd Ed.) John Wiley & Sons, New Jersey
- [52] Watanabe, K. et al. (1994) *Kinetic Inductance of Superconducting Coplanar Waveguides*. Jpn. J. Appl. Phys. Vol. 33, pp. 5708-5712
- [53] Ghione, G. Naldi, C. (1984) *Analytical Formulas for Coplanar Lines in Hybrid and Monolithic MICs*. Electronic Letters Vol. 20, No. 4, pp. 179-181
- [54] Veyres, C. Fouad Hanna, V. (1980) *Extension of the Application of Conformal Mapping Techniques to Coplanar Lines with Finite Dimensions*. Int. J. Electronics Vol. 1948, No 1. pp. 47-56
- [55] Steer, M.B. (2019) *Microwave and RF Design Volume 3: Networks*. (3rd Ed.) North Carolina State University Press, Raleigh
- [56] Rodin, B.A. Abergel, D. (2022) *Spin Relaxation: Is there anything new under the Sun?* Magn. Res. Vol. 3, pp. 27-41
- [57] Breuer, H. Petruccione, F. (2002) *The Theory of Open Quantum Systems*. University Press, Oxford
- [58] Waller, I. (1932) *Über die Magnetisierung von Paramagnetischen Kristallen in Wechselfeldern* Z. Phys. Vol. 79, pp. 370
- [59] Heitler, W. Teller, E. (1936) *Time Effects in the Magnetic Cooling Method*. Proc. Roy. Soc. London (A) Vol. 155, 629
- [60] Kronig, R. de L. (1939) *On the Mechanism of Paramagnetic Relaxation*. Physica VI No. 1, pp. 33-43
- [61] Nemati, S. et al. (2022) *Coupling Function from Bath Density of States*. Europhysics Letters, Vol. 139, No. 3, 6002
- [62] Klemens, P.G. *Thermal Conductivity and Lattice Vibrational Modes*. Solid State Physics Vol. 7, pp. 1-98
- [63] Sun, Z. et al. (2009) *Thermal Properties of Single-Phase Y_2SiO_5* . Journal of the European Ceramic Society Vol. 29, pp. 551-557
- [64] Heitler, W. (1944) *The Quantum Theory of Radiation* (2nd Ed.) University Press, Oxford
- [65] van Vleck, J.H. (1940) *Paramagnetic Relaxation Times for Titanium and Chrome Alum*. Phys. Rev. Vol. 57, 426

- [66] Faughan, B.W. Strandberg, M.W.P. (1961) *The Role of Phonons in Paramagnetic Relaxation*. J. Phys. Chem. Solids Vol. 19, No. 1/2, pp. 155-156
- [67] Levinson, I.B. (1980) *Propagation of Nonequilibrium Phonons with Frequency Down-conversion*. Mol. Cryst. Liq. Cryst. Vol. 57, pp. 23-28
- [68] Tucker, J.W. Rampton, V.W. (1972) *Microwave Ultrasonics in Solid State Physics*. North-Holland Publishing Company, Amsterdam
- [69] Gal'perin, Yu. M. et al. (1987) *Spectral Diffusion in Glasses at Low Temperatures. The "Burned-Out Hole" Phenomenon and Nonlinear Resonant Microwave and Sound Absorption*. Pis'ma Zh. Eksp. Teor. Fiz. Vol. 45, No. 2, pp. 85-88
- [70] Parshin, D.A. Rzaev, É.A. (1987) *Spectral Diffusion in Glasses*. Pis'ma Zh. Eksp. Teor. Fiz. Vol. 45, No. 7, pp. 344-347
- [71] Orbach, R. Vredevoe, L.A. (1964) *The Attenuation of High Frequency Phonons at Low Temperatures*. Physics, Vol. 1, No. 2, pp. 91-94
- [72] Kazakovtsev, D.V. Levinson, I.B. (1985). *Formation, Dynamics, and Explosion of a Phonon Hot Spot*. Zh. Eksp. Teor. Fiz. Vol. 88, pp. 2228-2243
- [73] Norambuena, A. et al. (2020) *Effect of Phonons on the Electron Spin Resonance Absorption Spectrum*. New. J. Phys. Vol.22, 073068 or
- [74] Parshin, D.A. Rzaev, É.A. (1987) *Spectral Diffusion and Phonon Bottleneck in Glasses*. Zh. Eksp. Teor. Fiz. Vol. 93, pp. 2129-2150
- [75] Levinson, I.B. (1983) *Establishment of Temperature in Dielectric Glasses below 1K*. Pis'ma Zh. Eksp. Teor. Fiz. Vol. 37, No. 3, pp. 157-159
- [76] Chudnovsky, E.M. et al. (2005) *Universal Mechanism of Spin Relaxation in Solids*. Phys. Rev. B Vol. 72, 094426
- [77] Chudnovsky, E.M. (2004) *Universal Decoherence in Solids*. Phys. Rev. Lett. Vol. 92, 120405
- [78] Chudnovsky, E.M. (1994) *Conservation of Angular Momentum in the Problem of Tunneling of the Magnetic Moment*. Phys. Rev. Lett. Vol. 72, 3433
- [79] Garanin, D.A. Chudnovsky E.M. (2015) *Angular Momentum in Spin-Phonon Processes*. Phys. Rev. B Vol. 92, 024421
- [80] Nakane, J.J. Kohno, H. (2018) *Angular Momentum of Phonons and its Applications to Single-Spin Relaxation*. Phys. Rev. B Vol. 97, 174403

- [81] Anderson, A.C. (1981) *The Kapitza Thermal Boundary Resistance between Two Solids*. Chapter 1 in *Nonequilibrium Superconductivity, Phonons, and Kapitza Boundaries*. NATO Advanced Study Institutes Series Vol. 65
- [82] Little, W.A. (1959) *The transport of Heat Between Dissimilar Solids at Low Temperatures*. Canadian Journal of Physics Vol. 37, No. 3, pp. 247-384
- [83] Wyatt, A.F. (1981) *Kapitza Conductance of Solid-Liquid He Interfaces*. Chapter 2 in *Nonequilibrium Superconductivity, Phonons, and Kapitza Boundaries*. NATO Advanced Study Institutes Series Vol. 65
- [84] Liberadzka, J. et al. (2019) *Heat Transfer at Dielectric-Metallic Interfaces in the Ultra-Low Temperature Range*. IOP Conf. Ser.: Mater. Sci. Eng. Vol. 502, 012133
- [85] Zubarev, D.N. (1971) *Neravnovesnaia Statisticheskaiia Termodinamika*. [Nonequilibrium Statistical Thermodynamics.] Nauka Press, Moscow
- [86] Zubarev, D.N. Kalashnikov, V.P. (1970) *Derivation of the Nonequilibrium Statistical Operator from the Extremum of the Information Entropy*. Physica Vol.46 pp. 550-554
- [87] Buishvili, L.L. et al. (1968) *Quantum-Statistical Theory of the Dynamical Polarization of Nuclei in the Case of Non-Uniform ESR Line Broadening*. Zh. Eksp. Teor. Fiz. Vol. 54, pp. 876-890
- [88] Buishvili, L.L. et al. (1974) *Strong EPR Saturation under Phonon-Bottleneck Conditions*. Zh. Eksp. Teor. Fiz. Vol. 67, pp. 665-67
- [89] Buishvili, L.L. et al. (1971) *Effect of Phonon Heating in Nuclear Spin-Lattice Relaxation*. Zh. Eksp. Teor. Fiz. Vol. 60, pp. 1433-1444
- [90] Buishvili, L.L. et al. (1972) *Strong Saturation of Inhomogeneously Broadened Lines*. Zh. Eksp. Teor. Fiz. Vol. 63, pp. 1764-1775
- [91] Böttger, H. (1970) *On the Phonon Avalanche Generated by Spin-Lattice Relaxation in a Bottlenecked Crystal*. phys. stat. sol. Vol. 40, pp. 309
- [92] Böttger, H. (1969) *Phonon Bottleneck Investigation Using a Quantum Statistical Method*. phys. stat. sol. Vol. 35, pp. 653
- [93] Kessenikh, A. (2021) *Spin Temperature and Dynamic Nuclear Polarization. From the History of Researches (1949-1983)*. Substantia Vol. 5, No. 2, pp. 19-34

-
- [94] Ali, Md. M. et al. (2020) *Quantum Thermodynamics of Single Particle Systems*. Nature Scientific Reports Vol. 10, 13500
- [95] Morozov, V.G. Ignatyuk, V. (2018) *Energy Conservation and the Correlation Quasi-Temperature in Open Quantum Dynamics*. Particles Vol. 1, pp. 285-295
- [96] Bogoliubov, N.N. (1946) *Problemy Dinamicheskoi Teorii v Statisticheskoi Fiziki*. [Problems of Dynamic Theory in statistical Physics.] GITTL, Kiev.
- [97] Golubjeva, O.N. et al. (2010) *Nikolai Nikolaevich Bogoliubov - Great Scientist and Humanist of the XX-th Century*. Ukr. J. Phys. 2010 Vol. 55, No. 1, pp. 143-150
- [98] Röpke, G. (2019) *The Source Term of the Non-Equilibrium Statistical Operator*. Particles Vol. 2 pp. 309-338
- [99] Kuzemsky, A.L. (2006) *Statistical Theory of Spin Relaxation and Diffusion in Solids*. Journal of Low Temperature Physics, Vol. 143, Nos. 5/6, pp. 213-256
- [100] Kuzemsky, A.L. (2007) *Theory of Transport Processes and the Method of the Nonequilibrium Statistical Operator*. International Journal of Modern Physics B Vol. 21, No. 17, pp. 2821-2949
- [101] Pokrovskii, L.A. (1968) *Generalized Kinetic Equations obtained by means of an Unbalanced Statistical Operator*. Dokl. Akad. Nauk SSSR Vol. 183, No. 4, pp. 806-809
- [102] Solov'ev, A.E. (1989) *Spectral Diffusion in Phonon Propagation*. Fizika Tverdogo Tela, Vol. 32, Iss. 8, pp. 2198-2204
- [103] Grinberg, E.S. (1978) *Saturation of a Nonuniformly Broadened Line Under Phonon Bottleneck Conditions*. Izvestiya Vysshikh Uchebnykh Zavedenii, Fizika, No. 8, pp. 70-75
- [104] Al'tshuler, S.A. et al. (1972) *Mandel'shtam-Brillouin Light Scattering Investigation of a Phonon System Under Paramagnetic Resonance Saturation Conditions*. Zh. Eksp. Teor. Fiz. Vol. 62, pp. 639-651 Journal of Physics Vol. 37, No. 3, pp. 247-384
- [105] Clauß, C. (2014) *On-Chip Broadband Magnetic Resonance Spectroscopy Down to Ultralow Temperatures*. Physikalisches Institut der Universität Stuttgart

-
- [106] Li, C. et al. (1992) *Spectroscopic Properties and Fluorescence Dynamics of Er^{3+} and Yb^{3+} in Y_2SiO_5* . IEEE Journal of Quantum Electronics, Vol. 28, No. 4, pp. 1209-1221
- [107] Sain, A. Melde, K.L. (2017) *Impact of Ground Via Placement in Grounded Coplanar Waveguide (GCPW) Interconnects* IEEE Transactions on Components, Packaging, and Manufacturing Technology Vol. 6, Iss. 1, pp. 136-144
- [108] Kuzemsky, A.L. (2005) *Generalized Kinetic and Evolution Equations in the Approach of the Nonequilibrium Statistical Operator*. International Journal of Modern Physics B Vol. 19, No 16, pp. 1029-1059